

Entry No. 56

**IMPACT OF CUMULUS CONVECTIVE AND PLANETARY BOUNDARY  
LAYER PARAMETERIZATION SCHEMES ON THE SIMULATION OF  
TROPICAL CYCLONE USING WEATHER RESEARCH AND  
FORECASTING (WRF) MODEL**

By

**MD. JAHANGIR HOSSAIN**

ROLL NO: 0755501

SESSION: JANUARY 2007

A THESIS SUBMITTED TO THE DEPARTMENT OF PHYSICS, KHULNA  
UNIVERSITY OF ENGINEERING & TECHNOLOGY KHULNA-9203 IN PARTIAL  
FULFILLMENT OF THE REQUIREMENT FOR THE DEGREE OF MASTER OF  
PHILOSOPHY



**DEPARTMENT OF PHYSICS  
KHULNA UNIVERSITY OF ENGINEERING & TECHNOLOGY  
KHULNA-9203, BANGLADESH  
DECEMBER, 2013**



**DEDICATED**

**TO**

**MY PARENTS, TEACHERS, WIFE AND MY LOVING SON**

## Declaration

This is to certify that the thesis work entitled "**Impact of Cumulus convective and Planetary Boundary Layer parameterization schemes on the simulation of Tropical Cyclone using Weather Research and Forecasting (WRF) model**" has been carried out in partial fulfillment of the requirement for M. Phil. degree in the department of Physics, Khulna University of Engineering & Technology, Khulna- 9203, Bangladesh by Md. Jahangir Hossain. The above research work or any part of this work has not been submitted anywhere for the award of any degree or diploma. No other persons' work has been used without due acknowledgement.

Supervisor

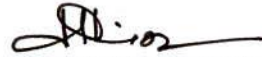


Name: **Dr. Md. Abdullah Elias Akhter**

Designation: Professor

Dept. of Physics, KUET

Candidate



Name: **Md. Jahangir Hossain**

Roll No: 0755501

## Acknowledgement

It is my honor and pleasure to admit that I have been facilitated for this thesis availing various types of altruistic help from many individuals in many ways.

I would like to express my heartfelt gratitude and inexhaustible recognition to Almighty Allah for His Devine blessings to finish this task.

With my great feelings of honor and respect I would like to express my jovial thanks and dedicated gratitude to my reverend, dynamic and pragmatic supervisor Professor Dr. Md. Abdullah Elias Akhter, Head, Department of Physics, Khulna University of Engineering & Technology, Khulna, Bangladesh, who has provided me his kind guidance, able and dynamic supervision and constant encouragement throughout this effort. His brainwave and friendly cooperation has accelerated my works.

It is a matter of contentment to record the affable sense of gratitude to Professor Dr. Shibendra Shekher Sikder, eminent researcher and scientist in the field of solid state physics, Department of Physics, Khulna University of Engineering & Technology, Khulna, Bangladesh, who has given me a well-built support in various ways.

I am also beholden to the members of faculty, Professor Dr. Mahbub Alam, Dr. Jolly Sultana, Mr. Md. Kamrul Hasan Reza, Mr. Md. Asaduzzaman, Department of Physics KUET, Bangladesh for their moral support.

I would like to carry my special gratitude and thankfulness to MCSK authority for providing me the facility to continue this work.

I am really thankful to all of my friends, particularly Assistant Professor Moumita Chaudhury, Jessore Science & Technology University, Md. Jahidul Islam and all other well-wishers and relatives who inspired me by their eternal blessings.

I would like to convey my cordial regards and thanks to all of my colleagues, particularly to Assistant Professor A.K.M Asaduzzaman, Assistant Professor K.M. Salim Reza, Assistant Prof. Md. Elius Hossain, and Mr. Abdul Awal of MCSK. I am also grateful to some of the others MCSK employees for their selfless help.

I am extremely grateful to the authority of Khulna University of Engineering & Technology, for providing me with all the necessary permissions and financial support to continue this thesis work.

I am really obliged to the Ministry of Science and Technology Peoples' Republic of Bangladesh for financing to research project.

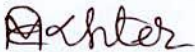
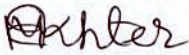
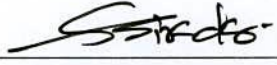


**KHULNA UNIVERSITY OF ENGINEERING & TECHNOLOGY  
DEPARTMENT OF PHYSICS**

Approval

This is to certify that the thesis work submitted by *Md. Jahangir Hossain* “*Impact of Cumulus Convective and Planetary Boundary Layer Parameterization Schemes on the Simulation of Tropical Cyclone using WRF Model*” has been accepted by the board of examiners for the partial fulfillment of the requirements for the degree of *Master of Philosophy* in the Department of *Physics*, Khulna University of Engineering & Technology, Khulna, Bangladesh in December 27, 2013.

**Board of Examiners**

**Sl. No. Name, Designation & Address**

1.   
\_\_\_\_\_  
Prof. Dr. Md. Abdullah Elias Akhter  
Department of Physics  
Khulna University of Engineering & Technology  
Chairman & Supervisor
2.   
\_\_\_\_\_  
Head  
Department of Physics  
Khulna University of Engineering & Technology  
Khulna 9203  
Member
3.   
\_\_\_\_\_  
Prof. Dr. Shibendra Shekher Sikder  
Department of Physics  
Khulna University of Engineering & Technology  
Khulna 9203  
Member
4.   
\_\_\_\_\_  
Prof. Dr. Jolly Sultana  
Department of Physics  
Khulna University of Engineering & Technology  
Khulna 9203  
Member
5.   
\_\_\_\_\_  
Dr. Samarendra Karmakar  
Director (Rtd), SAARC  
Meteorological Research Centre (SMRC)  
63 Jafrabad, 2<sup>nd</sup> floor, Dhaka – 1206, Bangladesh  
Member (External)

# TABLE OF CONTENT

	Page No.
<b>Acknowledgement</b>	<b>i</b>
<b>Table of content</b>	<b>ii</b>
<b>List of Tables</b>	<b>v</b>
<b>List of figures</b>	<b>vi</b>
<b>Abstract</b>	<b>xii</b>
<b>Abbreviation</b>	<b>xiii</b>
<b>1. Chapter I Introduction</b>	
1.1 Introduction	2
1.2 Objective & scope of the research	4
1.3 Social and economic benefit of the research	5
1.4 Layout of the research work	6
<b>2. Chapter II Literature review</b>	
2.1 Numerical weather prediction model	8
2.2 History of Numerical Weather Prediction Model	9
2.3 Description of WRF Model	11
2.3.1 Introduction	12
2.3.2 Major Features of the ARW System, Version 3	13
2.3.3 WRF Model Physics	14
2.3.4 Microphysics	15
2.3.4.1 Kessler scheme	16

2.3.4.2 Purdue Lin Scheme	16
2.3.4.3 WRF Single Moment 3 – class (WSM-3) Scheme	16
2.3.4.4 WRF Single Moment 5 – class (WSM-5) Scheme	17
2.3.4.5 WRF Single Moment 6 – class (WSM-6) Scheme	17
2.3.4.6 Eta Grid – Scale cloud and Precipitation (2001) Scheme.	18
2.3.4.7 Thompson et al. Scheme	18
2.3.4.8 Goddard Cumulus Ensemble Model Scheme	19
2.3.4.9 Morrison et al. Scheme 2-Moment Scheme	20
2.3.5 Cumulus Parameterization	20
2.3.5.1 Kain- Fritsch scheme	21
2.3.5.2 Betts – Miller – Janjic scheme	22
2.3.5.3 Grell – Devenyi Ensemble scheme	22
2.3.6 Surface Layer	23
2.3.7 Planetary boundary layer	23
2.3.8 Land Surface Model	24
2.4 Tropical cyclone	25
2.5 Tropical Cyclone Formation	27
2.6 The eye of the cyclone	28

### **3. Chapter III Methodology**

3. Model Selection	32
3.1 Act of Procedure	32
3.2 Experiments on simulation of Different TC events	34
3.3 Domain set up an Model Physics	34

3.4	Initial Data Source	35
3.5	Synoptic features of the selected tropical cyclones	36
3.5.1	Super cyclone Nargis (26 April- 02 May 2008)	36
3.5.2	Cyclonic storm Thane (25- 31 December, 2011)	36
3.5.3	Severe cyclonic storm Mahasen (10- 16 May 2013)	37

#### **4. Chapter IV Sensitivity Test**

4.1	Results, Discussion & Conclusion for sensitivity of PBL and CP on TC events	40
4.2	Simulation of Tropical Cyclone Nargis	47
4.2.1	Pressure field	47
4.2.2	Wind field	49
4.2.3	Vorticity field	56
4.2.4	Temperature anomaly	59
4.2.5	Water vapor mixing ratio	61
4.2.6	Rainfall pattern	62
4.2.7	Track pattern	63
4.3	Simulation of Tropical Cyclone Thane	64
4.3.1	Pressure field	64
4.3.2	Wind field	66
4.3.3	Vorticity field	73
4.3.4	Temperature anomaly	76
4.3.5	Water vapor mixing ratio	78
4.3.6	Rainfall pattern	79



4.3.7	Track pattern	80
4.4	Simulation of Tropical Cyclone Mahasen	81
4.4.1	Pressure field	81
4.4.2	Wind field	83
4.4.3	Vorticity field	90
4.4.4	Temperature anomaly	93
4.4.5	Water vapor mixing ratio	94
4.4.6	Rainfall pattern	96
4.4.7	Track pattern	97
<b>5.</b>	<b>Chapter V Conclusion</b>	<b>99</b>
	<b>References</b>	<b>101</b>

## LIST OF TABLES

TABLE NAME	Page No.	
2.1	Severity of TC	26
3.1	Design of the experiments.	33
3.2	Dimension of the domain for TC events.	34
3.3	Domain design for the WRF model version-3.	35
4.1	Best combinations Selection in TC Nargis simulation.	42
4.2	Best combinations Selection in TC Thane simulation.	44
4.3	Best combinations Selection in TC Mahasen simulation.	46

## LIST OF FIGURES

Figure Name	Page No.
2.1 TC breeding grounds are located over certain ocean basins.	27
2.2 Satellite picture of TC.	27
2.3 Eye of TC.	28
2.4 Image of TC eye.	28
4.1(a) Time variation of observed & model simulated SLP (hPa) for TC Nargis.	41
4.1 (b) Time variation of observed & model simulated wind (m/s) for zTC Nargis.	41
4.1(c) Model simulated tracks in 6-h interval for TC Nargis.	42
4.1(d) Time variation of observed & model simulated SLP (hPa) for TC Thane.	43
4.1(e) Time variation of observed & model simulated wind (m/s) for TC Thane.	43
4.1(f) Model simulated tracks in 6-h interval for TC Thane	44
4.1(g) Time variation of observed & model simulated wind (m/s) for TC Mahasen	45
4.1(h) Time variation of observed & model simulated SLP (hPa) for TC Mahasen.	45
4.1 (i) Model simulated tracks in 6-h interval for TC Mahasen.	46
4.2.(a) Time variation of observed & simulated SLP (hPa) for TC Nargis.	48
4.2.(b) Disribution of model simulated SLP (hPa) for TC Nargis at 00 UTC on 29,30 April & 01 May and 21 UTC on 01 May 2008.	48
4.3(a) Time variation of observed and model simulated wind (m/s) for TC Nargis.	51

4.3(b)	Surface wind (m/s) distribution for TC Nargis at 00 UTC on 29, 30 April & 01 May and 21 UTC on 01 May 2008.	51
4.3(c)	Model simulated east-west cross section of vertical profile of radial wind (m/s) at 00 UTC on 29, 30 April & 01 May and 21 UTC on 01 May 2008.	52
4.3(d)	Model simulated east-west cross section of vertical profile of tangential wind (m/s) at 00 UTC on 29, 30 April & 01 May and 21 UTC on 01 May 2008.	52
4.3(e)	Model simulated east-west cross section of vertical profile of vertical wind (m/s) at 00 UTC on 29, 30 April & 01 May and 21 UTC on 01 May 2008.	53
4.3(f)	Model simulated wind vector and magnitude at 00 UTC on 29, 30 April & 01 May and 21 UTC on 01 May 2008 at 850 hPa level.	53
4.3 (g)	Model simulated wind vector and magnitude at 00 UTC on 29, 30 April & 01 May and 21 UTC on 01 May 2008 at 500 hPa level.	54
4.3(h)	Model simulated wind vector and magnitude at 00 UTC on 29, 30 April & 01 May and 21 UTC on 01 May 2008 at 300 hPa level.	54
4.3(i)	Model simulated wind vector and magnitude at 00 UTC on 29, 30 April & 01 May and 21 UTC on 01 May 2008 at 100 hPa level.	55
4.3 (j)	Model simulated east-west cross section of vertical profile of horizontal wind for TC along the center at 00 UTC on 29, 30 April & 01 May and 21 UTC on 01 May 2008.	55
4.4(a)	Model simulated vorticity field at 00 UTC on 29, 30 April & 01 May and 21 UTC on 01 May 2008 at 850 hPa level.	57
4.4(b)	Model simulated vorticity field 00 UTC on 29, 30 April & 01 May and 21 UTC on 01 May 2008 at 500 hPa level.	57
4.4(c)	Model simulated vorticity field at 00 UTC on 29, 30 April & 01 May and 21 UTC on 01 May 2008 at 300 hPa level.	58

4.4(d)	Model simulated vorticity field at 00 UTC on 29, 30 April & 01 May and 21 UTC on 01 May 2008 at 100 hPa level.	58
4.5	Vertical distribution of temperature anomaly in the east-west direction through the centre 00 UTC on 29, 30 April & 01 May and 21 UTC on 01 May 2008.	60
4.6	Vertical distribution of water vapor mixing ratio in the east-west direction through the centre at 00 UTC on 29, 30 April & 01 May and 21 UTC on 01 May 2008.	61
4.7	24- hours accumulated rainfall (mm) of TC Nargis for the day 29 & 30 April and 01 May 2008.	62
4.8	Model simulated tracks in 6-h interval for different parameterization schemes for TC Nargis.	63
4.9(a)	Time variation of observed & simulated SLP (hPa) for TC Thane.	65
4.9(b)	Distribution of model simulated SLP (hPa) for TC Thane at 00 UTC on 28, 29 & 30 December and 18 UTC on 29 December 2011.	65
4.10 (a)	Time variation of observed & model simulated wind (m/s) for TC Thane.	68
4.10 (b)	Surface wind (m/s) distribution at 00 UTC on 28, 29 & 30 December and 18 UTC on 29 December 2011.	68
4.10 (c)	Model simulated wind vector and magnitude at 00 UTC on 28, 29 & 30 December and 18 UTC on 29 December 2011 at 850 hPa level.	69
4.10(d)	Model simulated wind vector and magnitude at 00 UTC on 28, 29 & 30 December and 18 UTC on 29 December 2011 at 500 hPa level.	69
4.10(e)	Model simulated wind vector and magnitude at 00 UTC on 28, 29 & 30 December and 18 UTC on 29 December 2011 at 300 hPa level.	70
4.10(f)	Model simulated wind vector and magnitude at 00 UTC on 28, 29 & 30 December 2011 and 18 UTC on 29 December 2011 at 100 hPa level.	70

4.10(g)	Model simulated east-west cross section of vertical profile of radial wind at 00 UTC on 28, 29 & 30 December and 18 UTC on 29 December 2011.	71
4.10(h)	Model simulated east-west cross section of vertical profile of tangential wind at 00 UTC on 28, 29 & 30 December and 18 UTC on 29 December 2011.	71
4.10(i)	Model simulated east-west cross section vertical profile of vertical wind at 00 UTC on 28, 29 & 30 December 2011 and 18 UTC on 29 December 2011.	72
4.10 (j)	Model simulated east-west cross section of vertical profile of horizontal wind at 00 UTC on 28, 29 & 30 December and 18 UTC on 29 December 2011.	72
4.11(a)	Model simulated vorticity field at 00 UTC on 28, 29 & 30 December and 18 UTC on 29 December 2011 at 850 hPa level.	74
4.11(b)	Model simulated vorticity field at 00 UTC on 28, 29 & 30 December and 18 UTC on 29 December 2011 at 500 hPa level.	74
4.11(c)	Model simulated vorticity field at 00 UTC on 28, 29 & 30 December and 18 UTC on 30 December 2011 at 300 hPa level.	75
4.11(d)	Model simulated vorticity field at 00 UTC on 28, 29 & 30 December and 18 UTC on 30 December 2011 at 100 hPa level.	75
4.12	Vertical distribution of temperature anomaly in the east-west direction through the centre at 00 UTC on 28, 29 & 30 December and 18 UTC on 30 December 2011.	77
4.13	Vertical distribution of water vapor mixing ratio in the east-west direction through the centre at 00 UTC on 28, 29 & 30 December and 18 UTC on 30 December 2011.	78
4.14	24- hours accumulated rainfall (mm) of TC Thane for the days 28, 29 and 30 December 2011.	79
4.15	Model simulated tracks in 6-h interval for TC Thane.	80



4.16(a)	Time variation of observed & simulated SLP (hPa) for TC Mahasen.	82
4.16(b)	Distribution of model simulated SLP (hPa) for TC Mahasen at 00 UTC on 14, 15 & 16 May and 15 UTC on 16 May 2013.	82
4.17 (a)	Time variation of observed & model simulated wind (m/s) for TC Mahasen.	85
4.17(b)	Surface wind (m/s) distribution at 00 UTC on 14, 15 & 16 May and 15 UTC on 16 May 2013.	85
4.17(c)	Model simulated wind vector and magnitude at 00 UTC on 14, 15 & 16 May and 15 UTC on 16 May 2013 at 850 hPa level.	86
4.17(d)	Model simulated wind vector and magnitude at 00 UTC on 14, 15 & 16 May and 15 UTC on 16 May 2013 at 500 hPa level.	86
4.17(e)	Model simulated wind vector and magnitude at 00 UTC on 14, 15 & 16 May and 15 UTC on 16 May 2013 at 300 hPa level.	87
4.17(f)	Model simulated wind vector and magnitude at 00 UTC on 14, 15 & 16 May and 15 UTC on 16 May 2013 at 100 hPa level.	87
4.17(g)	Model simulated east-west cross section of vertical profile of radial wind at 00 UTC on 14, 15 & 16 May and 15 UTC on 16 May 2013.	88
4.17(h)	Model simulated east-west cross section of vertical profile of tangential wind at 00 UTC on 14, 15 & 16 May and 15 UTC on 16 May 2013.	88
4.17(i)	Model simulated east-west cross section of vertical profile of vertical wind at 00 UTC on 14, 15 & 16 May and 15 UTC on 16 May 2013.	89
4.17 (j)	Model simulated east-west cross section of vertical profile of horizontal wind for TC Mahasen along the center at 00 UTC on 14, 15 & 16 May and 15 UTC on 16 May 2013.	89
4.18(a)	Model simulated vorticity field at 00 UTC on 14, 15 & 16 May and 15 UTC on 16 May 2013 at 850 hPa level.	91
4.18(b)	Model simulated vorticity field at 00 UTC on 14, 15 & 16 May and 15 UTC on 16 May 2013 at 500 hPa level.	91

4.18(c)	Model simulated vorticity field at 00 UTC on 14, 15 & 16 May and 15 UTC on 16 May 2013 at 300 hPa level.	92
4.18(d)	Model simulated vorticity field at 00 UTC on 14, 15 & 16 May and 15 UTC on 16 May 2013 at 100 hPa level.	92
4.19	Vertical distribution of temperature anomaly in the east-west direction through the centre at 00 UTC on 14, 15 & 16 May and 15 UTC on 16 May 2013.	94
4.20	Vertical distribution of water vapor mixing ratio in the east-west direction through the centre at 00 UTC on 14, 15 & 16 May and 15 UTC on 16 May 2013.	95
4.21	24- hours accumulated rainfall (mm) of TC Mahasen for 14, 15 and 16 May.	96
4.22	Model simulated tracks in 6-h interval for TC Mahasen.	97

## Abstract

The convection and planetary boundary layer (PBL) processes play significant role in the genesis and intensification of tropical cyclones (TCs). Three convective and two PBL parameterization schemes have been incorporated in the present study for numerical weather prediction models.

A systematic inter comparison of performance of parameterization schemes is essential to select a model for Bangladesh and its surroundings. In this context, a comprehensive sensitivity analysis on physical parameterization schemes of Weather Research and Forecasting (WRF) model have been carried out for the prediction of track and intensity of three the tropical cyclones: TC Nargis (26 April- 02 May, 2008), TC Thane (25-31 December, 2011) and Mahasen (10-16 May, 2013). For this purpose, making six possible combinations of physical parameterization schemes of two PBL Schemes (Yonsei University Scheme and Mellor Yamada Jainjic Scheme) and three convection schemes (Kain-Fritsch, Betts-Miller, and Grell-Devenyi) of WRF-ARW model are employed to obtain the best combination for the prediction of TCs over Bay of Bengal. In this regard, at first it is considered TC Nargis as the case- 1 (26 April- 02 May, 2008) and the WRF model is run using two types of Planetary Boundary Layer (PBL) YSU & MYJ respectively along with three Cumulus Parameterization (CP) KF, BM & GD schemes respectively and six independent run is made. The model domain is consisting of single nested with 9 km horizontal resolution with 28 vertical sigma levels. It is repeated the procedure for two other cases TC Thane (25-31 December, 2011) and TC Mahasen (10 - 16 May, 2013).

The simulated track and intensity (pressure & wind) are compared with the IMD observed data and select the best combination of the parameterization schemes. The tracks are also compared with those provided by the operational centers like NCEP and IMD. It is found that the combination of YSU PBL scheme with KF convection scheme (YKF) provides a better prediction of intensity, track, and rainfall consistently. The average Root Mean Square Error (RMSE) of intensity in terms SLP is 0.782243 hPa for all TCs, for 10-m wind is 2.2, 2.02, and 3.79  $\text{ms}^{-1}$  for Nargis, Thane and Mahasen respectively and mean track errors are 33.44 km for Mahasen, 21.16 km for Thane and 55.26 km for Nargis respectively. The errors are found to be least in all aspects with YKF combination.

Finally, the pressure, wind (vector and scalar horizontal wind, radial, tangential and vertical wind), vorticity, temperature anomaly, water vapor mixing ratio, rainfall and track have been studied to understand the cyclonic structure and dynamics.



## ABBREVIATIONS

ARW	:	The Advanced Research WRF
BMD	:	Bangladesh Meteorological Department
BM	:	Betts-Miller Janjic
CP	:	Cumulus Parameterization
GD	:	Grell Devenyi
FNL	:	Final Reanalysis
IMD	:	Indian Meteorological Department
KF	:	Kain-Fritsch
MP	:	Microphysics
MRF	:	Medium Range Forecast
MYJ	:	Mellor-Yamada-Janjic
NCEP	:	National Center for Environmental Prediction
NWP	:	Numerical Weather Prediction
PBL	:	Planetary Boundary Layer
RRTM	:	Rapid Radiative Transfer Model
WRF	:	Weather Research Forecasting
YSU	:	Yonsei University Scheme



# **CHAPTER 1**

## **INTRODUCTION**

## 1.1 Introduction

Bangladesh is of a precarious geographical position with the Himalayans in north and the Bay of Bengal in the south. The hilly areas are situated to the northeast and to the southeastern part of the country. The worlds' largest mangrove forest Sunder bans is located to the southwestern coastal zone of Bangladesh.

In the pre-monsoon season when the warm and moist air blows from the sea to the land in the lower level and the subtropical cool air blows from the westerly direction over this moisture laden hot air mass creating a situation of high instability in the troposphere favoring the convective processes to occur frequently. Due to this convection the other disasters come from the severe thunderstorms, squall lines, northwesterners, meso-scale convective clouds and tornadoes which are of localized nature and are relatively short lived but causes damages to lives and properties over the affected areas. The horizontal scale of these systems is within the range 1- 100 km. The Bay of Bengal is highly suitable for tropical cyclogenesis. One of the linked features of the tropical cyclone is the storm surge, which is responsible for major damages. The strong wind of the tropical cyclone exerts frictional forces on the water surface which is proportional to the square of the winds speed. This friction force causes high gravity waves with height up to 10-12 meters. This waves causes water to flow inland and lash everything in its path. The human casualties of these cyclones of 12 November 1970, 29 April 1991, 15 November 2007, were 300000, 138882, and 3363 respectively due to the rampage of this executioner cyclones.

Bangladesh has a placid winter and hot summer. The annual statistics show that 70.6 % of the country's average rainfall occurs during the southwest monsoon and 18.9 % during pre-monsoon seasons. The winter and pre monsoon show about 1.5 and 9 % of the annual average rainfall. There are considerable spatial variations. The northeast part of Bangladesh experiences very high rainfall. There are four prominent seasons in a year which are winter (December- February), pre-monsoon (March - May), monsoon (June- September) and post monsoon (October- November), the average annual rainfall varies from 1429 to 4338 mm. About 80 percent of the total rainfall of the country occurs in monsoon. The maximum rainfall is recorded in the coastal areas of Chittagong and northern part of Sylhet district while the minimum is observed in the

western and northwestern part of Bangladesh. Monsoon rainfall is very essential for agriculture. The agricultural and land use practices depend on the rainfall pattern and water availability.

The country is prone to disasters like floods and droughts, tropical cyclones and northwestern tornadoes. Variability of rainfall causes floods and droughts. The excess rainfall in Bangladesh and the upper catchments of the Bangladesh rivers causes floods. It is to mention that 92 % of the catchments of Ganges, Brahmaputra and Meghna lies outside Bangladesh and the runoff from these areas pass through Bangladesh which accounts for the 8 percent of the catchments. The severe floods cause the damages to crops, infrastructure, power supply, economic activities and overall livelihood of the affected areas. Beside these the heavy rainfall events cause flash floods and landslides.

Tropical cyclones (TC) are known over the whole globe for their devastation in the tropical regions particularly as they make landfall mainly due to high winds, torrential rains and the associated storm surge. It happen five tropical cyclones annually on an average over the Bay of Bengal, which represents 5.85% of the global frequency (Bhaskar Rao et al., 2001). To improve forecasts of these storm systems, it is important to get hold of a better understanding of their internal dynamics. Though there has been significant development in the field of TC track prediction over this region by various global and mesoscale models (RSMC Report 2010), there is still need for further improvement in its performance considering diversity and inconsistency in numerical weather prediction (NWP) guidance. There have been many attempts to improve up on the models through grid resolution, physical parameterizations and data assimilation etc. Among all, the physical parameterizations, which includes cumulus convection, surface fluxes of heat, moisture, momentum, and vertical mixing in the planetary boundary layer (PBL) play important role in the development and intensification of TCs (Anthes 1982). Among all, PBL and convection have long been recognized as processes of central importance in the genesis and intensification of TCs. In recent years, it has been realized that the PBL is a critical factor (Braun and Tao 2000) because of generation of the large fluxes of heat, moisture, and momentum in this thin layer: Therefore, several PBL parameterization schemes (PBLs) have been incorporated in the NWP

models (e.g., Mellor and Yamada 1982; Hong et al. 2006). In addition, turbulent eddies in the PBL transport moisture into the free convection regime and thus favor intensification of TCs. As the scale of convective clouds is too small to be resolved by numerical models, a wide variety of cumulus parameterization schemes (CPSs) have also been developed and incorporated into three dimensional mesoscale models (e.g., Kuo 1974; Arakawa and Schubert 1974; Anthes 1977; Betts and Miller 1986; Kain and Fritsch 1993; Grell 1993, etc.). Most of the above schemes evaluated for a specific convective environment (Grell 1993; Kuo et al. 1996). Hence, the general applicability of these schemes to any geographical environment is not obvious. Therefore, a systematic inter comparison of performance of these parameterization schemes is essential to customize a mesoscale model to examine (1) how well do these schemes perform in a mesoscale model under a variety of intense convective conditions and (2) consistency in the performance of these schemes in different geographical environments? Yang and Cheng (2005) studied the sensitivity of typhoon Toraji to different parameterization schemes of MMS model and reported that the Grell convection scheme and Goddard Microphysics explicit moisture schemes could provide the best track, whereas the warm rain scheme yielded the lowest central surface pressure. Rao and Bhaskar Rao (2003) showed that the intensity of the Orissa super cyclone is underestimated with Grell, MRF, and Simple-Ice schemes of MM5. Mandal et al. (2004) simulated two TCs over BoB using different physical parameterization schemes of MMS model and concluded that MRF PBL and Grell convection schemes could predict better track and intensity up to 48 h. Bhaskar Rao and Hari Prasad (2007) also studied the sensitivity of TC intensification to boundary layer and convective processes with MMS model but their study confined to only one case (Orissa super cyclone over BoB during 1999). Considering all the above, a study has been undertaken to examine the performance of various convection and PBL schemes for Bay of Bengal TCs using WRF model.

## **1.2 Objectives & Scope of the Research**

To improve forecasts of tropical cyclone systems, it is important to acquire a better understanding of their internal dynamics. So, a study has been undertaken to

examine the performance of various cumulus convection and PBL schemes for tropical cyclones over Bay of Bengal. Attempts will be taken to adjust the physical parameterization schemes and boundary layer parameterization to improve the performance of the models. A non-hydrostatic version of Advanced Research Weather Research and Forecasting (ARW-WRF, hereafter WRF) model is used for this purpose. The main objective of the study is to determine the most suitable model parameterization schemes for the simulation of the TC's over Bay of Bengal.

### **1.3 Social and Economic Benefit of the Research**

The economic activities of the country, especially the agriculture, are dependent on the rainfall. Besides, the tropical cyclones, tornadoes and the other meso-scale activities cause severe damage to lives, properties, infrastructure, agricultural crops and environment. The weather activities of Bangladesh are dominated by the southwest monsoon. Being the coastal zone Bangladesh has become the worst victim of the impacts of global warming associated climate change. The climate change has enhanced the natural disasters which have caused immeasurable casualties in loss of wealth, resources and livelihood. Tropical Cyclones can neither be destroyed nor be prevented, but its damages can be minimized by proper management practices which include preparedness, rescue operation and rehabilitation. Again agriculture plane can be made suitable using of the prediction of the above convective activity. To identify the impacts of precipitation it is to understand the knowledge of prediction at their earlier formation. So this requires research on the impact of cumulus convective and planetary boundary layer on the simulation of tropical cyclone using WRF model to save the valuable life and assets. It also helps the policy maker to develop the country especially in agriculture sector.

## **1.4 Layout of the research work**

The thesis has been organized with the following layout: Abstract, which summarizes the contents of the dissertation reflecting the theme of the work performed for this dissertation. Chapter- 1 contains introduction which delineates geographical settings of the Bay of Bengal and adjacent land masses, objectives and scope of the study and explains how the research results will bring social and economic benefits. Chapter- 2 contains an overview of tropical cyclones which describes the current state of knowledge about the cyclonic system based literature review and also contains a description of Advanced Research weather Research Forecasting Model (ARW) used in the present study. Chapter- 3 contains methodology, model set up and model initialization of the study. Chapter- 4 contains the results and discussion on the formation, evaluation and track movements of the selected tropical cyclones of the Bay of Bengal basing on the obtained results. In chapter- 5, the conclusion of the research findings have brought out with a few recommendation for future research on this subject.

## **CHAPTER 2**

### **LITERATURE REVIEW**



## 2.1 Numerical Weather Prediction Model

Models use systems of differential equations based on the laws of physics, fluid motion and chemistry and use a coordinates system which divides the planet into a 3D grid winds. Heat transfer, solar radiation, relative humidity and surface hydrology are calculated within each grid cell and the interaction with neighboring cells are used to calculate atmospheric properties in the future.

Numerical weather prediction uses mathematical models of the atmosphere and oceans to predict the weather based on current weather conditions. Though the first attempt was in 1920s, it was not until the advent of computer simulation in 1950s that numerical weather predictions produced realistic results. A number of global and regional forecast models are run in different countries worldwide, using current weather observations relayed from radio sounds or weather satellites as to input to the models.

Mathematical models based on the same physical principles can be used to generate either short term weather forecast or longer term climate predictions; the latter are widely used for understanding and projecting climate change. The improvements made to the regional models have allowed for significant improvements in tropical track and air quality forecast; however atmospheric models performs poorly at handing process that occur in a relatively constricted area, such as wild fires. Manipulating the vast datasets and performing the complex calculations it is necessary to modern numerical weather prediction requires some of the most powerful supercomputers in the world. Even with the increase of power of supercomputers, the forecast skill of numerical weather models extends up to about six days. Factors affecting the accuracy of numerical predictions include the density and quality of observations used as input to the forecasts, along with deficiencies in the numerical models themselves. Although the post-processing techniques such as model output statistics (MOS) have been developed to improve the handling of errors in numerical predictions, a more fundamental problem lies in the chaotic nature of the partial differential equations used to simulate the atmosphere. It is impossible to

solve these equations exactly, and small errors grow with time (doubling about every five days). In addition, the partial differential equations used in the model need to be supplemented with parameterizations for solar radiation, moist processes (clouds and precipitation), heat exchange, soil, vegetation, surface water, and the effects of terrain. In an effort to quantify the large amount of inherent uncertainty remaining in numerical predictions, ensemble forecasts have been used since the 1990s to help gauge the confidence in the forecast, and to obtain useful results farther into the future than otherwise possible. This approach analyzes multiple forecasts created with an individual forecast model or multiple models.

## **2.2 History of Numerical Weather Prediction Model**

The history of numerical weather prediction began in the 1920s through the efforts of Lewis Fry Richardson, who used procedures originally developed by Vilhelm Bjerknes to produce by hand a six-hour forecast for the state of the atmosphere over two points in central Europe, taking at least six weeks to do so. It was not until the advent of the computer and computer simulations that computation time was reduced to less than the forecast period itself. The ENIAC was used to create the first weather forecasts via computer in 1950; in 1954, Carl-Gustav Rossby's group at the Swedish Meteorological and Hydrological Institute used the same model to produce the first operational forecast (i.e. routine predictions for practical use). Operational numerical weather prediction in the United States began in 1955 under the Joint Numerical Weather Prediction Unit (JNWPU), a joint project by the U.S. Air Force, Navy and Weather Bureau.

In 1956, Norman Phillips developed a mathematical model which could realistically depict monthly and seasonal patterns in the troposphere; this became the first successful climate model. Following Phillips' work, several groups began working to create general circulation models. The first general circulation climate model that combined both oceanic and atmospheric processes was developed in the late 1960s at the NOAA Geophysical Fluid Dynamics Laboratory.

As computers have become more powerful, the size of the initial data sets has increased and newer atmospheric models have been developed to take advantage of the added available computing power. These newer models include more physical processes in the simplifications of the equations of motion in numerical simulations of the atmosphere. In 1966, West Germany and the United States began producing operational forecasts based on primitive-equation models, followed by the United Kingdom in 1972 and Australia in 1977.

The development of limited area (regional) models facilitated advances in forecasting the tracks of tropical cyclones as well as air quality in the 1970s and 1980s. By the early 1980s models began to include the interactions of soil and vegetation with the atmosphere, which led to more realistic forecasts.

The output of forecast models based on atmospheric dynamics is unable to resolve some details of the weather near the Earth's surface. As such, a statistical relationship between the output of a numerical weather model and the ensuing conditions at the ground was developed in the 1970s and 1980s, known as model output statistics (MOS). Starting in the 1990s, model ensemble forecasts have been used to help define the forecast uncertainty and to extend the window in which numerical weather forecasting is viable farther into the future than otherwise possible.

The atmosphere is a fluid. As such, the idea of numerical weather prediction is to sample the state of the fluid at a given time and use the equations of fluid dynamics and thermodynamics to estimate the state of the fluid at some time in the future. The process of entering observation data into the model to generate initial conditions is called *initialization*. On land, terrain maps available at resolutions down to 1Km (0.6 mi) globally are used to help model atmospheric circulations within regions of rugged topography, in order to better depict features such as down slope winds, mountain waves and related cloudiness that affects incoming solar radiation. The main inputs from country-based weather services are observations from devices (called radio sounds) in weather balloons that measure various atmospheric parameters and transmit them to a fixed receiver, as well as from weather satellites. The World Meteorological Organization acts to standardize the instrumentation, observing practices and timing of these observations worldwide. Stations either report hourly in Reports, or every six hours in SYNOP reports. These observations are

irregularly spaced, so they are processed by data assimilation and objective analysis methods, which perform quality control and obtain values at locations usable by the model's mathematical algorithms. Some global models use finite differences, in which the world is represented as discrete points on a regularly spaced grid of latitude and longitude; other models use spectral methods that solve for a range of wavelengths. The data are then used in the model as the starting point for a forecast.

A variety of methods are used to gather observational data for use in numerical models. Sites launch radio sounds in weather balloons which rise through the troposphere and well into the stratosphere. Information from weather satellites is used where traditional data sources are not available. Commerce provides pilot reports along aircraft routes and ship reports along shipping routes. Research projects use reconnaissance aircraft to fly in and around weather systems of interest, such as tropical cyclones. Reconnaissance aircraft are also flown over the open oceans during the cold season into systems which cause significant uncertainty in forecast guidance, or are expected to be of high impact from three to seven days into the future over the downstream continent. Sea ice began to be initialized in forecast models in 1971. Efforts to involve sea surface temperature in model initialization began in 1972 due to its role in modulating weather in higher latitudes of the Pacific.

## **2.3 Description of WRF model**

Weather Research and Forecasting (WRF) is a next generation mesoscale numerical weather forecasting community model. Its simulation capacity is very high and can simulate meteorological phenomena ranging from meters to thousands of kilometers. The ARW is the ARW dynamics solver together with other components of the WRF system compatible with that solver and used in producing a simulation. Thus, it is a subset of the WRF modeling system that, in addition to the ARW solver, encompasses physics schemes, numeric/dynamics options, initialization routines, and a data assimilation package (WRF-Var). The ARW solver shares the WRF with the NMM solver and all other WRF components within the framework.

### **2.3.1 Introduction**

The Weather Research and Forecasting (WRF) model is a numerical weather prediction (NWP) and atmospheric simulation system designed for both research and operational applications. WRF is supported as a common tool for the university/research and operational communities to promote closer ties between them and to address the needs of both. The development of WRF has been a multi-agency effort to build a next-generation mesoscale forecast model and data assimilation system to advance the understanding and prediction of mesoscale weather and accelerate the transfer of research advances into operations. The WRF effort has been a collaborative one among the National Center for Atmospheric Research's (NCAR) Mesoscale and Microscale Meteorology (MMM) Division, the National Oceanic and Atmospheric Administration's (NOAA) National Centers for Environmental Prediction (NCEP) and Earth System Research Laboratory (ESRL), the Department of Defense's Air Force Weather Agency (AFWA) and Naval Research Laboratory (NRL), the Center for Analysis and Prediction of Storms (CAPS) at the University of Oklahoma, and the Federal Aviation Administration (FAA), with the participation of university scientists. WRF reflects flexible, state-of-the-art, portable code that is efficient in computing environments ranging from massively-parallel supercomputers to laptops. Its modular, single-source code can be configured for both research and operational applications. Its spectrum of physics and dynamics options reflects the experience and input of the broad scientific community. Its WRF-Var variational data assimilation system can ingest a host of observation types in pursuit of optimal initial conditions, while its WRF-Chem model provides a capability for air chemistry modeling. WRF is maintained and supported as a community model to facilitate wide use internationally, for research, operations, and teaching. It is suitable for a broad span of applications across scales ranging from large-eddy to global simulations. Such applications include real-time NWP, data assimilation development and studies, parameterized-physics research, regional climate simulations, air quality modeling, atmosphere-ocean coupling, and idealized simulations. As of this writing, the number of registered WRF users exceeds 6000, and WRF is in operational and research use around the world. The WRF Software Framework (WSF) provides the infrastructure that accommodates the dynamics solvers, physics packages that interface with the solvers, programs for

initialization, WRF-Var, and WRF-Chem. There are two dynamics solvers in the WSF: the Advanced Research WRF (ARW) solver (originally referred to as the Eulerian mass or "em" solver) developed primarily at NCAR, and the Analyses.

### **2.3.2 Major Features of the ARW System, Version 3**

#### ARW Solver

- Equations: Fully compressible, Euler non-hydrostatic with a run-time hydrostatic option available. Conservative for scalar variables.
- Prognostic Variables: Velocity components  $u$  and  $v$  in Cartesian coordinate, vertical velocity  $w$ , perturbation potential temperature, perturbation geo-potential, and perturbation surface pressure of dry air. Optionally, turbulent kinetic energy and any number of scalars such as water vapor mixing ratio, rain/snow mixing ratio, cloud water/ice mixing ratio, and chemical species and tracers.
- Vertical Coordinate: Terrain-following, dry hydrostatic-pressure, with vertical grid stretching permitted. Top of the model is a constant pressure surface.
- Horizontal Grid: Arakawa C-grid staggering.
- Time Integration: Time-split integration using a 2nd- or 3rd-order Runge-Kutta scheme with smaller time step for acoustic and gravity-wave modes. Variable time step capability.
- Spatial Discretization: 2nd- to 6th-order advection options in horizontal and vertical.
- Turbulent Mixing and Model Filters: Sub-grid scale turbulence formulation in both coordinate and physical space. It is divergence damping, external-mode filtering, vertically implicit acoustic step off-centering and having explicit filter option.
- Initial Conditions: Three dimensional for real-data, and one-, two- and three-dimensional for idealized data. It possesses digital filtering initialization (DFI) capability available (real-data cases).
- Lateral Boundary Conditions: Periodic, open, symmetric, and specified options available.

- Top Boundary Conditions: Gravity wave absorbing (diffusion, Rayleigh damping, or implicit Rayleigh damping for vertical velocity). Constant pressure level at top boundary along a material surface. Rigid lid option.
- Bottom Boundary Conditions: Physical or free-slip.
- Earth's Rotation: Full Coriolis terms included.
- Mapping to Sphere: Four map projections are supported for real-data simulation: polar stereographic, Lambert conformal, Mercator, and latitude-longitude (allowing rotated pole). Curvature terms included.
- Nesting: One-way interactive, two-way interactive and moving nests. Multiple levels and integer ratios.
- Nudging: Grid (analysis) and observation nudging capabilities available.
- Global Grid: Global simulation capability using polar Fourier filter and periodic east-west conditions.

### **2.3.3 WRF Model Physics**

The WRF physics options fall into several categories, each contains several choices. The physics categories are (1) micro- physics, (2) cumulus parameterization, (3) planetary boundary layer (PBL), (4) land-surface model, and (5) radiation. Diffusion may also be considered part of the physics. The chapter will also address four-dimensional data assimilation (FDDA) methods that are available in ARW. These methods apply extra forcing to the model equations, and are internally treated similarly to physics. The physics section is insulated from the rest of the dynamics solver by the use of physics drivers. These are between solver-dependent routines: a pre-physics preparation and post-physics modifications of the tendencies. The physics preparation involves filling arrays with physics-required variables that include the temperature, pressure, heights, layer thicknesses, and other state variables in MKS units at half-level grid points and on full levels. The velocities are also de-staggered so that the physics part is independent of the dynamical solver's velocity staggering. Physics packages compute tendencies for the velocity components (un-staggered), potential temperature, and moisture fields. The solver-dependent post-physics step will re-stagger these

tendencies as necessary, couple tendencies with coordinate metrics, and convert to variables or units appropriate to the dynamics solver. The initialization of the physics is called prior to the first model step. This initialization may include reading in data files for physics tables or calculating look-up tables of functions. Each physics module includes an initialization routine for this purpose. Often physics packages will have many of their own constants that should also be included in their own module, while common physical constants are passed in from the physics drivers.

### **2.3.4 Microphysics**

Microphysics includes explicitly resolved water vapor, cloud, and precipitation processes. The model is general enough to accommodate any number of mass mixing-ratio variables, and other quantities such as number concentrations. Four-dimensional arrays with three spatial indices and one species index are used to carry such scalars. Memory, i.e., the size of the fourth dimension in these arrays, is allocated depending on the needs of the scheme chosen, and advection of the species also applies to all those required by the microphysics option. In the current version of the ARW, microphysics is carried out at the end of the time-step as an adjustment process, and so does not provide tendencies.

The rationale for this is that condensation adjustment should be at the end of the time-step to guarantee that the final saturation balance is accurate for the updated temperature and moisture. However, it is also important to have the latent heating forcing for potential temperature during the dynamical sub-steps, and this is done by saving the microphysical heating as an approximation for the next time-step as described in Section.

Currently, the sedimentation process is accounted for inside the individual microphysics modules, and, to prevent instability in the calculation of the vertical flux of precipitation, a smaller time step is allowed. The saturation adjustment is also included inside the microphysics. In the future, however, it might be separated into an individual subroutine to enable the remaining microphysics to be called less frequently than the model's advection step for efficiency shows a summary of the options indicating the number of moisture variables, and whether ice-phase and mixed-phase processes are included. Mixed-phase processes are those that result from the interaction of ice and water



particles, such as riming that produces graupel or hail. As a general rule, for grid sizes less than 10 km, where updrafts may be resolved, mixed-phase schemes should be used, particularly in convective or icing situations. For coarser grids the added expense of these schemes is not worth it because riming is not likely to be well resolved.

#### **2.3.4.1 Kessler Scheme**

This scheme (Kessler, 1969), which was taken from the COMMAS model (Wicker and Wilhelmson, 1995), is a simple warm cloud scheme that includes water vapor, cloud water, and rain. The microphysical processes included are: the production, fall, and evaporation of rain; the accretion and auto conversion of cloud water; and the production of cloud water from condensation.

#### **2.3.4.2 Purdue Lin Scheme**

Six classes of hydrometeors are included: water vapor, cloud water, rain, cloud ice, snow, and graupel. All parameterization production terms are based on Lin et al. (1983) and Rutledge and Hobbs (1984) with some modifications, including saturation adjustment following Tao et al. (1989) and ice sedimentation. This is a relatively sophisticated microphysics scheme in WRF, and it is most suitable for use in research studies. The scheme is taken from the Purdue cloud model, and the details can be found in Chen and Sun (2002).

#### **2.3.4.3 WRF Single-Moment 3-class (WSM3) Scheme**

The WRF single-moment microphysics scheme follows Hong et al. (2004) including ice sedimentation and other new ice-phase parameterizations. A major difference from other approaches is that a diagnostic relation is used for ice number concentration that is based on ice mass content rather than temperature. The computational procedures are described in Hong and Lim (2006). As with WSM5 and WSM6, the freezing/melting processes are computed during the full-term sub-steps to increase accuracy in the vertical heating profile of these processes.

The order of the processes is also optimized to decrease the sensitivity of the scheme to the time step of the model. The WSM3 scheme predicts three categories of hydrometeors: vapor, cloud water/ice, and rain/snow, which is a so-called simple-ice

scheme. It follows Dudhia (1989) in assuming cloud water and rain for temperatures above freezing, and cloud ice and snow for temperatures below freezing. This scheme is computationally efficient for the inclusion of ice processes, but lacks super cooled water and gradual melting rates.

#### **2.3.4.4 WRF Single-Moment 5-class (WSM5) Scheme**

This scheme is similar to the WSM3 simple ice scheme. However, vapor, rain, snow, cloud ice, and cloud water are held in five different arrays. Thus, it allows super cooled water to exist, and a gradual melting of snow falling below the melting layer. Details can be found in Hong et al. (2004), and Hong and Lim (2006). As with WSM6, the saturation adjustment follows Dudhia (1989) and Hong et al. (1998) in separately treating ice and water saturation processes, rather than a combined saturation such as the Purdue Lin (above) and Goddard (Tao et al., 1989) schemes. This scheme is efficient in intermediate grids between the mesoscale and cloud-resolving grids.

#### **2.3.4.5 WRF Single-Moment 6-class (WSM6) Scheme**

The six-class scheme extends the WSM5 scheme to include graupel and its associated processes. Some of the graupel-related terms follow Lin et al. (1983), but its ice-phase behavior is much different due to the changes of Hong et al. (2004). A new method for representing mixed-phase particle fall speeds for the snow and graupel particles by assigning a single fall speed to both that is weighted by the mixing ratios, and applying that fall speed to both sedimentation and accretion processes is introduced (Dudhia et al., 2008).

The behavior of the WSM3, WSM5, and WSM6 schemes differ little for coarser mesoscale grids, but they work much differently on cloud-resolving grids. Of the three WSM schemes, the WSM6 scheme is the most suitable for cloud-resolving grids, considering the efficiency and theoretical backgrounds (Hong and Lim, 2006).

#### **2.3.4.6 Eta Grid-scale Cloud and Precipitation (2001) scheme**

This is also known as EGCP01 or the Eta Ferrier scheme. The scheme predicts changes in water vapor and condensate in the forms of cloud water, rain, cloud ice, and precipitation ice (snow/graupel/sleet). The individual hydrometeor fields are combined into total condensate, and it is the water vapor and total condensate that are advected in the model. Local storage arrays retain first-guess information that extract contributions of cloud water, rain, cloud ice, and precipitation ice of variable density in the form of snow, graupel, or sleet. The density of precipitation ice is estimated from a local array that stores information on the total growth of ice by vapor deposition and accretion of liquid water. Sedimentation is treated by partitioning the time averaged flux of precipitation into a grid box between local storage in the box and fall out through the bottom of the box. This approach, together with modifications in the treatment of rapid microphysical processes, permits large time steps to be used with stable results. The mean size of precipitation ice is assumed to be a function of temperature following the observational results of Ryan (1996). Mixed-phase processes are now considered at temperatures warmer than  $-30^{\circ}\text{C}$  (previously  $-10^{\circ}\text{C}$ ), whereas ice saturation is assumed for cloudy conditions at colder temperatures. Further description of the scheme can be found in Sec. 3.1 of the November 2001 Technical Procedures Bulletin (TPB) at <http://www.emc.ncep.noaa.gov/mmb/mmbpll/eta12tpb/> and on the COMET page at <http://meted.ucar.edu/nwp/pcu2/etapcp1.htm>.

#### **2.3.4.7 Thompson et al. scheme**

A new bulk microphysical parameterization (BMP) has been developed for use with WRF or other mesoscale models. Compared to earlier single-moment BMPs, the new scheme incorporates a large number of improvements to both physical processes and computer coding plus employs many techniques found in far more sophisticated spectral/bin schemes using look-up tables. Unlike any other BMP, the assumed snow size distribution depends on both ice water content and temperature and is represented as a sum of exponential and gamma distributions.

Furthermore, snow assumes a non-spherical shape with a bulk density that varies inversely with diameter as found in observations and in contrast to nearly all other BMPs that assume spherical snow with constant density.

New features specific to this version of the bulk scheme compared to the Thompson et al. (2004) paper description include:

- generalized gamma distribution shape for each hydrometeor species,
- Non-spherical, variable density snow, and size distribution matching observations,
- Y-intercept of rain depends on rain mixing ratio and whether apparent source is melted ice,
- Y-intercept of graupel depends on graupel mixing ratio,
- a more accurate saturation adjustment scheme,68
- Variable gamma distribution shape parameter for cloud water droplets based on observations,
- Look-up table for freezing of water drops,
- Look-up table for transferring cloud ice into snow category,
- Improved vapor deposition/sublimation and evaporation,
- Variable collection efficiency for rain, snow, and graupel collecting cloud droplets,
- improved rain collecting snow and graupel.

#### **2.3.4.8 Goddard Cumulus Ensemble Model scheme**

The Goddard Cumulus Ensemble (GCE) models (Tao and Simpson, 1993) one-moment bulk microphysical schemes are mainly based on Lin et al. (1983) with additional processes from Rutledge and Hobbs (1984). However, the Goddard microphysics schemes have several modifications. First, there is an option to choose either graupel or hail as the third class of ice (Mc Cumber et al.(1991). Graupel has a relatively low density and a high intercept value (i.e., more numerous small particles). In contrast, hail has a relative high density and a low intercept value (i.e., more numerous large particles).

These differences can affect not only the description of the hydrometeor population and formation of the anvil-stratiform region but also the relative importance of the microphysical-dynamical-radiative processes. Second, new saturation techniques (Tao

et al., 1989, 2003) were added. These saturation techniques are basically designed to ensure that super saturation (sub-saturation) cannot exist at a grid point that is clear (cloudy). Third, all microphysical processes that do not involve melting, evaporation or sublimation (i.e., transfer rates from one type of hydrometeor to another) are calculated based on one thermodynamic state. This ensures that all of these processes are treated equally. Fourth, the sum of all sink processes associated with one species will not exceed its mass. This ensures that the water budget will be balanced in the microphysical calculations.

The Goddard microphysics has a third option, which is equivalent to a two-ice (2ICE) scheme having only cloud ice and snow. This option may be needed for coarse resolution simulations (i.e., > 5 km grid size). The two-class ice scheme could be applied for winter and frontal convection.

#### **2.3.4.9 Morrison et al. 2-Moment scheme**

The Morrison et al. (2008) scheme is based on the two-moment bulk microphysics scheme of Morrison et al. (2005) and Morrison and Pinto (2006). Six species of water are included: vapor, cloud droplets, cloud ice, rain, snow, and graupel/hail. The code has a user-specified switch to include either graupel or hail. Prognostic variables include number concentrations and mixing ratios of cloud ice, rain, snow, and graupel/hail, and mixing ratios of cloud droplets and water vapor (total of 10 variables).

The prediction of two-moments (i.e., both number concentration and mixing ratio) allows for a more robust treatment of the particle size distributions, which are a key for calculating the microphysical process rates and cloud/precipitation evolution. Several liquid, ice, and mixed-phase processes are included. Particle size distributions are treated using gamma functions, with the associated intercept and slope parameters derived from the predicted.

#### **2.3.5 Cumulus parameterization**

These schemes are responsible for the sub-grid-scale effects of convective and/or shallow clouds. The schemes are intended to represent vertical fluxes due to unresolved updrafts and downdrafts and compensating motion outside the clouds. They

operate only on individual columns where the scheme is triggered and provide vertical heating and moistening profiles. Some schemes additionally provide cloud and precipitation field tendencies in the column, and future schemes may provide momentum tendencies due to convective transport of momentum. The schemes all provide the convective component of surface rainfall. Cumulus parameterizations are theoretically only valid for coarser grid sizes, (e.g., greater than 10 km), where they are necessary to properly release latent heat on a realistic time scale in the convective columns. While the assumptions about the convective eddies being entirely sub-grid-scale break down for finer grid sizes, sometimes these schemes have been found to be helpful in triggering convection in 5–10 km grid applications. Generally, they should not be used when the model can resolve the convective eddies itself (e.g.,  $\leq 5$  km grid).

### **2.3.5.1 Kain-Fritsch scheme**

The modified version of the Kain-Fritsch scheme (Kain, 2004) is based on Kain and Fritsch (1990) and Kain and Fritsch (1993), but has been modified based on testing within the Eta model. As with the original KF scheme, it utilizes a simple cloud model with moist updrafts and downdrafts, including the effects of detrainment, entrainment, and relatively simple microphysics. It differs from the original KF scheme in the following ways:

- A minimum entrainment rate is imposed to suppress widespread convection in marginally unstable, relatively dry environments.
- Shallow (non-precipitating) convection is allowed for any updraft that does not reach minimum cloud depth for precipitating clouds; this minimum depth varies as a function of cloud-base temperature.
- The entrainment rate is allowed to vary as a function of low-level convergence.
- Downdraft changes:
  - Source layer is the entire 150 – 200 mb deep layer just above cloud base.
  - Mass flux is specified as a fraction of updraft mass flux at cloud base. Fraction is a function of source layer RH rather than wind shear or other parameters, i.e., old precipitation efficiency relationship not used.

– Detrainment is specified to occur in updraft source layer and below.

### **2.3.5.2 Betts-Miller-Janjic scheme**

The Betts-Miller-Janjic (BMJ) scheme (Janjic, 1994, 2000) was derived from the Betts-Miller (BM) convective adjustment scheme (Betts, 1986; Betts and Miller, 1986). However, the BMJ scheme differs from the Betts-Miller scheme in several important aspects. The deep convection profiles and the relaxation time are variable and depend on the cloud efficiency, a non-dimensional parameter that characterizes the convective regime (Janjic, 1994). The cloud efficiency depends on the entropy change, precipitation, and mean temperature of the cloud. The shallow convection moisture profile is derived from the requirement that the entropy change be small and nonnegative (Janjic, 1994). The BMJ scheme has been optimized over years of operational application at NCEP, so that, in addition to the described conceptual differences, many details and/or parameter values differ from those recommended in Betts (1986) and Betts and Miller (1986). Recently, attempts have been made to refine the scheme for higher horizontal resolutions, primarily through modifications of the triggering mechanism. In particular:

- A floor value for the entropy change in the cloud is set up below which the deep convection is not triggered;
- In searching for the cloud top, the ascending particle mixes with the environment; and
- The work of the buoyancy force on the ascending particle is required to exceed a prescribed positive threshold.

### **2.3.5.3 Grell-Devenyi Ensemble Scheme**

Grell and Devenyi (2002) introduced an ensemble cumulus scheme in which effectively multiple cumulus schemes and variants are run within each grid box and then the results are averaged to give the feedback to the model.

In principle, the averaging can be weighted to optimize the scheme, but the default is an equal weight. The schemes are all mass-flux type schemes, but with differing updraft

and downdraft entrainment and detrainment parameters, and precipitation efficiencies. These differences in static control are combined with differences in dynamic control, which is the method of determining cloud mass flux. The dynamic control closures are based on convective available potential energy (CAPE or cloud work function), low-level vertical velocity, or moisture convergence. Those based on CAPE either balance the rate of change of CAPE or relax the CAPE to a climatological value, or remove the CAPE in a convective time scale. The moisture convergence closure balances the cloud rainfall to the integrated vertical advection of moisture. Another control is the trigger, where the maximum cap strength that permits convection can be varied. These controls typically provide ensembles of 144 members.

### **2.3.6 Surface Layer**

The surface layer schemes calculate friction velocities and exchange coefficients that enable the calculation of surface heat and moisture fluxes by the land-surface models and surface stress in the planetary boundary layer scheme. Over water surfaces, the surface fluxes and surface diagnostic fields are computed in the surface layer scheme itself. The schemes provide no tendencies, only the stability-dependent information about the surface layer for the land-surface and PBL schemes.

Currently, each surface layer option is tied to particular boundary-layer options, but in the future more interchangeability and options may become available. Note that some boundary layer schemes (YSU and MRF) require the thickness of the surface layer in the model to be representative of the actual surface layer (e.g. 50-100 meters).

### **2.3.7 Planetary Boundary Layer**

The planetary boundary layer (PBL) is responsible for vertical sub-grid-scale fluxes due to eddy transports in the whole atmospheric column, not just the boundary layer. Thus, when a PBL scheme is activated, explicit vertical diffusion is de-activated with the assumption that the PBL scheme will handle this process. The most appropriate horizontal diffusion choices are those based on horizontal deformation or constant Kh values where horizontal and vertical mixing are treated independently. The surface fluxes are provided by the surface layer and land-surface schemes. The PBL schemes determine the flux profiles within the well-mixed boundary layer and the stable layer,



and thus provide atmospheric tendencies of temperature, moisture (including clouds), and horizontal momentum in the entire atmospheric column.

Most PBL schemes consider dry mixing, but can also include saturation effects in the vertical stability that determines the mixing. The schemes are one-dimensional, and assume that there is a clear scale separation between sub-grid eddies and resolved eddies. This assumption will become less clear at grid sizes below a few hundred meters, where boundary layer eddies may start to be resolved, and in these situations the scheme should be replaced by a fully three-dimensional local sub-grid turbulence scheme such as the TKE diffusion scheme summarizes the basic features of the PBL schemes in ARW.

### **2.3.8 Land-Surface Model**

The land-surface models (LSMs) use atmospheric information from the surface layer scheme, radiative forcing from the radiation scheme, and precipitation forcing from the microphysics and convective schemes, together with internal information on the land's state variables and land-surface properties, to provide heat and moisture fluxes over land points and sea-ice points.

These fluxes provide a lower boundary condition for the vertical transport done in the PBL schemes (or the vertical diffusion scheme in the case where a PBL scheme is not run, such as in large-eddy mode). [Note that large-eddy mode with interactive surface fluxes is not yet available in the ARW, but is planned for the near future.] The land-surface models have various degrees of sophistication in dealing with thermal and moisture fluxes in multiple layers of the soil and also may handle vegetation, root, and canopy effects and surface snow-cover prediction. The land surface model provides no tendencies, but does update the land's state variables which include the ground (skin) temperature, soil temperature profile, soil moisture profile, snow cover, and possibly canopy properties. There is no horizontal interaction between neighboring points in the LSM, so it can be regarded as a one-dimensional column model for each WRF land grid-point, and many LSMs can be run in a stand-alone mode.

## 2.4 Tropical cyclone

A tropical cyclone is a rotational low pressure system in tropics when the central pressure falls by 5 to 6 hPa from the surrounding and maximum sustained wind speed reaches 34 knots (about 62 kmph). It is a vast violent whirl of 150 to 800 km, spiraling around a centre and progressing along the surface of the sea at a rate of 300 to 500 km a day. The word cyclone has been derived from Greek word 'cyclos' which means 'coiling of a snake'. The word cyclone was coined by Harry Paddington who worked as a Rapporteur in Kolkata during British rule. The terms "hurricane" and "typhoon" are region specific names for a strong "tropical cyclone". Tropical cyclones are called "Hurricanes" over the Atlantic Ocean and "Typhoons" over the Pacific Ocean. As the earth's rotation sets up an apparent force (called the Coriolis force) that pulls the winds to the right in the Northern Hemisphere (and to the left in the Southern Hemisphere). So, when a low pressure starts to form over north of the equator, the surface winds will flow inward trying to fill in the low and will be deflected to the right and a counter-clockwise rotation will be initiated. The opposite (a deflection to the left and a clockwise rotation) will occur south of the equator. This Coriolis force is too tiny to effect rotation in, for example, water that is going down the drains of sinks and toilets. The rotation in those will be determined by the geometry of the container and the original motion of the water. Thus, one can find both clockwise and counter-clockwise flowing drains no matter what hemisphere one is located. Tropical Cyclone can be compared to a heat engine. The energy input is from warm water and humid air over tropical oceans. Release of heat is through condensation of water vapor to water droplets/rain. Only a small percentage (3%) of this released energy is converted into Kinetic energy to maintain cyclone circulation (wind field). A mature cyclone releases energy equivalent to that of 100 hydrogen bombs. India Meteorological Department (IMD) uses a 3 minutes averaging for the sustained wind. The maximum sustained wind mentioned in the bulletins used by IMD is the highest 3 minutes surface wind occurring within the circulation of the system.

**Table 2.1: Severity of TC**

System	Pressure deficient (hPa)	Associated wind speed Knots (Kmph)
Low pressure area	1.0	<17(<32)
Depression	1.0- 3.0	17-27 (32–50)
Deep Depression	3.0 - 4.5	28-33 (51–59)
Cyclonic Storm	4.5- 8.5	34-47 (60-90)
Severe Cyclonic Storm (SCS)	8.5-15.5	48-63 (90-119)
Very Severe Cyclonic Storm(VSCS)	15.5-65.6	64-119 (119-220)
Super Cyclonic Storm	>65.6	>119(>220)

These surface winds are observed (or, more often, estimated) at the standard meteorological height of 10 m (33 ft) in an unobstructed exposure (i.e., not blocked by buildings or trees). The National Hurricane Centre uses a 1 minute averaging time for reporting the sustained wind. Some countries also use 10 minutes averaging time for this purpose. While one can utilize a simple ratio to convert from peak 10 minute wind to peak 1 minute wind or 3 minute wind, such systematic differences to make inter-basin comparison of tropical cyclones around the world is problematic. However there is no significant difference between the maximum sustained wind reported in different basis with different averaging method. The low pressure system over Indian region is classified based on the maximum sustained winds speed associated with the system and the pressure deficit/ number of closed isobars associated with the system. The pressure criteria are used, when the system is over land and wind criteria is used, when the system is over the sea. The system is called as low if there is one closed isobar in the interval of 2 hPa. It is called depression, if there are two closed isobars, a deep depression, if there are three closed isobars and cyclonic storm if there are four or more closed isobars. Considering wind criteria, the system with wind speed of 17-27 knots is called as depression and the low pressure system with maximum sustained 3 minutes

surface winds between 28-33 knots is called a deep depression. The system with maximum sustained 3 minutes surface winds of 34 knots or more is called as cyclonic storm. When the maximum sustained 3 minutes surface winds are more than 119 knots, the low pressure system is called as "Super Cyclone" over north Indian Ocean. Similarly, "Super-typhoon" is a term utilized by the U.S. Joint Typhoon Warning Centre for typhoons that reach maximum sustained 1 minute surface winds of at least 130 knots (65 m/s). This is the equivalent of a strong Saffir-Simpson category 4 or category 5 hurricane in the Atlantic basin or a category 5 severe tropical cyclone in the Australian basin. The detailed classification based on wind criteria are given in the Table 2.1.

## 2.5 Tropical Cyclone Formation

The tropical cyclones form over ocean basins in lower latitudes of all oceans except south Atlantic and southeast Pacific. The tropical cyclones develop over the warm water of the Bay of Bengal and the Arabian Sea. The favorable ocean basins for development of cyclonic storms are shown in the Figure 2.1.

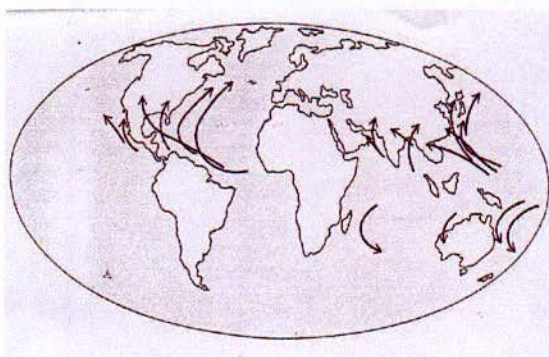


Figure: 2.1

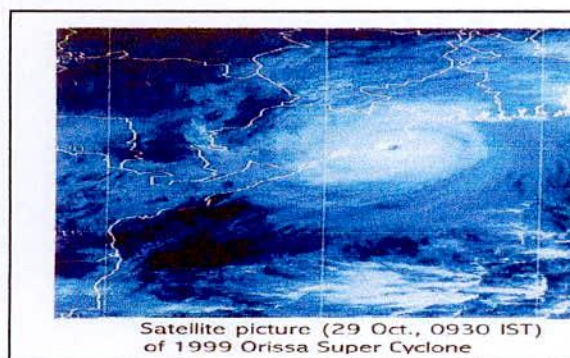


Figure: 2.2

Figure: TC breeding grounds are located over certain ocean basins. Arrows indicate average trajectories over different basins in Figure 2.1. Satellite picture of TC in the Figure 2.2.

A fully developed tropical cyclone has a central cloud free region of calm winds, known as the "eye" of the cyclone with diameter varying from 10 to 50 km. surrounding the eye

is the "wall cloud region" characterized by very strong winds and torrential rains, which has the width of about 10 to 150 km. The winds over this region rotate around the centre and resemble the "coils of a snake". Wind speed fall off gradually away from this core region, which terminate over areas of weaker winds with overcast skies and occasional squall .There may be one or more spiral branch in a cyclone where higher rainfall occurs. The vertical extent of the cyclone is about 15 km. The INSAT imagery of Orissa Super cyclone on 29<sup>th</sup> October, 1999 is shown in the Figure 2.2.

"CDO" is an acronym that stands for "central dense overcast". This is the cirrus cloud shield that results from the thunderstorms in the eye wall of a tropical cyclone and its rain bands. Before the tropical cyclone reaches very severe cyclonic storm (64 knots), typically the CDO is uniformly showing the cold cloud tops of the cirrus with no eye apparent. Once the storm reaches the hurricane strength threshold, usually an eye can be seen in either the infrared or visible channels of the satellites. Tropical cyclones that have nearly circular CDO's are indicative of favorable, low vertical shear environments.

## 2.6 Eye of the cyclone



Figure 2.3: Eye of TC

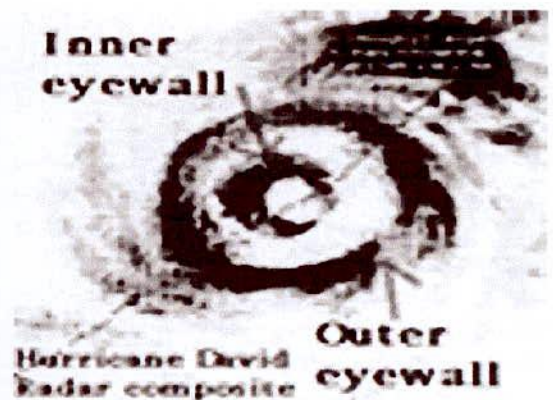


Figure 2.4: Image of TC eye.

The **"eye"** is a roughly circular area of comparatively light winds and fair weather found at the center of a severe tropical cyclone is shown in the Figure 2.3. Although the winds are calm at the axis of rotation, strong winds may extend well into the eye. There is little or no precipitation and sometimes blue sky or stars can be seen. The eye is the region of lowest surface pressure and warmest temperatures aloft - the eye temperature may be 10°C warmer or more at an altitude of 12 km than the surrounding environment, but only 0-2°C warmer at the surface in the tropical cyclone. Eyes range in size from 8 km to over 200 km across, but most are approximately 30-60 km in diameter. The eye is surrounded by the **"eye wall"**, the roughly circular ring of deep convection, which is the area of highest surface winds in the tropical cyclone. The eye is composed of air that is slowly sinking and the eye wall has a net upward flow as a result of many moderate - occasionally strong - updrafts and downdrafts. The eye's warm temperatures are due to compression warming of the subsiding air. Most soundings taken within the eye show a low-level layer, which is relatively moist, with an inversion above - suggesting that the sinking in the eye typically does not reach the ocean surface, but instead only gets to around 1-3 km of the surface. The exact mechanism by which the eye forms remains somewhat controversial. One idea suggests that the eye forms as a result of the downward directed pressure gradient associated with the weakening and radial spreading of the tangential wind field with height (Smith, 1980). Another hypothesis suggests that the eye is formed when latent heat release in the eye wall occurs, forcing subsidence in the storm's centre (Shapiro and Willoughby, 1982). It is possible that these hypotheses are not inconsistent with one another. In either case, as the air subsides, it is compressed and warms relative to air at the same level outside the eye and thereby becomes locally buoyant. This upward buoyancy approximately balances the downward directed pressure gradient so that the actual subsidence is produced by a small residual force. Another feature of tropical cyclones that probably plays a role in forming and maintaining the eye is the eye wall convection. Convection in tropical cyclones is organized into long, narrow rain bands which are oriented in the same direction as the horizontal wind. Because these bands seem to spiral into the centre of a tropical cyclone, they are called **"spiral bands"**. Along these bands, low-level convergence is a maximum, and therefore, upper-level divergence is most pronounced above. A direct circulation develops in which warm, moist air converges at the surface, ascends through these bands, diverges aloft, and descends on both sides of the bands.

Subsidence is distributed over a wide area on the outside of the rain band but is concentrated in the small inside area. As the air subsides, adiabatic warming takes place, and the air dries. Because subsidence is concentrated on the inside of the band, the adiabatic warming is stronger inward from the band causing a sharp contrast in pressure falls across the band since warm air is lighter than cold air. Because of the pressure falls on the inside, the tangential winds around the tropical cyclone increase due to increased pressure gradient. Eventually, the band moves toward the centre and encircles it and the eye and eye wall form. Thus, the cloud-free eye may be due to a combination of dynamically forced centrifuging of mass out of the eye into the eye wall and to a forced descent caused by the moist convection of the eye wall. This topic is certainly one that can use more research to ascertain which mechanism is primary.

Some of the most intense tropical cyclones exhibit concentric eye walls, two or more eye wall structures centered at the circulation centre of the storm. Just as the inner eye wall forms, convection surrounding the eye wall can become organized into distinct rings. Eventually, the inner eye begins to feel the effects of the subsidence resulting from the outer eye wall, and the inner eye wall weakens, to be replaced by the outer eye wall which is shown in the Figure 2.4. The pressure rises due to the destruction of the inner eye wall are usually more rapid than the pressure falls due to the intensification of the outer eye wall, and the cyclone itself weakens for a short period of time.

## **CHAPTER 3**

### **METHODOLOGY**





### 3. Model Selection

Advanced Weather Research Forecasting (WRF-ARW) single state of the art of mesoscale model has been taken to evaluate the performance for the simulation of tropical cyclone events.

#### 3.1 Act of Procedure

For achieving the objective of the study, the three convection and two Planetary Boundary Layer (PBL) schemes of Weather Research Forecasting (WRF) model are combined for simulation of TCs over Bay of Bengal (BoB) in near real time using the resultant combination of parameterization schemes. The Kain–Fritsch, Betts–Miller–Janjic, and Grell–Devenyi schemes are thereby referred as KF, BM, and GD schemes, respectively. The Yonsei University Scheme (YSU) and Mellor -Yamada -Janjic (MYJ) scheme are henceforth referred as Y and M, respectively.

For the study six experiments are carried out with six possible combinations of three Cumulus Parameterizations Schemes (CPS) and two Planetary Boundary Layer Schemes (PBLs) taking the WRF Single Moment -3 Class (WSM 3-class) micro physics scheme (Hong et al. 2004) as common. All the six experiments with the combination of these schemes and name of the experiments are given in Table 3.1.

Three test cases have been considered for the tropical cyclone events those are Case 1 Nargis ( 26 April- 02 May, 2008), Case 2 Thane (25-31 December, 2011) and Case 3 Cyclonic Storm, Mahasen over Bay of Bengal (10 - 16 May, 2013). All the cyclones are integrated up to 96 hours from their respective real initial time. The initial and boundary conditions are obtained from National Centers for Environment Prediction (NCEP) Final (FNL) analyses (9 km grid resolutions). For evaluation the experiments of the three considered cases: Nargis (26 April- 02 May, 2008), Thane (25-31-December, 2011) and Mahasen (10 - 16 May, 2013), have been analyzed and thereby compared the output of all the parameters with the respective observed values for finding the best combination.

**Table 3.1: Design of the experiments.**

S. No	Physical Parameterization schemes		Name of Experiments
1	PBLs	CPs	YKF
	Yonsei University Schemes (YSU)	Kain Fristch (KF) Scheme	
2	Yonsei University Schemes (YSU)	Betts Miller Janjic (BM) Scheme	YBM
3	Yonsei University Schemes (YSU)	Grell Devenyi (GD) Scheme	YGD
4	Meller Yamada Janjic Scheme (MYJ)	Kain Fristch (KF) Scheme	MKF
5	Meller Yamada Janjic Scheme (MYJ)	Betts Miller Janjic (BM) Scheme	MBM
6	Meller Yamada Janjic Scheme (MYJ)	Grell Devenyi (GD) Scheme	MGD

Three test cases, case 1 Nargis (26 April- 02 May, 2008), Case 2 Thane (25-31 December, 2011) and Case 3 Mahasen (10 - 16 May, 2013) are simulated with the optimum combination of physical parameterization schemes and expected result is achieved from the study. Table 3.1 describes the details of the total experiments in evaluation study. The NCEP Global Forecasting System (GFS) analyses and forecast products available in near real time are used as initial and boundary conditions to the model. The single domain is fixed between 78° E–99° E and 3° N–26° N for BoB TCs with 9-km horizontal grid resolution. The grid staggering is Arakawa C-grid. The complete model configuration with all the specifications is given in Table 3.3. Except different combinations of PBLs and CPs for customization study and the initial conditions for model evaluation study, the model configuration is kept identical in all

aspects for all the experiments. All the model-simulated results are compared with those prepared by IMD.

### 3.2 Experiments on simulation of different TC events

Tropical cyclone events have been considered for the simulation of different meteorological parameters to understand the genesis, characteristics and structure of the systems. Three test cases have been considered for the tropical cyclone events those are Case 1 Nargis ( 26 April- 02 May, 2008), Case 2 Thane (25-31 December, 2011) and Case 3 Cyclonic Storm, Mahasen (10 - 16 May, 2013).

### 3.3 Domain setup and Model Physics

It is taken single domain for tropical cyclone simulation. The horizontal grid resolution of the domain is 9 km. The dimension of the WRF model is summarized in the Table 3.2.

**Table 3.2: Dimension of the domain for TC**

Latitude °N	Longitude °E
3° N- 26°N	78° E- 99°E

The WRF model is run for TC cases using two types of Planetary Boundary Layer schemes, Yonsei University (YSU) and Mellor- Yamada- Janjic (MYJ), along with three cumulus parameterization schemes Kain-Fritsch (KF), Betts-Miller-Janjic (BMJ) and Grell-Devenyi (GD) making 06 independent run.

The common physics options which are used, other than the CPs and PBLs, includes: i) WSM 3-class microphysical scheme for moisture anticipation, ii) RRTM for long wave and Dudhia for short wave radiation schemes for radiation calculation and iii) 5- Loah land surface model to predict soil temperature which has been illustrated detail in the Table 3.3.

**Table 3.3: Domain design for the WRF model version 3**

Dynamics	Non-hydrostatic with three dimensional Coriolis force
Main prognostic variables	u, v, w, T, p and q
Map projection	Lambert conformal mapping
Central point of the domain	15.5 <sup>0</sup> N & 88.5 <sup>0</sup> E
Horizontal grid distance	9 km
Number of vertical levels	19
Horizontal grid system	Arakawa C grid
Time integration scheme	Leapfrog scheme with time splitting technique
PBL parameterization scheme	YSU, MYJ
Cumulus parameterization scheme	Kain-Fritsch (KF), Betts-Miller-Janjic(BMJ) and Grell-Devenyi (GD)
Microphysics	WSM 3 –class
Soil model	5- Loah land surface model

### **3.4 Initial Data Sources**

To simulate tropical cyclone (TC) events the WRF model is run for 96 hours. Final reanalysis (FNL) data (1<sup>0</sup> X 1<sup>0</sup>) from India Meteorological Department (IMD) is used as initial and lateral boundary conditions (LBCs) which is updated at six hour interval i.e, the model is initialized with 00, 06, 12 and 18 UTC initial field of corresponding date.

### **3.5 Synoptic features of the selected tropical cyclones (TC)**

These observed characteristics of the Tropical Cyclones Nargis, Thane and Mahasen are illustrated in the following subsections (3.5.1, 3.5.2 and 3.5.3) respectively.

#### **3.5.1 Very severe cyclone Nargis (26 April- 02 May, 2008)**

The very severe cyclone Nargis initially appeared as a low pressure area over Bay of Bengal on 26 April and concentrated into a depression at 03000 UTC on 27 April. The observed track of the VSCS 'Nargis' shows that the TC moved slightly northwestwards and intensified into a depression and then into a cyclone at 00 UTC on 28 April over the southwest and adjoining southeast and west central Bay of Bengal about 550 km east of Chennai. The system remained practically stationary for some time and further intensified into an SCS at 09 UTC on 28 April and into a VSCS at 0300 UTC on 29 April over west central and adjoining southwest and southeast Bay of Bengal. The system moved slightly to the north and then to the eastwards for a period about 30h from 0600 UTC of 01 May till 1500 UTC of 01 May towards the Myanmar coast and crossed Myanmar coast between 1730 and 1930h IST on 02 May 2008 as a VSCS. The intense cloud band associated with the system on 02 May at 06 UTC. Even after the landfall the system was maintaining its intensity as a VSCS for a period of about 12 h. The VSCS 'Nargis devastated large part of the low lying delta region of the Irrawaddy River. Winds exceeded 190 km ph as the storm ripped through the Myanmar's biggest city Yangon (estimated population 06 million) for over more than ten hours.

#### **3.5.2 Cyclonic Storm Thane (25-31 December, 2011)**

A depression formed over southeast Bay of Bengal in the evening of 25<sup>th</sup> December, 2011 and lay centered about 1000 km southeast of Chennai. It gradually moved north-northwestwards and intensified into a deep depression in the early morning of 26th December, 2011 and into a cyclonic storm 'THANE' in the same midnight. It then

moved west-northwestwards and intensified into a severe cyclonic storm in the afternoon and into a very severe cyclonic storm in the evening of 28<sup>th</sup> December, 2011. It then moved west-southwestwards and crossed north Tamil Nadu & Puducherry coast between Cuddalore and Puducherry within 0630 and 0730 hrs IST of 30<sup>th</sup> December, 2011 with a wind speed of 120-140 kmph. After landfall, the system rapidly weakened into a severe cyclonic storm over north coastal Tamil Nadu at 0830 hrs IST of 30<sup>th</sup> and into a deep depression around noon and into a depression in the same evening over the north Interior Tamil Nadu. It weakened further and lay as a well-marked low pressure area over north Kerala and neighborhood in early morning of 31<sup>st</sup> December, 2011.

### **3.5.3 Cyclonic Storm Mahasen over Bay of Bengal (10 - 16 May, 2013)**

A depression formed over southeast Bay of Bengal at 1430 hrs IST of 10<sup>th</sup> May 2013 near latitude  $5.0^{\circ}\text{N}$  and longitude  $92.0^{\circ}\text{E}$ . It moved northwestwards and intensified into a deep depression in the evening of the same day. Continuing its northwestward movement, it further intensified into a cyclonic storm, Mahasen in the morning of 11<sup>th</sup> May 2013. Under the influence of the anti-cyclonic circulation lying to the east, the cyclonic storm changed its direction of movement initially from northwesterly to northerly and then to north-northeasterly on 13<sup>th</sup> and 14<sup>th</sup> May respectively. On 15<sup>th</sup> May, it further came under the influence of the mid-latitude westerly trough running roughly along  $77^{\circ}\text{E}$ , which further helped in enhancing the north-northeastward movement of the cyclonic storm. As this trough came closer on 16<sup>th</sup> the north-northeastward speed of the cyclonic storm significantly increased, becoming about 40-50 kmph. The cyclonic storm crossed Bangladesh coast near lat.  $22.8^{\circ}\text{N}$  and long-  $91.4^{\circ}\text{E}$ , about 30 km south of Feni around 1330 hrs IST of 16<sup>th</sup> May 2013 with a sustained maximum surface wind speed of about 85- 95 kmph. After the landfall, it continued to move north-northeastwards and weakened gradually due to interaction with land surface. It weakened into a deep depression over Mizoram in the evening and into a depression over Manipur around mid-night of 16<sup>th</sup>. It further weakened into a well-marked low pressure area over Nagaland in the early morning and moved away

towards Myanmar as a low pressure area in the morning of 17th. The salient features of this storm are as follows;

- (i) The genesis of the disturbance took place in lower latitude, near 5 degree north.
- (ii) It was one of the longest track over north Indian Ocean in recent period after the very severe cyclonic storm, Phet over the Arabian Sea (31 May-07 June, 2010)
- (iii) The cyclonic storm moved very fast (about 40-50 km per hour on the day of landfall, i.e. on 16th May 2013. Such type of fast movement of the cyclonic storm is very rare.
- (iv) Due to the faster movement and the adverse weather the severity of the cyclonic storm was relatively less.

## ***CHAPTER 4***

### ***SENSITIVITY TEST***



## **4.1. Results, discussion and conclusion for the sensitivity of PBL and CP on TC events.**

Among the three tropical cyclones, at first TC Nargis has been taken and the WRF model is run using two types of Planetary Boundary Layer (PBL) along with three Cumulus Parameterization schemes (CP) and made 06 independent run. The simulated track and intensity (pressure & wind) are compared with the IMD observed data and select the best combination of the parameterization schemes. It has been repeated the procedure for two other cases (TC Thane and Mahasen). The simulated SLP, wind and track of the tropical cyclones Nargis, Thane and Mahasen are plotted along with IMD observed data and are shown in Figures 4.1(a), (b) & (c), 4.1(d), (e) & (f) and 4.1(g), (h) & (i) respectively. Performances of the selected PBLs with the CPs are not same for all combinations which have been shown in Tables: 4.1, 4.2 & 4.3. In the Figures 4.1 (b), (e) and (g), it is visualized that with time variation of observed and model simulated Maximum Wind Speed (MWS) at the standard meteorological height of 10-m varies significantly for all the TCs Nargis, Thane and Mahasen respectively. It is observed that the output from no combination is coordinated exactly with the observed MWSs. Simulated tracks for all the TCs Nargis, Thane and Mahasen, shown in the Figures 4.1 (c), (f) and (i) respectively, are deviated mainly in the left or right to the respective observed track. Simulated SLPs, shown in the Figures 4.1 (a), (d) and (h), are more or less than the observed. Considering the performance of PBL with CP for three TCs, it is seen from the Figures and Tables, no combination of PBL and CP perform absolutely better than others. But it seems that YSU PBL with KF CP performs better than any other combinations. This combination of PBL and CP may be used as an operational purpose for the TC prediction. But it is recommended that more combination may be done to search better option. Using the output of simulation for the best combination, pressure, wind (vector and scalar horizontal wind, radial, tangential and vertical wind), vorticity, temperature anomaly, water vapor mixing ratio and rainfall of the three tropical cyclones Nargis, Thane and Mahasen are studied.

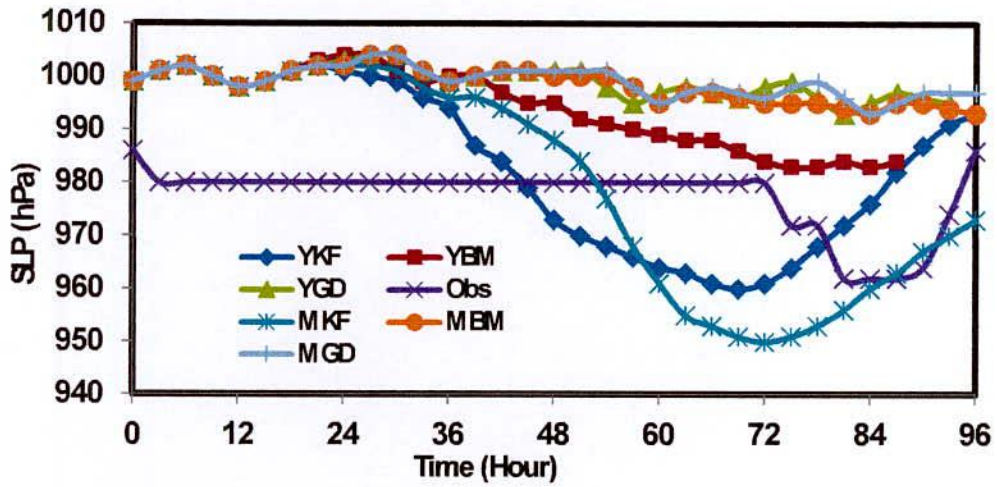


Figure 4.1(a): Time variation of observed & model simulated SLP (hPa) for TC Nargis.

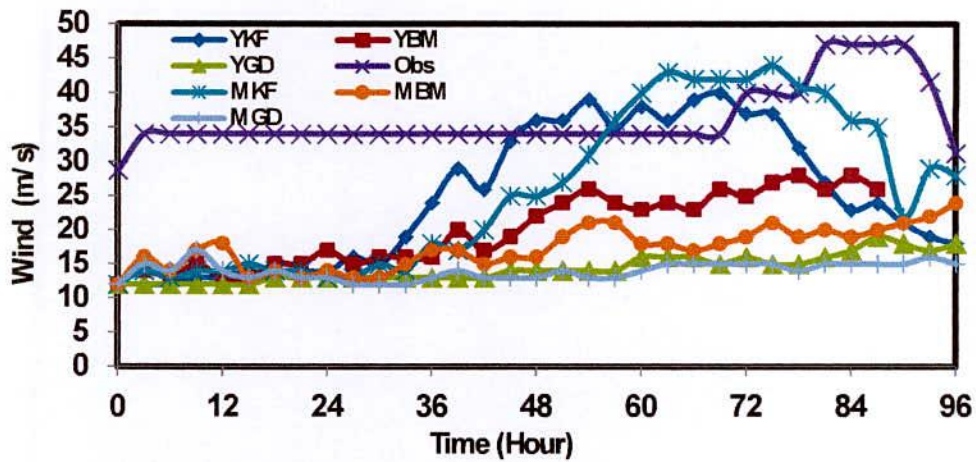


Figure 4.1 (b): Time variation of observed & model simulated wind speed (m/s) for TC Nargis.

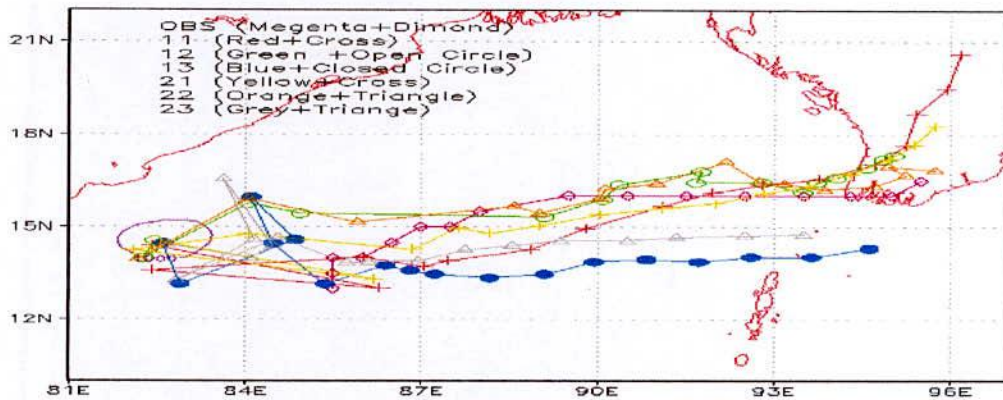


Figure 4.1(c): Model simulated tracks in 6-h interval from different parameterization schemes for TC Nargis.

Table 4.1: Best combination Selection for TC Nargis simulation

NAME OF EXP.	RMSE OF TC Nargis			BEST EXP.
	Wind ( $\text{ms}^{-1}$ )	SLP (hPa)	Track (km)	
YKF	3.265179	0.782243	0.502412	<b>YKF</b>
YBM	3.618005	2.097618	0.64337	
YGD	4.490867	2.305929	0.918923	
MKF	3.545487	4.053805	1.517197	
MBM	3.545487	3.977915	1.243621	
MGD	4.441189	2.837452	0.86933	

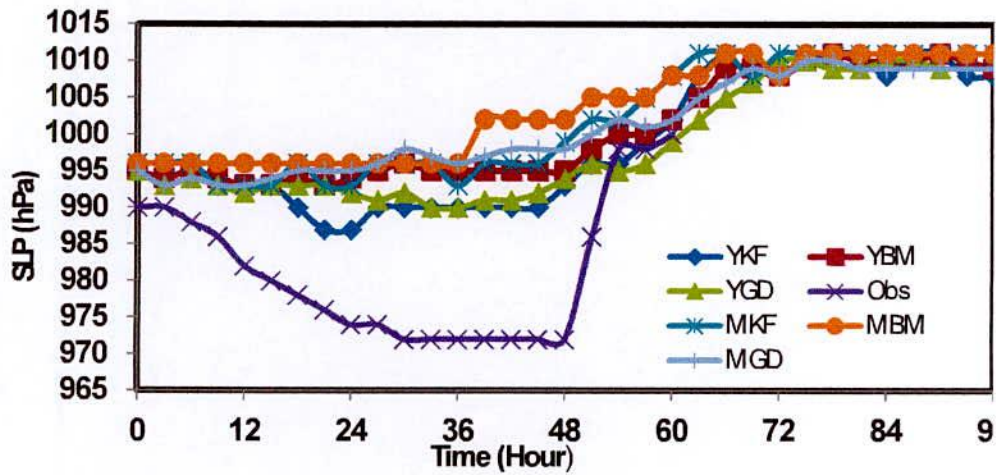


Figure 4.1(d): Time variation of observed & model simulated SLP (hPa) for TC Thane.

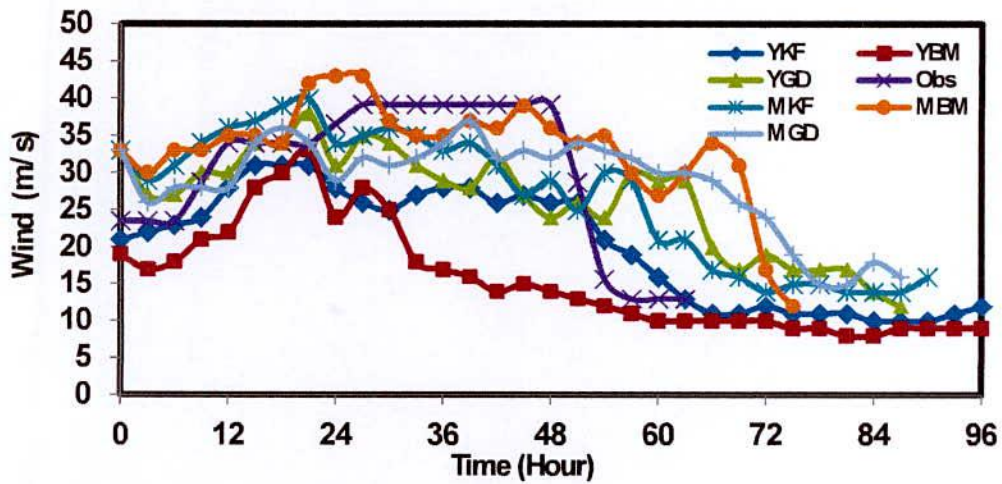


Figure 4.1(e): Time variation of observed & model simulated wind (m/s) for TC Thane.

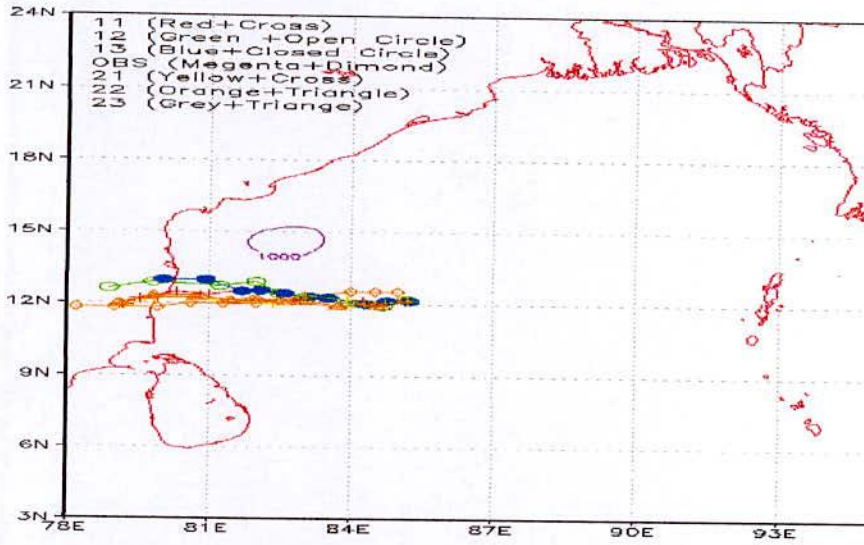


Figure 4.1(f): Model simulated tracks in 6-h interval for TC Thane

Table 4.2: Best combinations Selection for TC Thane simulation.

NAME OF EXP.	RMSE OF TC Thane			BEST EXP.
	Wind ( $\text{ms}^{-1}$ )	SLP (h Pa)	Track (km)	
YKF	1.814948	0.782243	0.19235	YKF
YBM	2.440302	2.097658	0.28256	
YGD	1.990369	2.395929	0.27422	
MKF	2.406541	4.053805	0.22341	
MBM	2.406541	3.977915	0.25101	
MGD	2.892947	2.837252	8.66586	

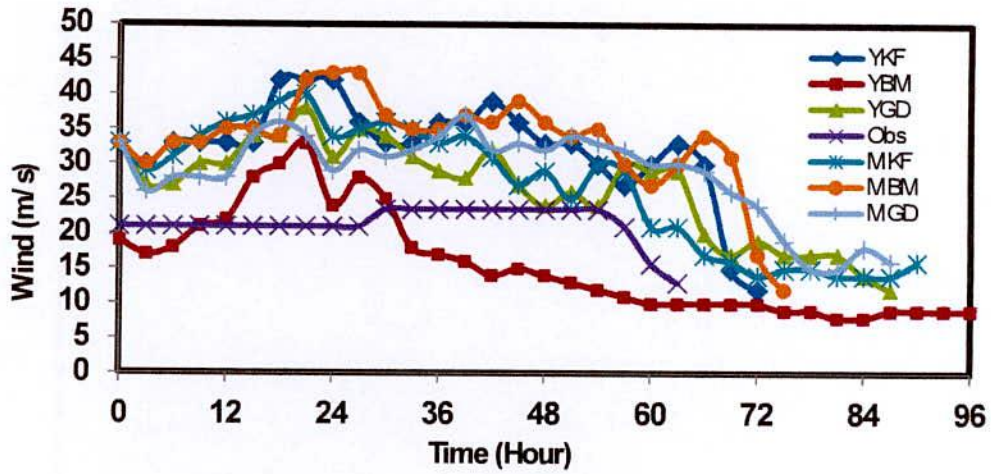


Figure 4.1(g): Time variation of observed & model simulated wind (m/s) for TC Mahasen.

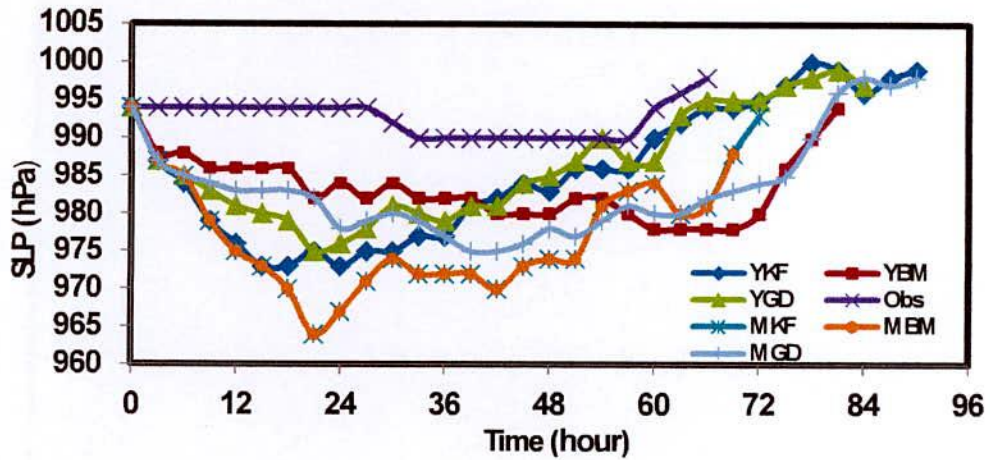


Figure 4.1(h): Time variation of observed & model simulated SLP (hPa) for TC Mahasen.

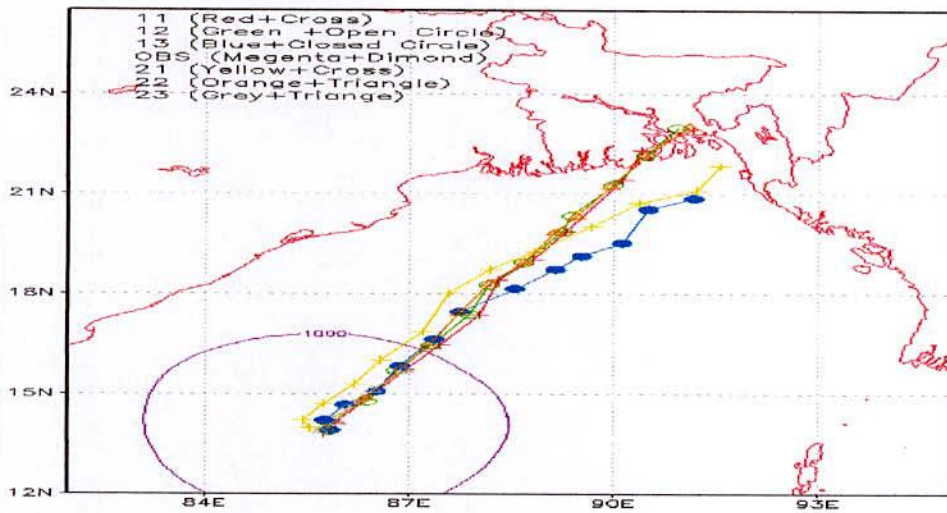


Figure 4.1(j): Model simulated tracks in 6-h interval from different parameterization schemes for TC Mahasen.

Table 4.3: Selection of Best combinations for TC Mahasen.

NAME OF EXP.	RMSE Of TC Mahasen			BEST EXP.
	Wind ( $\text{ms}^{-1}$ )	SLP (hPa)	Track (km)	
YKF	2.973754	0.782243	0.394868	<b>YKF</b>
YBM	1.563753	2.097658	0.540921	
YGD	2.143721	2.395929	0.519803	
MKF	2.46022	4.053805	0.575069	
MBM	2.46022	3.977915	0.544413	
MGD	2.342317	2.837252	0.630277	



## 4.2 Simulation of TC Nargis

To evaluate the structure of TC Nargis the Weather Research Forecasting (WRF) model is run for 96 hours from 29 April 2008 at 00 UTC. After 69 hours on 01 May 2008 at 21 UTC the system attained to state of highest intensity. The model resulted values of different meteorological parameters for the best combination are discussed graphically, numerically and figuratively, in the following subsections, comparing with the available data obtained from Indian Meteorological Department (IMD).

### 4.2.1 Pressure Field

To evaluate the TC intensity, minimum sea level pressure (SLP) plays an important role. It is pretty difficult to find any ratification of model simulated SLP with real observable data from the sea before the landfall as TCs develop over the vast oceanic areas where observations are scant or not available. But now meteorologists are able to estimate SLP and maximum sustained wind (MSW) using interpretations of satellite products. Observed and model simulated SLP of TC Nargis from 00 UTC 29 April 2008 up to 96 hours is presented in Figure 4.2(a).

From the Figure it is seen that model simulated SLP falls gradually with time and attains the peak intensity 960 hPa at 21 UTC on 01 May 2008 and after that increases gradually. Finally just before the landfall the Sea Level Pressure is 961 hPa at 00 UTC on 02 May 2008. The observed SLP remains same for a long time from 03 UTC 29 April to 21 UTC on 01 May 2008. On the other hand the observed peak SLP 962 hPa is obtained at 09 UTC on 02 May 2008 and remains same up to 15 UTC on 02 May 2008 from 09 UTC on 02 May 2008. After that it increases gradually.

The distribution of sea level pressure (SLP) for the TC Nargis at 00 UTC on 29, 30 April & 01 May 2008 and 21 UTC on 01 May 2008 has been shown in Figure 4.2(b) which indicates the same feature as described in Figure 4.2(a).



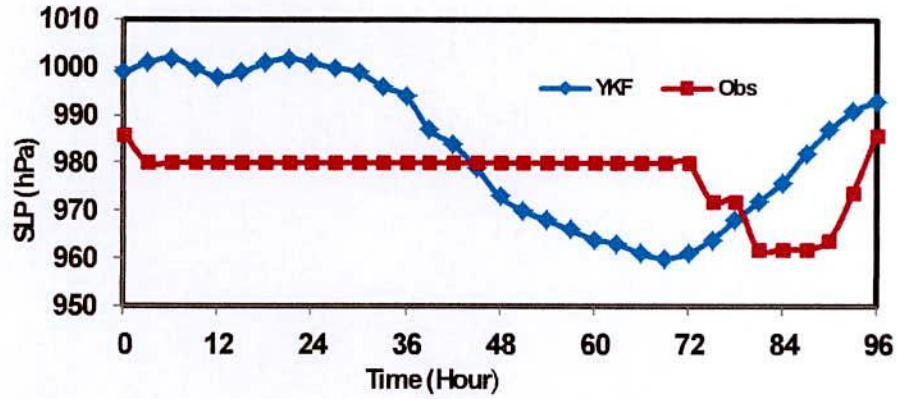


Figure 4.2(a): Time variation of observed & simulated SLP (hPa) for TC Nargis.

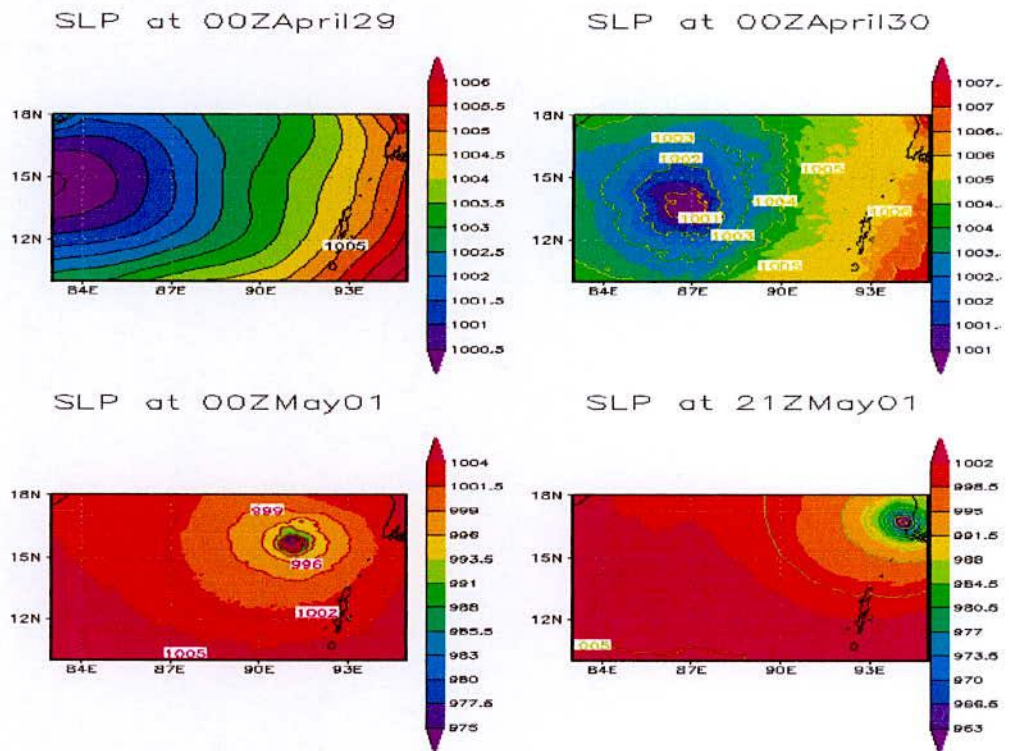


Figure 4.2(b): Distribution of model simulated SLP (hPa) for TC Nargis at 00 UTC on 29, 30 April & 01 May and 21 UTC on 01 May 2008.

## 4.2.2 Wind Field

When the landfall occurs, maximum wind speed (MWS) directly devastates the effected area and it is the most effective force for generating storm, surge over the landfall area. Figure 4.3 (a) shows the time disparities of model simulated MWS and observed wind of TC Nargis. The model simulated MWSs obtained are lower than observed wind upto first 42 hours from the initial and after that it increases from 48 hours upto 75 hours showing a bit oscillation then it falls gradually. Maximum Wind Speed (MWS)  $40 \text{ ms}^{-1}$  is achieved at 21 UTC on 01 May 2008. On the other hands the observed MWS  $45 \text{ ms}^{-1}$  is achieved at 09 UTC on 02 May 2008.

The distribution of surface wind for Nargis at 00 UTC on 29, 30 April & 01 May and 21 UTC on 01 May 2008 has been shown in the Figure 4.3 (b). The Figures show that the pattern has an asymetric wind distribution with strong wind bands at the front left and right sides, close to the centre of north directed moving storm. The wind flow in the core region shows a near circular feature with minimum wind speed at the centre. The maximum wind speed at 00 UTC 29 April is 12 m/s. At 00 UTC on 30 April and 01 May 2008, TC is organized with strong wind band and the wind flow in the core region shows asymetric feature with minimum wind at the centre. The maximum wind at these stages are 14 and 36 m/s. At 21 UTC on 01 May 2008 just before the landfall, the maximum wind is  $40 \text{ ms}^{-1}$ .

The vertical profile of radial, tangential and vertical wind of the system at 00 UTC on 29, 30 April and 01 May and 21 UTC on 01 May 2008 has been shown in the Figures 4.3 (c), (d) and (e) respectively.

Figure 4.3 (c) shows the vertical profile of radial wind at 00 UTC on 29, 30 April & 01 May and 21 UTC on 01 May 2008 which indicates that the system is more organized at 21 UTC on 01 May than 00 UTC on 29, 30 April and it is also clear that the system has strong inflow in the lower level which bring air to the system from the boundary and lower level, and outflow at the upper level.

Figure 4.3 (d) shows the vertical profile of tangential wind at 00 UTC on 29, 30 April & 01 May and 21 UTC on 01 May 2008 which demonstrates that the tangential wind flows

towards northerly directional to the western side of the system and southerly directional at the eastern side.

Figure 4.3 (e) shows the vertical profile of vertical velocity at 00 UTC on 29, 30 April & 01 May and 21 UTC on 01 May 2008 which indicates that vertical velocity of wind changes with the change of time at different levels. It confirms the development of the cyclone.

The horizontal distribution of wind vector and magnitude of the wind field for 850, 500, 300 and 200 hPa levels at 00 UTC on 29, 30 April & 01 May and 21 UTC on 01 May 2008 has been shown in Figures 4.3(f), (g), (h), (i) and (j).

The Figures 4.3(f) and (g) are well organized cyclonic circulation with strong wind encircling the center is found at 850 and 500 hPa levels.

At 300 hPa level, a little bit cyclonic circulation in the right side of the TC and weak outflow at the left which is observed in Figure 4.3 (h).

At 100 hPa level strong outflow from the central part of the cyclone is envisioned in Figure 4.3 (i).

Figure 4.3 (j) shows the vertical profile of horizontal wind of the system at 00 UTC on 29, 30 April & 01 May and 21 UTC on 01 May 2008 which indicates the distribution of strong winds up to 500 hPa level.

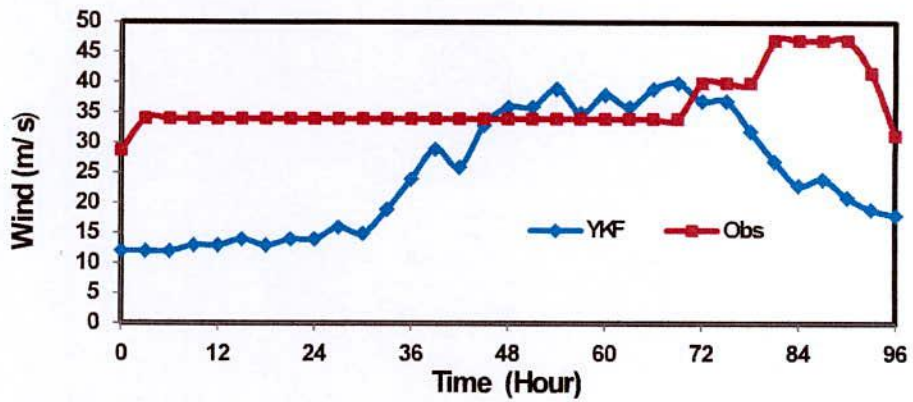


Figure 4.3(a): Time variation of observed and model simulated wind (m/s) for TC Nargis.

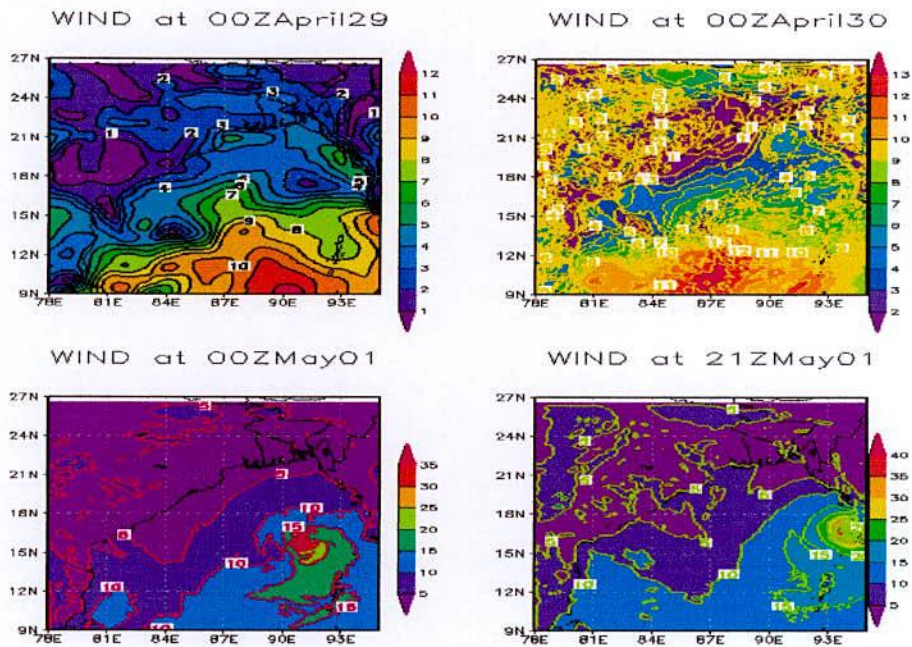


Figure 4.3(b): Surface wind (m/s) distribution for TC Nargis at 00 UTC on 29, 30 April & 01 May and 21 UTC on 01 May 2008.

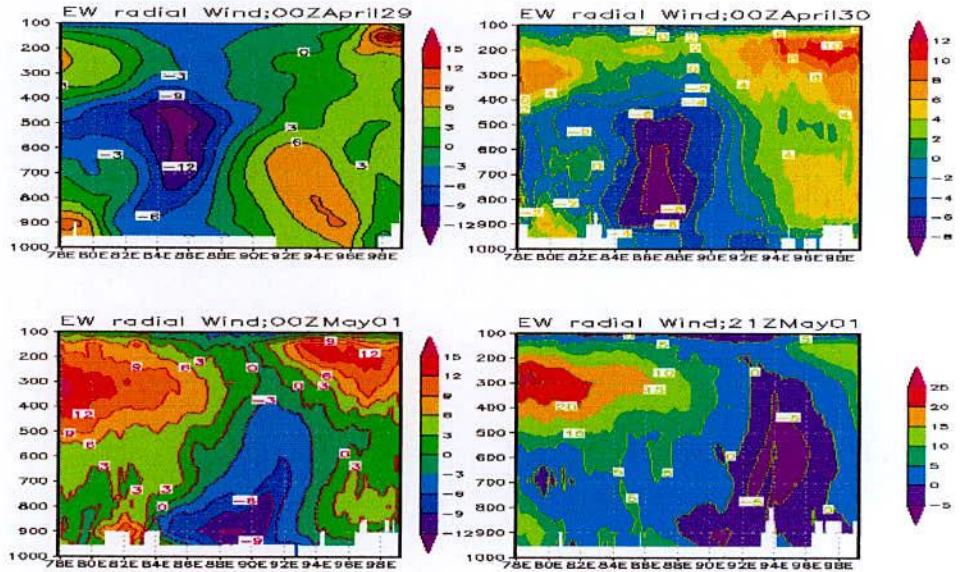


Figure 4.3(c): Model simulated east-west cross section of vertical profile of radial wind (m/s) at 00 UTC on 29, 30 April & 01 May and 21 UTC on 01 May 2008.

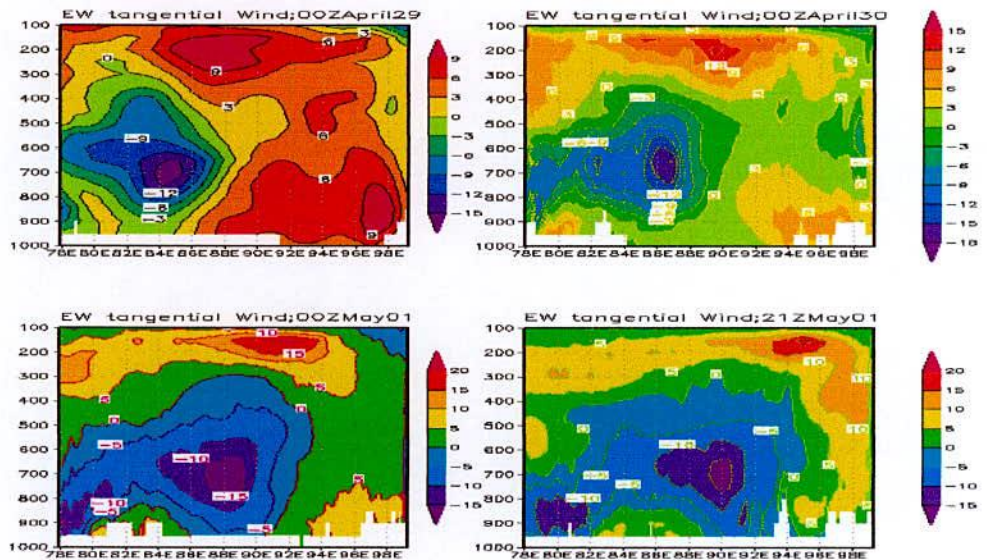


Figure 4.3(d): Model simulated east-west cross section of vertical profile of tangential wind (m/s) at 00 UTC on 29, 30 April & 01 May and 21 UTC on 01 May 2008.

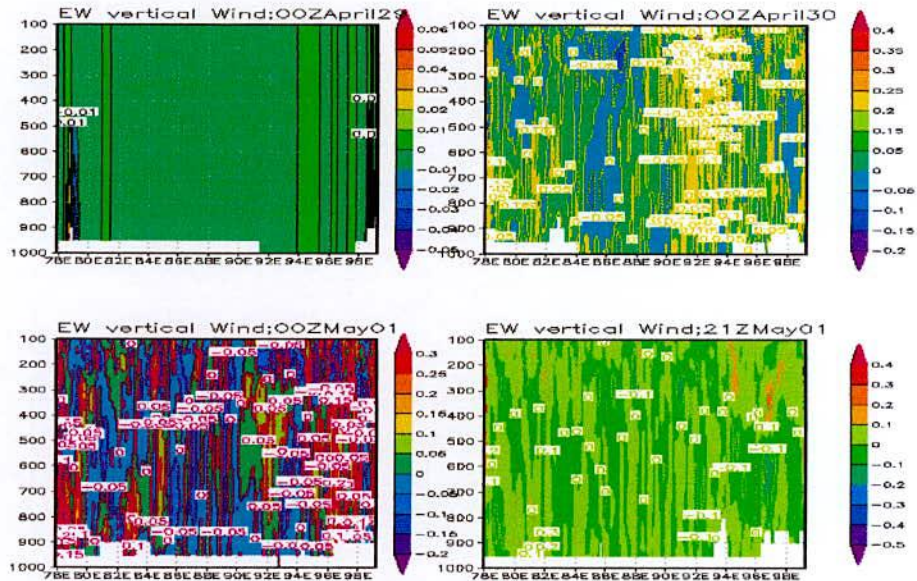


Figure 4.3(e): Model simulated east-west cross section of vertical profile of vertical wind (m/s) at 00 UTC on 29, 30 April & 01 May and 21 UTC on 01 May 2008.

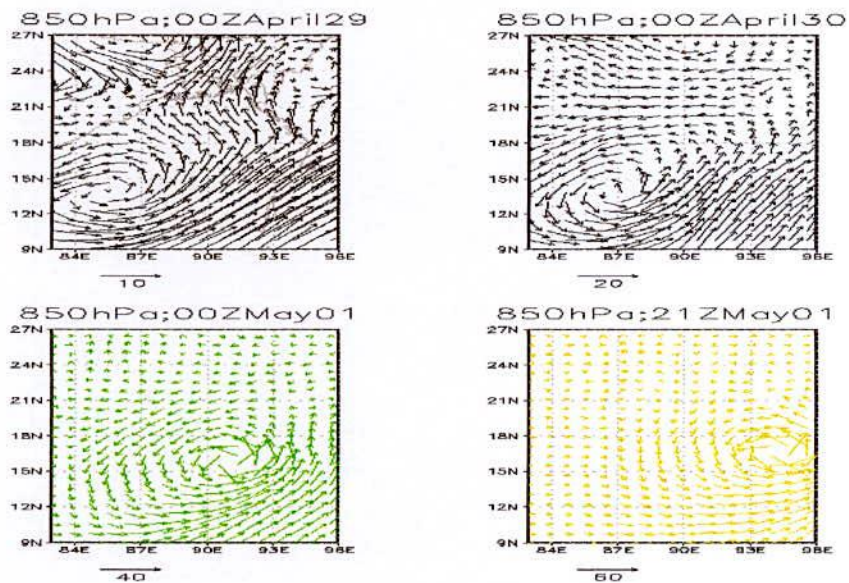


Figure 4.3(f): Model simulated wind vector and magnitude at 00 UTC on 29, 30 April & 01 May and 21 UTC on 01 May 2008 at 850 hPa level.

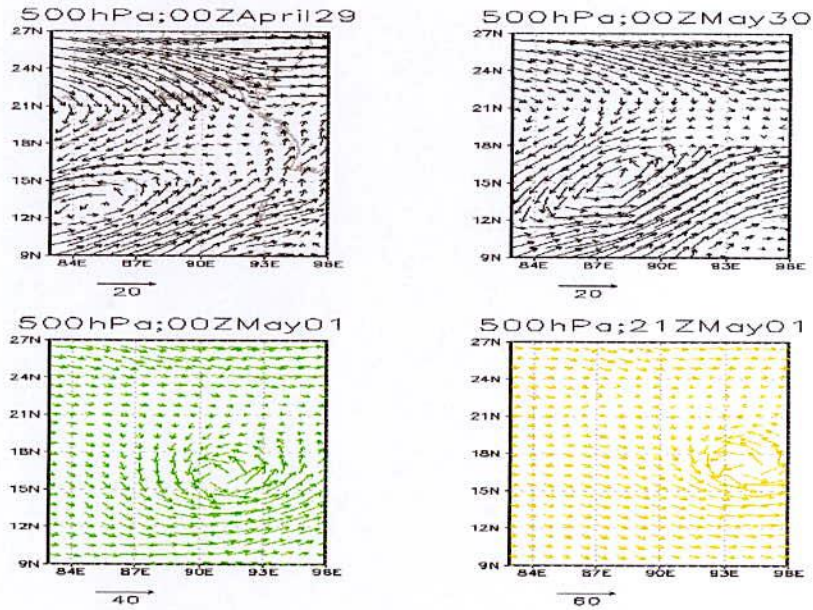


Figure 4.3(g): Model simulated wind vector and magnitude at 00 UTC on 29, 30 April & 01 May and 21 UTC on 01 May 2008 at 500 hPa level.

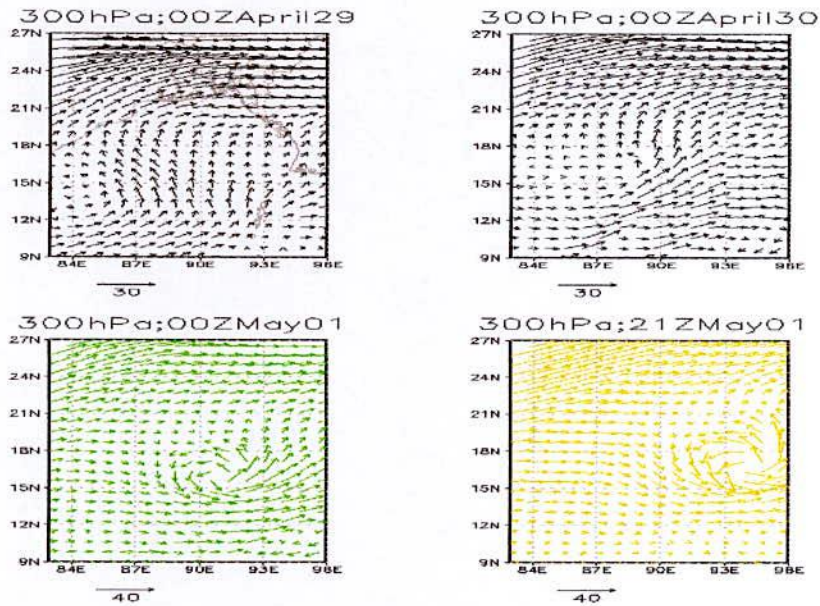


Figure 4.3(h): Model simulated wind vector and magnitude at 00 UTC on 29, 30 April & 01 May and 21 UTC on 01 May 2008 at 300 hPa level.

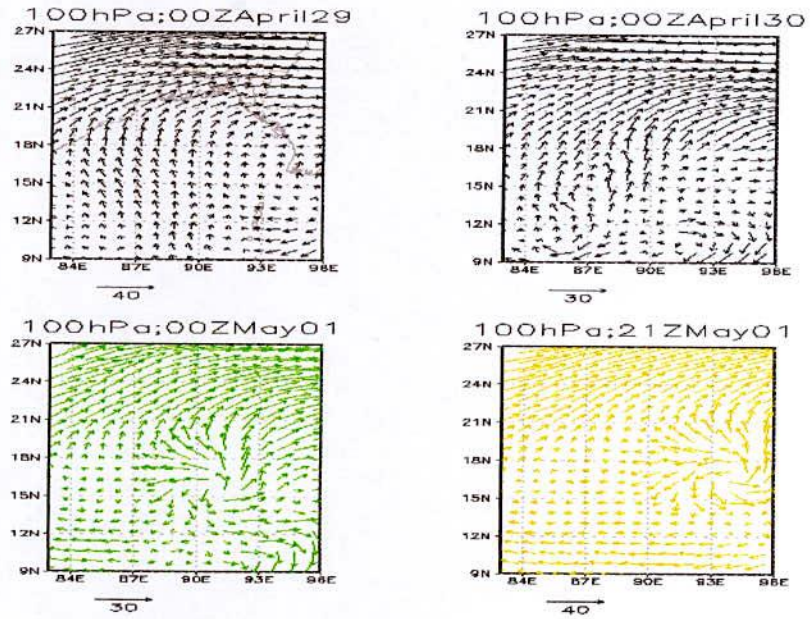


Figure 4.3(i): Model simulated wind vector and magnitude at 00 UTC on 29, 30 April & 01 May and 21 UTC on 01 May 2008 at 100 hPa level.

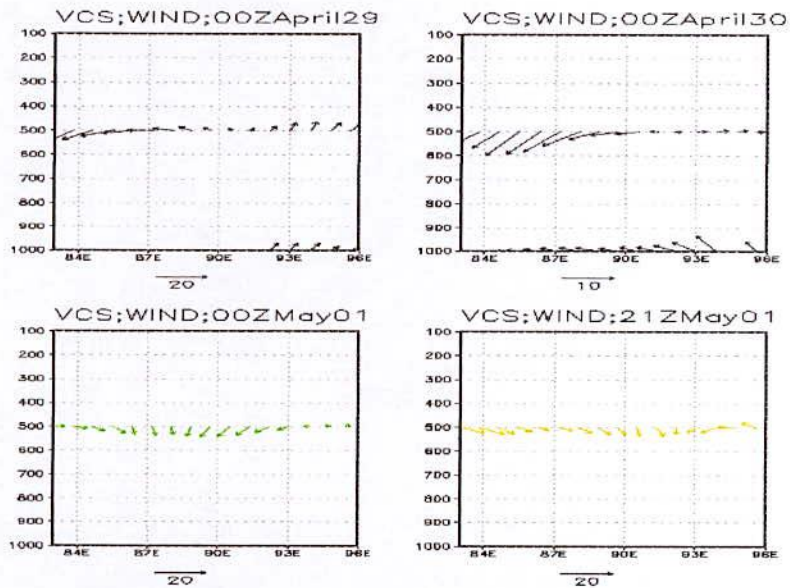


Figure 4.3(j): Model simulated east-west cross section of vertical profile of horizontal wind for TC along the center at 00 UTC on 29, 30 April & 01 May and 21 UTC on 01 May 2008.



### 4.2.3 Vorticity Field

The horizontal distribution of relative vorticity at 00 UTC on 29, 30 April & 01 May and 21 UTC on 01 May 2008 at 850, 500, 300 and 200 hPa levels has been shown in the Figures 4.4(a), (b), (c) and (d) respectively.

It is seen from the Figures that the obtained vorticity is distributed with maximum value at the center. The distribution shows circular pattern with some asymmetric features in the outer periphery except at 00 UTC on 29 April 2008 (i.e, initial time) but symmetric circular pattern is available at all the levels in the inner side of the centre.

At 850 hPa level, shown in Figure 4.4 (a) indicates that the negative vorticity is found almost every sides which is followed by a positive and negative vorticity fields at 21 UTC on 01 May 2008. Similar phenomena are found at 00 UTC on 29, 30 April and 01 May 2008. The distance of the negative vorticity fields from the center are increased due to intensification of the intensity. Low level vorticity fields confirm the strong cyclonic circulation with different value of the radius at different time in feeding moisture into the system to sustain its intensity. After that the development of the cyclone has been enhanced.

At 500, 300 and 100 hPa levels the distribution of relative vorticity shows a symmetric character in the horizontal direction. At 500 and 300 hPa levels the distribution of relative vorticity shows a symmetric character in the horizontal direction which has been shown in Figures 4.4(b) and (c). At 00 UTC on 29 April 2008 a core of positive relative vorticity is found to be formed at the 500 hPa level. On the other hand at 21 UTC on 01 May 2008 an embedded core of positive relative vorticity is found to be formed at the 500 hPa level.

The values of relative vorticity are increased with the intensification of the intensity of the cyclone and then decreased before landfall.

A weak positive vorticity embedded with negative vorticity field is visible at 100 hPa level shown in Figure 4.4(d). At this level vorticity diversifies to the either direction of the level which confirms the mature development of negative vorticity of the cyclone.

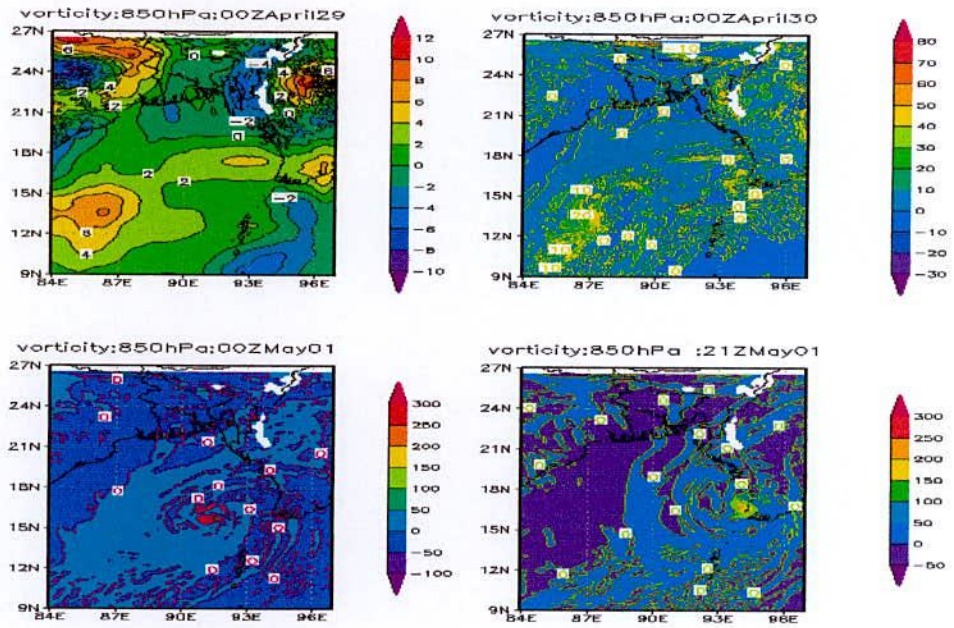


Figure 4.4(a): Model simulated vorticity field at 00 UTC on 29, 30 April & 01 May and 21 UTC on 01 May 2008 at 850 hPa level.

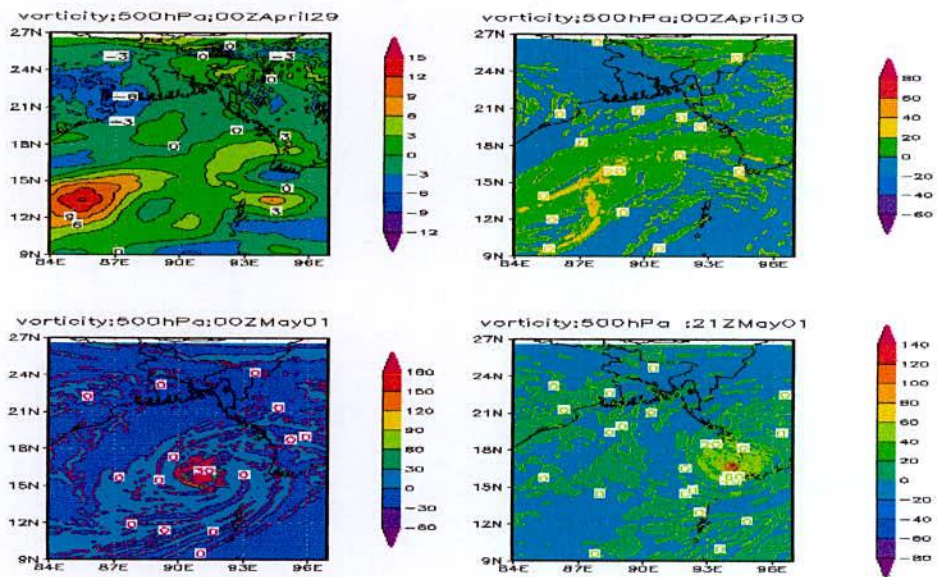


Figure 4.4(b): Model simulated vorticity field 00 UTC on 29, 30 April & 01 May and 21 UTC on 01 May 2008 at 500 hPa level.

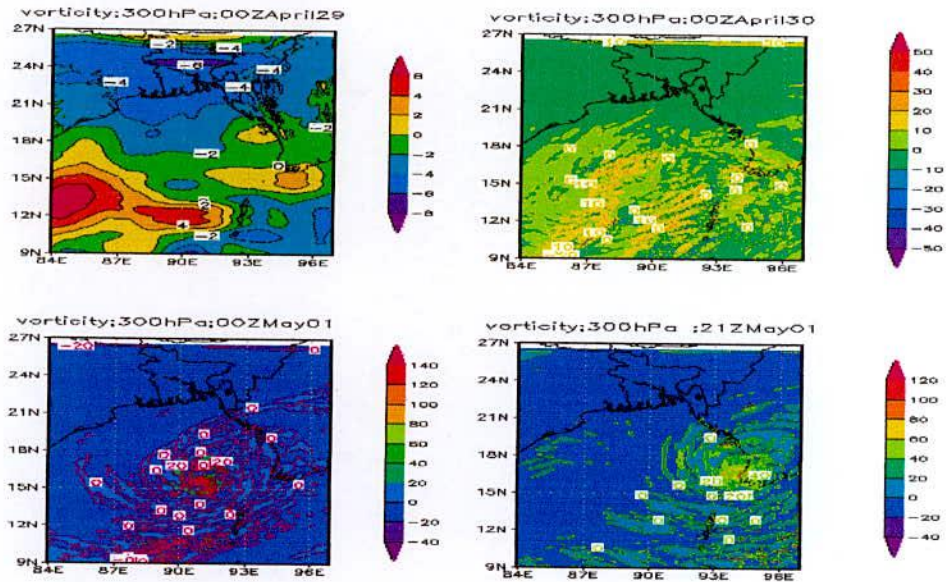


Figure 4.4(c): Model simulated vorticity field at 00 UTC on 29, 30 April & 01 May and 21 UTC on 01 May 2008 at 300 hPa level.

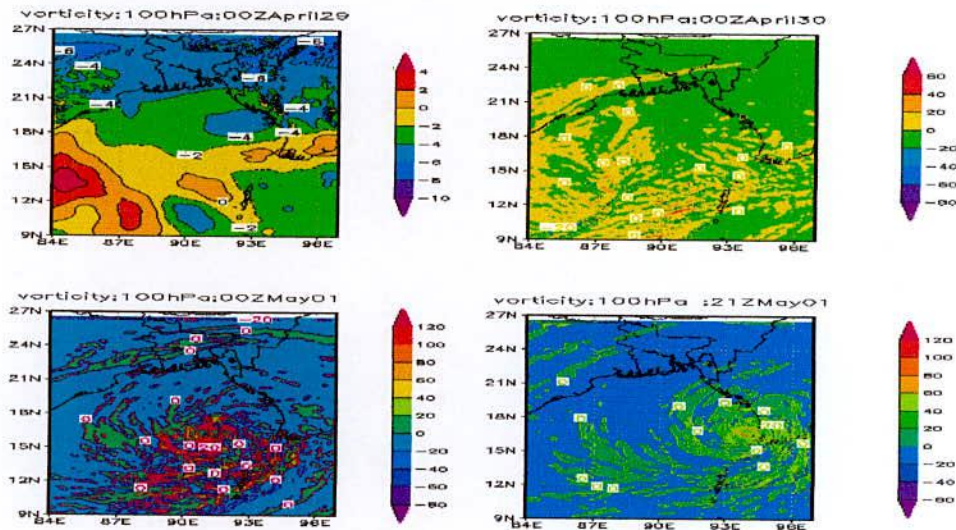


Figure 4.4(d): Model simulated vorticity field at 00 UTC on 29, 30 April & 01 May and 21 UTC on 01 May 2008 at 100 hPa level.

## 4.2.4 Temperature Anomaly

The model simulated temperature anomaly of TC Nargis at 00 UTC on 29, 30 April & 01 May and 21 UTC on 01 May 2008 (before the landfall) from surface to 100 hPa levels has been shown in the Figure 4.5.

At 00 UTC on 29 April 2008, 5<sup>0</sup>C warm core is observed in the layer between 950 - 700 hPa levels. It is seen that the warm core is slightly expanded outward at 900-750 hPa level. The highest anomaly is formed around 900 and 750 hPa levels. The simulated anomaly demonstrates that the warm core is visible in the lower troposphere and negative anomaly at the middle levels. At the upper levels very low anomaly is visualized.

At 00 UTC on 30 April 2008, several 3<sup>0</sup>C warm cores are observed in the layer between 900 - 150 hPa. The highest anomaly is formed around 850 and 200 hPa levels. The simulated anomaly demonstrates that the warm core is visible in the upper and lower troposphere and negative anomaly at the middle levels.

At 00 UTC on 01 May 2008, 3<sup>0</sup>C warm core is observed in the layer between 950- 200 hPa levels. The highest anomaly is formed around 900 and 200 hPa levels and expanded at the outer perimeter. The simulated anomaly demonstrates that the warm core is visible in the upper and lower troposphere and negative anomaly is embedded at the middle and lower levels.

At 21 UTC on 01 May 2008, 12<sup>0</sup>C warm core is observed in the layer between 450- 150 hPa levels. The highest anomaly is formed around 300 hPa level. The simulated anomaly demonstrates that the warm core is visible in the upper troposphere and negative anomaly at the middle levels. Again at the lower levels the positive anomaly is embedded. It is also seen that the negative anomaly is slightly expanded to the inner perimeter.

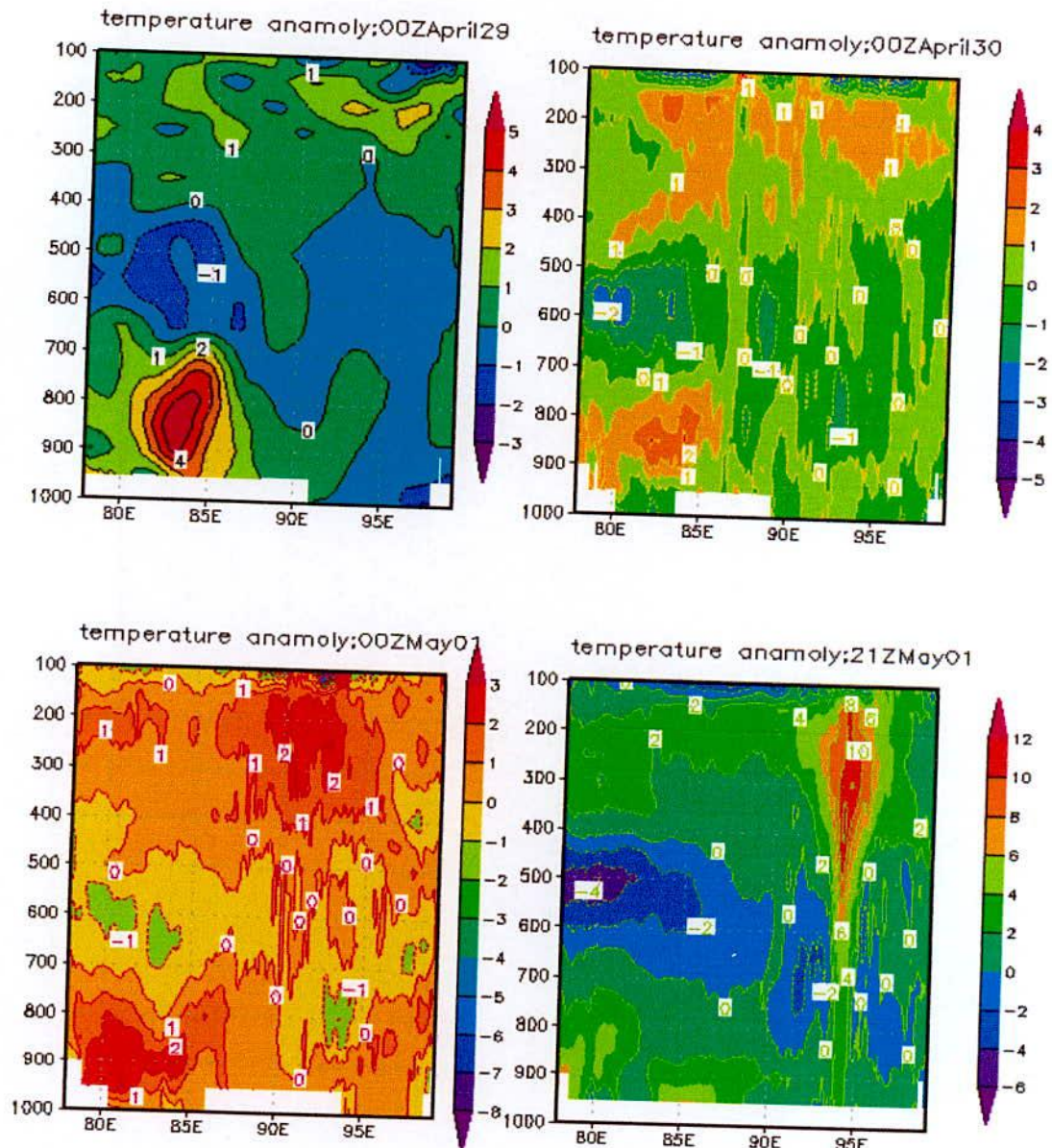


Figure 4.5: Vertical distribution of temperature anomaly in the east-west direction through the centre at 00 UTC on 29, 30 April & 01 May and 21 UTC on 01 May 2008.

## 4.2.5 Water Vapor Mixing Ratio

The model simulated vertical distribution of water vapor mixing ratio along the east-west cross section of the center of TC Nargis at 00 UTC on 29, 30 April & 01 May and 21 UTC on 01 May (before the landfall) 2008 from surface to 100 hPa levels has been shown in Figure 4.6. It is observed that the highest water vapor mixing ratio around  $2.2 \times 10^{-2}$  kg/kg or more is found at the centre of the system at 950 hPa level and it decreases upwards to 400 hPa level. It is seen that moisture content distribution has shifted towards eastward with the progress of time.

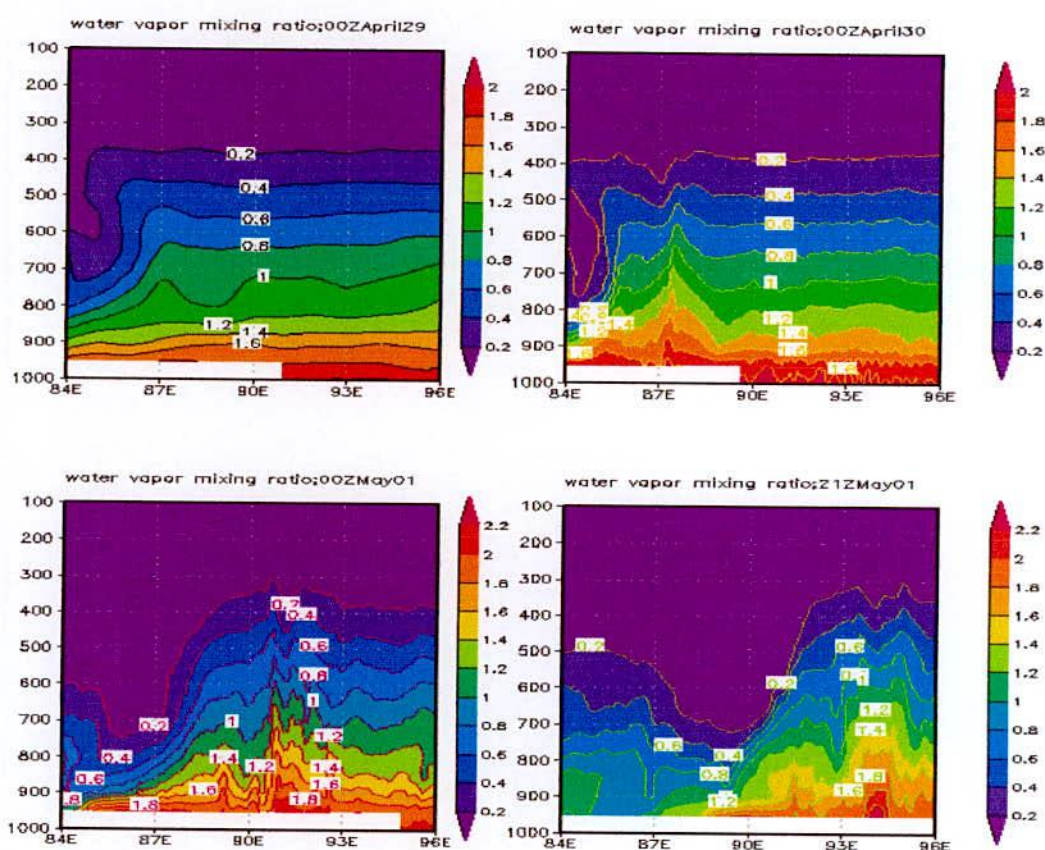


Figure 4.6: Vertical distribution of water vapor mixing ratio in the east-west direction through the centre at 00 UTC on 29, 30 April & 01 May and 21 UTC on 01 May 2008.

## 4.2.6 Rainfall Pattern

Model simulated 24 hours accumulated rainfall of TC Nargis for the day 29, 30 April and 01 May 2008 (i.e, ending at 00 UTC on 30 April, 01 and 02 May 2008) has been shown in the Figure 4.7.

On 29 April 2008, the rainfall occurs mainly in the sea. On 30 April 2008, the rainfall occurs mainly in the sea and south eastern part of Bangladesh. On 01 May 2008, the rainfall occurs in the south eastern part of Bangladesh.

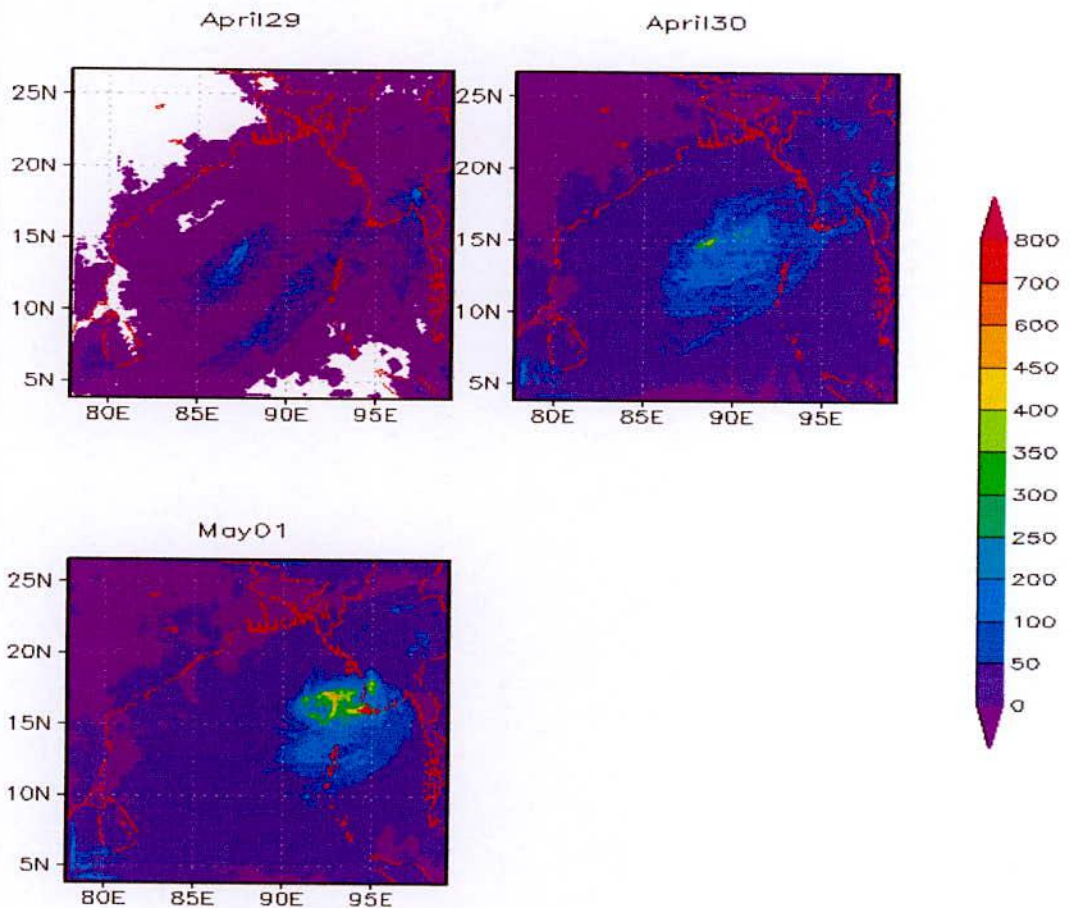


Figure 4.7: 24- hours accumulated rainfall (mm) of TC Nargis for the day 29 & 30 April and 01 May 2008.

## 4.2.7 Track Pattern

The model simulated and observed track of TC Nargis are plotted in the Figure 4.8. It is visualized from the figure that the model simulated tracks for six selected combination are parallel along with the observed track but other than the YKF simulated track rest of the simulated tracks have been deviated maximum north or south side of the observed track all along the journey from the initial to the landfall. Initially all the simulated tracks have deviated at the north. It may be because of initial data error. It reveals that simulated track using YKF combination is obtained more close to the IMD best track than all other simulated tracks. The numerical calculation (shown in Table 4.1) shows that the average track error using YKF combination is 50 km which is least than any other simulated combination.

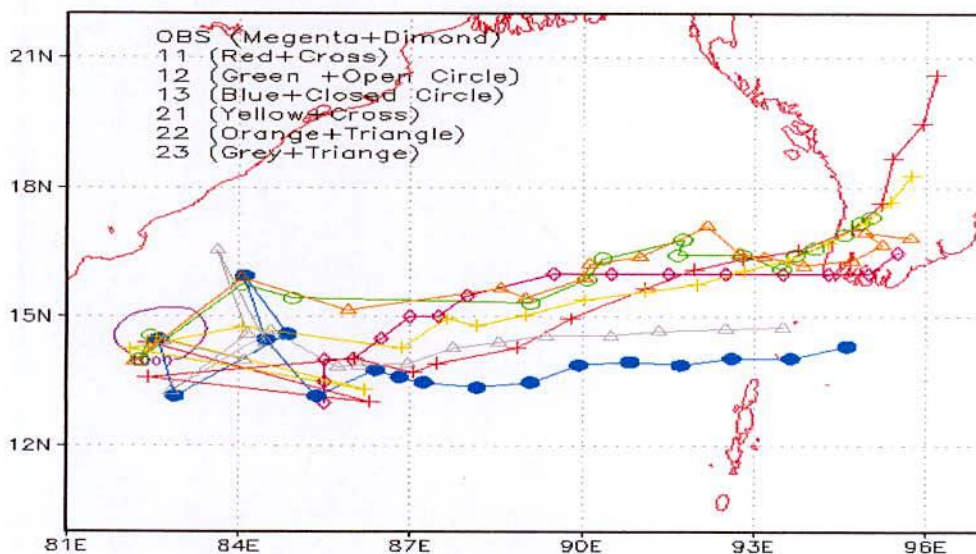


Figure 4.8: Model simulated tracks in 6-h interval for TC Nargis.



## 4.3 Simulation of TC Thane

To evaluate the structure of TC Thane the WRF model is run for 96 hours from 28 December 2011 at 00 UTC. After 21 hrs on 28 December 2011 at 21 UTC the system attains to state of highest intensity. To evaluate the structure of TC Thane the model resulted values of different meteorological parameters using the best combination are discussed graphically, numerically and figuratively in the following subsections comparing with the available data obtained from Indian Meteorological Department (IMD).

### 4.3.1 Pressure Field

To evaluate the TC intensity, minimum sea level pressure (SLP) plays an important role. It is pretty difficult to find any ratification of model simulated MSLP with real observable data from the sea before the landfall as TCs develop over the vast oceanic areas where observations are scant or not available. But now meteorologists are able to estimate SLP and maximum sustained wind (MSW) using interpretations of satellite products. Observed and model simulated SLP of TC Thane from 00 UTC on 28 December 2011 up to 96 hours is presented in the Figure 4.9(a). Model simulated SLP falls gradually with time and attains the peak intensity 987 hPa at 21 UTC on 28 December 2011 and 00 UTC on 29 December 2011 respectively and after that SLP gradually increases. It is observed that the simulated SLP remains same from 03 UTC 29 December 2011 to 21 UTC on 29 December 2011. Finally just before the landfall the SLP is 993 hPa at 00 UTC on 30 December 2011. On the other hand the observed peak SLP 972 hPa is obtained at 00 UTC on 29 December and remain same up to 12 UTC 29 December 2011 and after that it shows a very rapid increase up to a certain period of time at 21 UTC on 29 December 2011.

The distribution of sea level pressure (SLP) for the TC Thane at 00 UTC on 28, 29 & 30 and 18 UTC on 29 December 2011 has been shown in Figure 4.9(b) which reveals the same feature as described in the Figure 4.9(a).

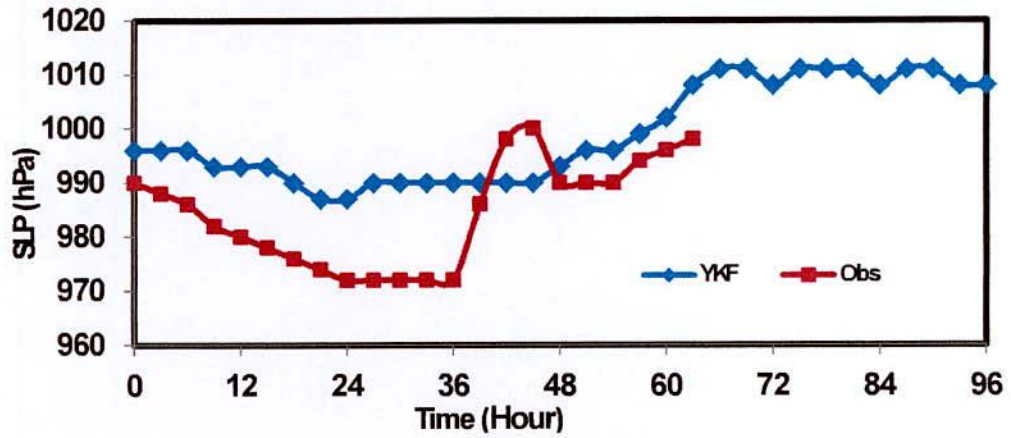


Figure 4.9(a): Time variation of observed & simulated SLP (hPa) for TC Thane.

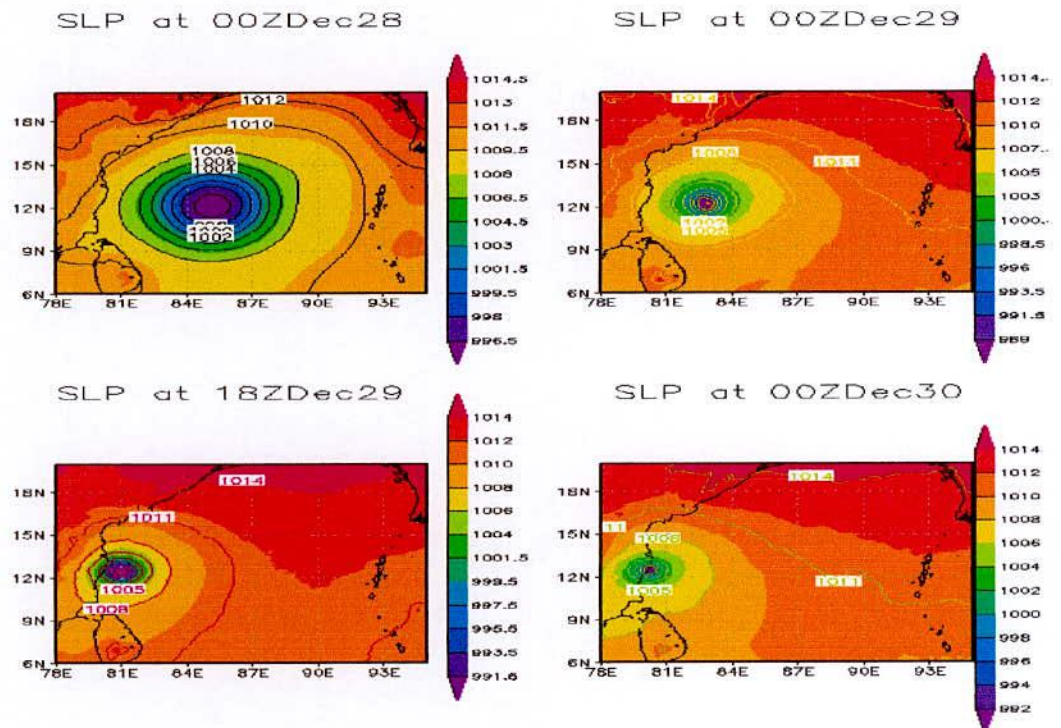


Figure 4.9(b): Distribution of model simulated SLP (hPa) for TC Thane at 00 UTC on 28, 29 & 30 December and 18 UTC on 29 December 2011.

### 4.3.2 Wind Field

When the landfall occurs, maximum wind speed (MWS) directly devastates the effected area and it is the most effective force for generating storm and surge over the landfall area. The model simulated MWSs obtained are lower than observed wind up to first 48 hours from the initial and after that it increases from 48 hours upto 66 hours showing a bit oscillation then it falls gradually. Figure 4.10 (a) shows the time variations of model simulated MWS and observed wind of TC Thane. The model simulated MWSs obtained are lower in most of the cases except some deviation at 00 UTC on 28, 29 & 30 December 2011 and 18 UTC on 29 December 2011 from the observed values.

The distribution of surface wind for Thane at 00 UTC on 28, 29 & 30 December 2011 and 18 UTC on 29 December 2011 (before landfall) has been shown in the Figure 4.10(b). The Figure shows that the pattern has an asymmetric wind distribution with strong wind bands at the front left and right sides, close to the centre of north directed moving storm. The wind flow in the core region shows a near circular feature with minimum wind speed at the centre. The maximum wind speed at this time is 20 m/s. At 00 UTC on 28 and 29 December 2011, TC is organized with strong wind band around and the wind flow in the core region shows asymmetric feature with minimum wind at the centre. The maximum wind at this stages are 26 and 24 m/s. At 18 UTC on 30 December 2011 just before the landfall, the maximum wind is  $12 \text{ ms}^{-1}$ .

Simulated Maximum Wind Speed (MWS)  $40 \text{ ms}^{-1}$  is achieved at 06 UTC on 28 December 2011 on the other hands the observed MWS  $25 \text{ ms}^{-1}$  is achieved at 00 UTC on 29 December 2011.

The horizontal distribution of wind vector and magnitude of the wind field for 850, 500, 300 and 200 hPa at 00 UTC on 28, 29 & 30 December 2011 and 18 UTC on 29 December 2011 has been shown in Figures 4.10 (c), (d), (e) and (f).

The Figures 4.10 (c) and (d) show that a well organized cyclonic circulation with strong wind encircling the center with a little outflow at the right is found at 850 and 500 hPa levels.

At 300 hPa level wind shows a little bit cyclonic circulation in the lower left side of the TC and strong outflow at the upper left which is shown in Figure 4.10 (e).

At 100 hPa level strong outflow is seen from the central part of the cyclone at 00 UTC on 28, 29 & 30 December 2011 and 18 UTC (before landfall) on 29 December 2011 shown in the Figure 4.10(f).

Figure 4.10(j) shows the vertical profile of horizontal wind of the system at 00 UTC on 28, 29 & 30 December 2011 and 18 UTC (before landfall) on 29 December 2011 which indicates that the distribution of strong wind up to 500 hPa level. At the upper levels there is no cyclonic wind.

The vertical profile of radial, tangential, vertical velocity and horizontal wind of the system at 00 UTC on 28, 29 & 30 December 2011 and 18 UTC (before landfall) on 29 December 2011 has been shown in the Figures 4.10(g), (h), (i) and (j) respectively.

Figure 4.10(g) shows the vertical profile of radial wind at 00 UTC on 28, 29 & 30 December and 18 UTC (before landfall) on 29 December 2011 which indicates that the system is more organised at 00 and 18 UTC on 29 December than 00 UTC on 28 & 29 December and it is also clear that the system has strong inflow in the lower level which bring air to the system from the boundary and lower level and outflow at the upper level. It is observed several intensified wind core to form between 1000 to 850 hPa level and 400 to 200 hPa level respectively at 00 UTC on 28 and 29 December 2011. An extended and intensified wind core is formed from 1000 to 400 hPa level.

Figure 4.10(h) shows the vertical profile of tangential wind at 00 UTC on 28, 29 & 30 December and 18 UTC (before landfall) on 29 December 2011 which demonstrates that the tangential wind flows towards northerly direction to the western side of the system and southerly direction at the eastern side. It is observed an intensified wind core to form between 1000 to 500 hPa level and 950 to 300 hPa level respectively at 00 UTC on 28 and 29 December 2011.

Figure 4.10(i) shows the vertical profile of vertical velocity at 00 UTC on 28, 29 & 30 December and 18 UTC (before landfall) on 29 December 2011 which indicates that

vertical velocity of wind changes with the change of time at different levels. It confirms the development of the cyclone.

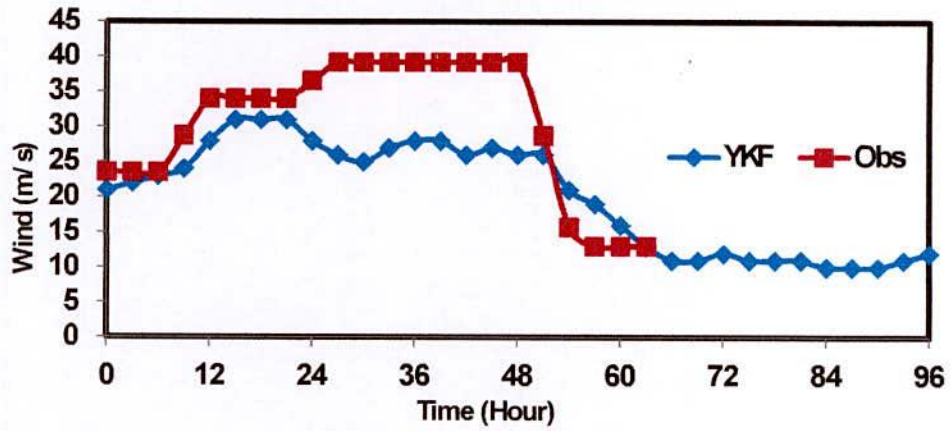


Figure 4.10(a): Time variation of observed & model simulated wind (m/s) for TC Thane.

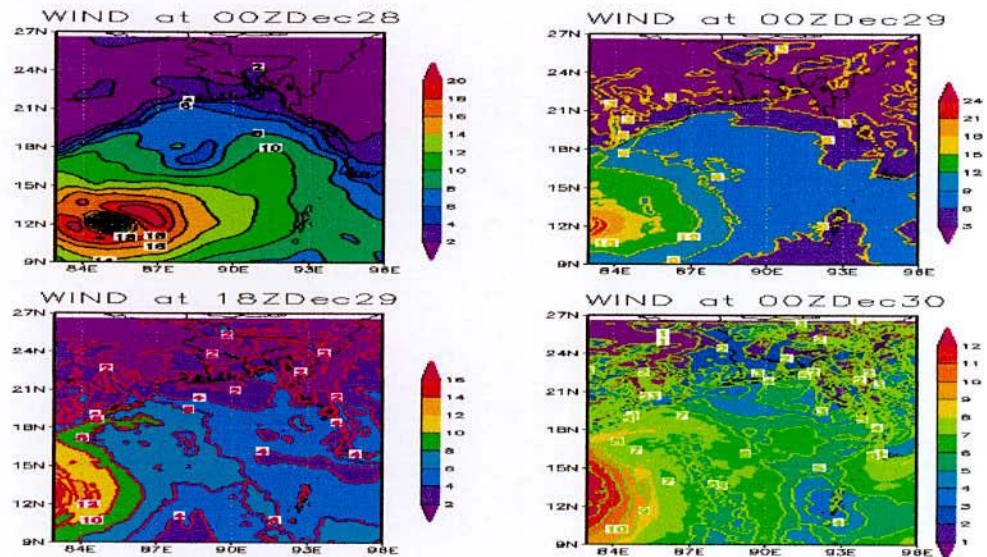


Figure: 4.10(b): Surface wind (m/s) distribution at 00 UTC on 28, 29 & 30 December and 18 UTC on 29 December 2011.

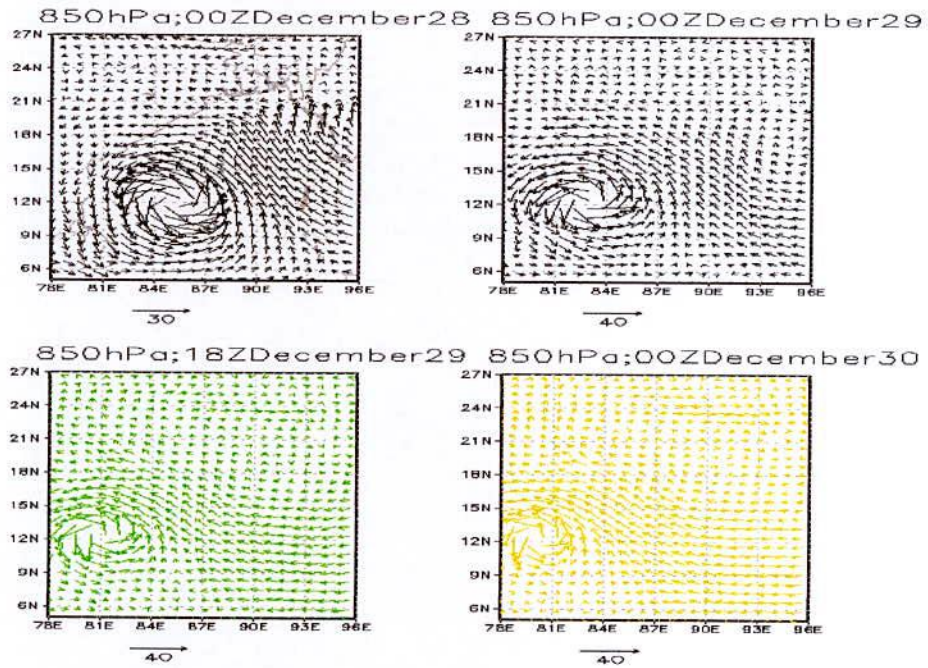


Figure 4.10(c): Model simulated wind vector and magnitude at 00 UTC on 28, 29 & 30 December and 18 UTC on 29 December 2011 at 850 hPa level.

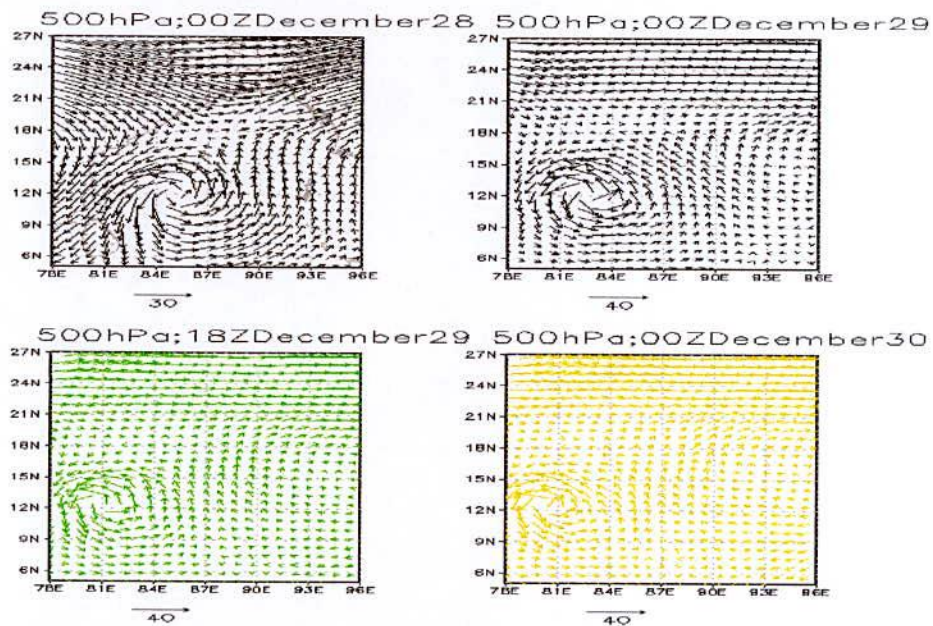


Figure 4.10(d): Model simulated wind vector and magnitude at 00 UTC on 28, 29 & 30 December and 18 UTC on 29 December 2011 at 500 hPa level.

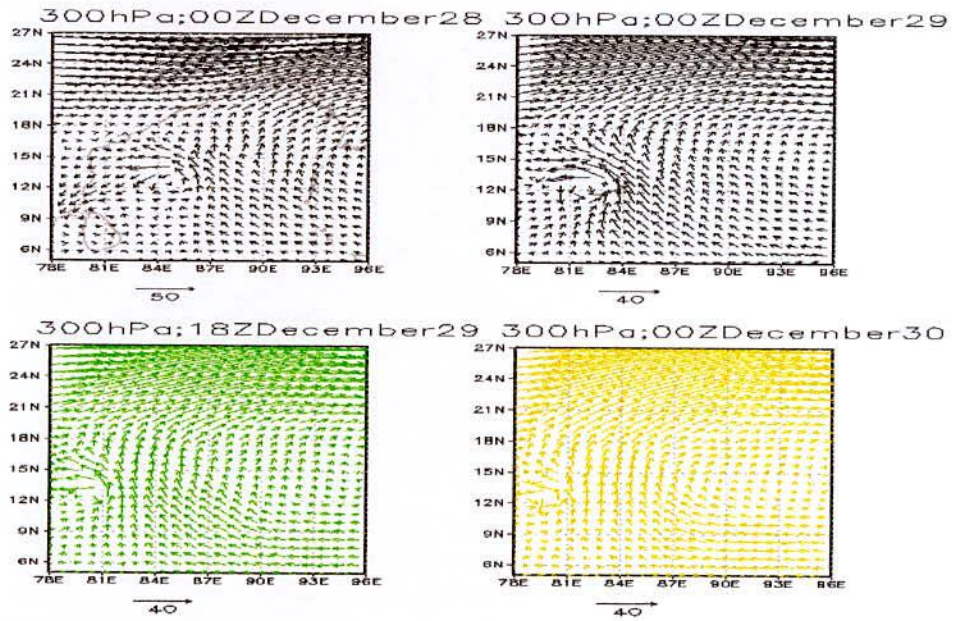


Figure 4.10(e): Model simulated wind vector and magnitude at 00 UTC on 28, 29 & 30 December and 18 UTC on 29 December 2011 at 300 hPa level.

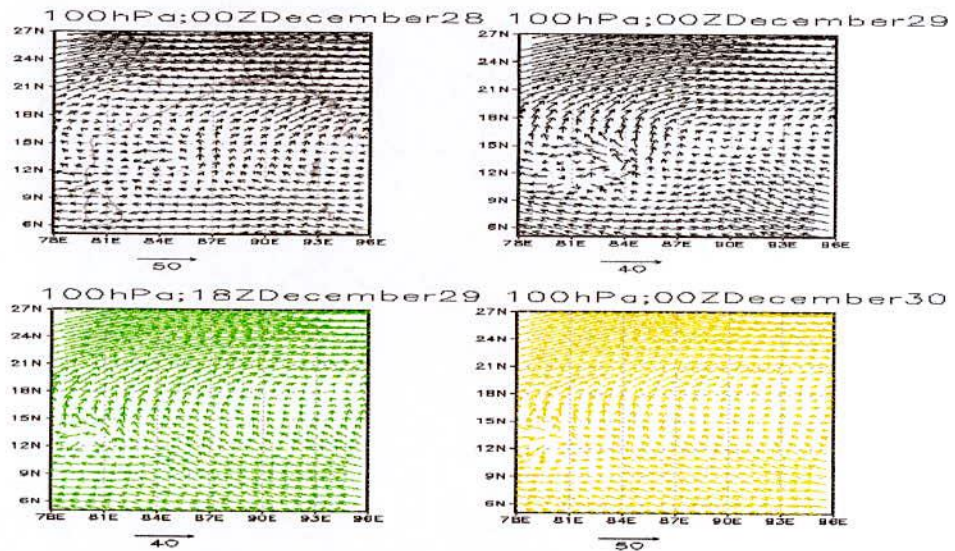


Figure 4.10(f): Model simulated wind vector and magnitude at 00 UTC on 28, 29 & 30 December and 18 UTC on 29 December 2011 at 100 hPa level.

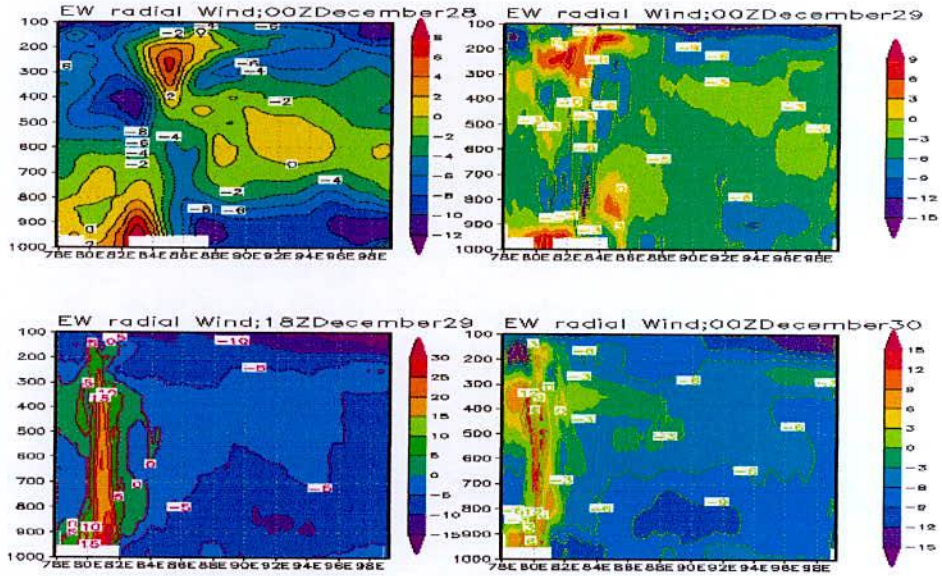


Figure 4.10(g): Model simulated east-west cross section of vertical profile of radial wind at 00 UTC on 28, 29 & 30 December and 18 UTC on 29 December 2011.

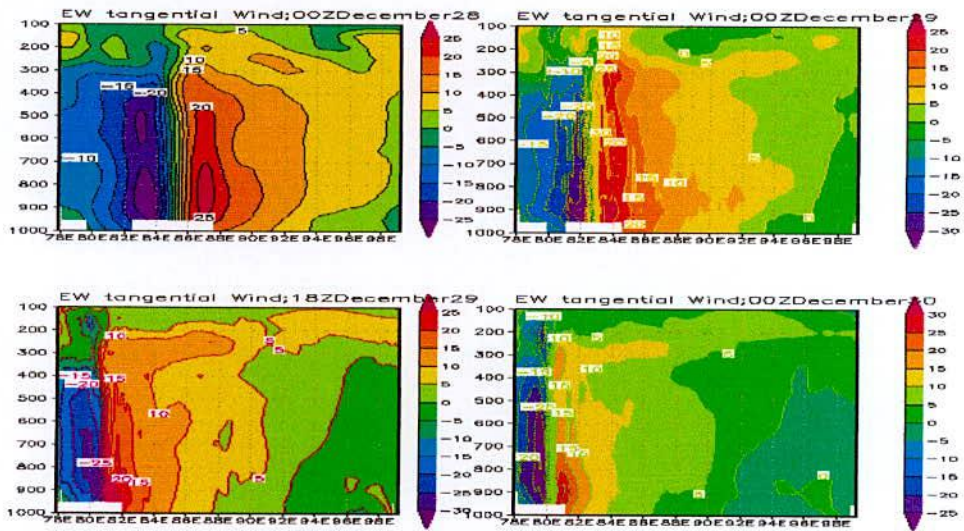


Figure 4.10(h): Model simulated east-west cross section of vertical profile of tangential wind at 00 UTC on 28, 29 & 30 December and 18 UTC on 29 December 2011.



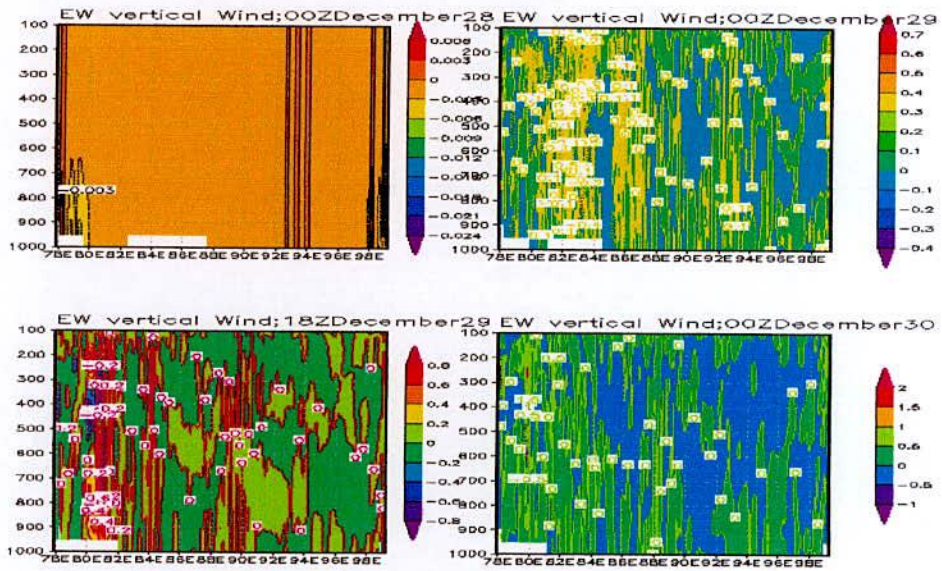


Figure 4.10(i): Model simulated east-west cross section vertical profile of vertical wind at 00 UTC on 28, 29 & 30 December and 18 UTC on 29 December 2011.

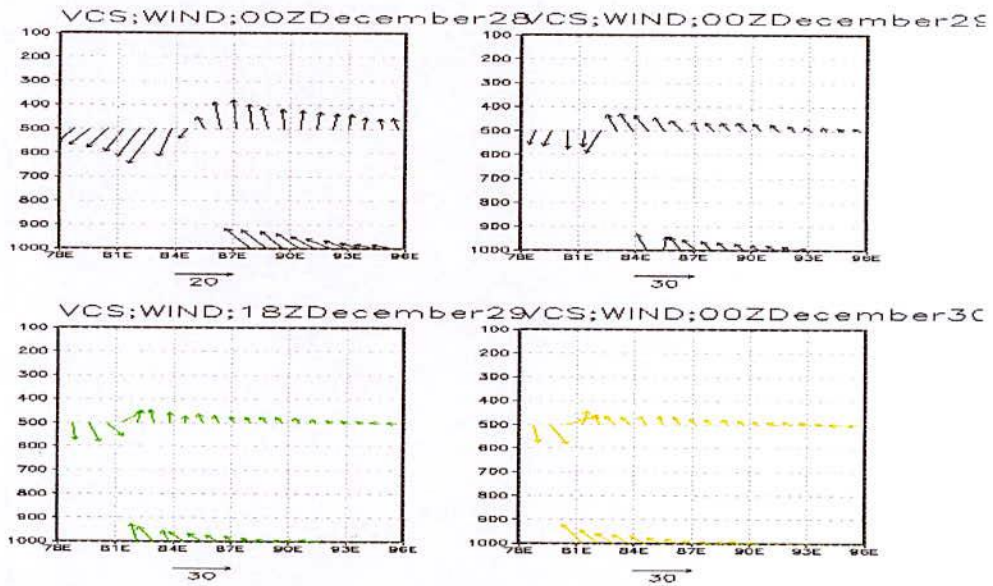


Figure 4.10 (j): Model simulated east-west cross section of vertical profile of horizontal wind at 00 UTC on 28, 29 & 30 December and 18 UTC on 29 December 2011.

### 4.3.3 Vorticity Field

The horizontal distribution of relative vorticity at 00 UTC on 28, 29 & 30 December and 18 UTC on 29 December 2011 at 850, 500, 300 and 100 hPa levels has been shown in the Figures 4.11(a), (b), (c) and (d) respectively.

It is seen from the Figures that the obtained vorticity is distributed with maximum value at the center. The distribution shows circular pattern with some asymmetric features in the outer periphery except at 00 UTC on 28 December 2011 (i.e, initial time) but symmetric circular pattern is available at all the levels in the inner side of the centre.

At 850 hPa level, shown in Figure 4.11 (a) negative vorticity is found almost every sides except the center which is followed by a positive and negative vorticity fields at 18 UTC on 29 December 2011. Similar phenomena are found at 00 UTC on 28, 29 and 30 December 2011. The distance of the negative vorticity fields from the center are increased due to intensification of the intensity. On the other hand at 18 UTC on 29 December 2011 an embedded core of positive relative vorticity is found to be formed at the 850 hPa level. At Low level vorticity fields confirm the strong cyclonic circulation with different value of the radius at different time in feeding moisture into the system to sustain its intensity. At 500, 300 and 100 hPa levels the distribution of relative vorticity shows a symmetric character in the horizontal direction.

At 500 and 300 hPa levels the distribution of relative vorticity shows a symmetric character in the horizontal direction which has been shown in the Figures 4.11 (b) and (c). The values of relative vorticity are increased with the intensification of the intensity of the cyclone and then decreased before landfall. At 00 UTC on 28 December 2011 a core of positive relative vorticity is found to be formed at the 500 hPa level. On the other hand at 18 UTC on 29 December 2011 an embedded core of positive relative vorticity is found to be formed at the 500 hPa level. The values of relative vorticity are increased with the intensification of the intensity of the cyclone and then decreased before landfall. A weak positive vorticity embedded with negative vorticity field is visible at 100 hPa level shown in Figure 4.11 (d). At this level vorticity diversifies to the either direction of the level which confirms the mature development of negative vorticity of the cyclone.

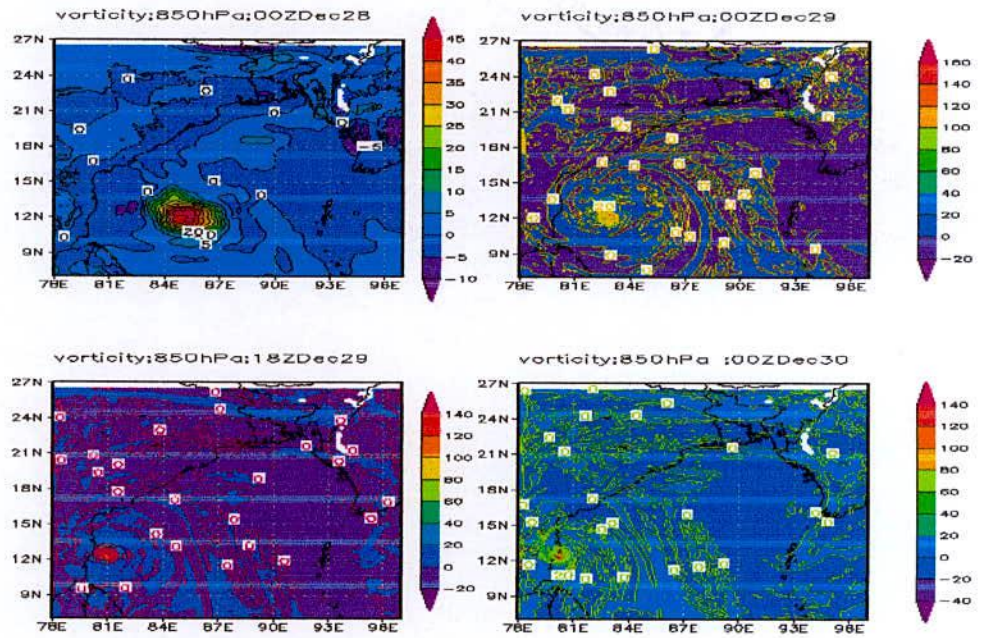


Figure 4.11(a): Model simulated vorticity field at 00 UTC on 28, 29 & 30 December and 18 UTC on 29 December 2011 at 850 hPa level.

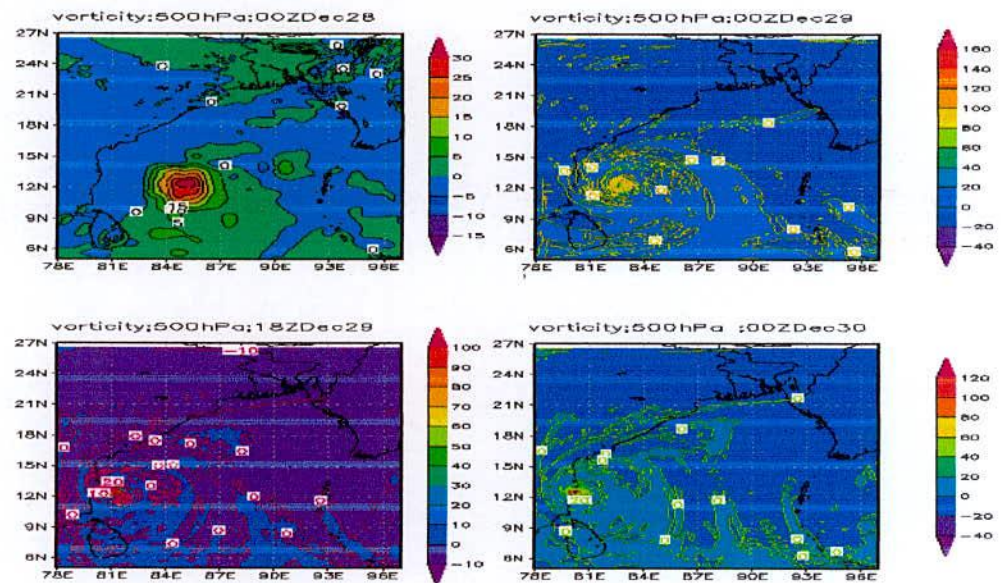


Figure 4.11(b): Model simulated vorticity field at 00 UTC on 28, 29 & 30 December and 18 UTC on 29 December 2011 at 500 hPa level.

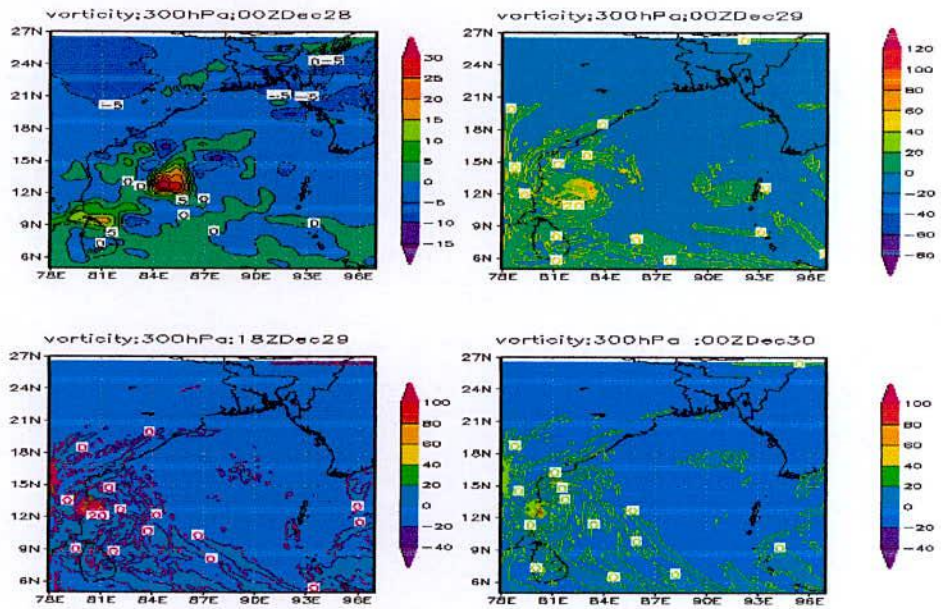


Figure 4.11(c): Model simulated vorticity field at 00 UTC on 28, 29 & 30 December and 18 UTC on 30 December 2011 at 300 hPa level.

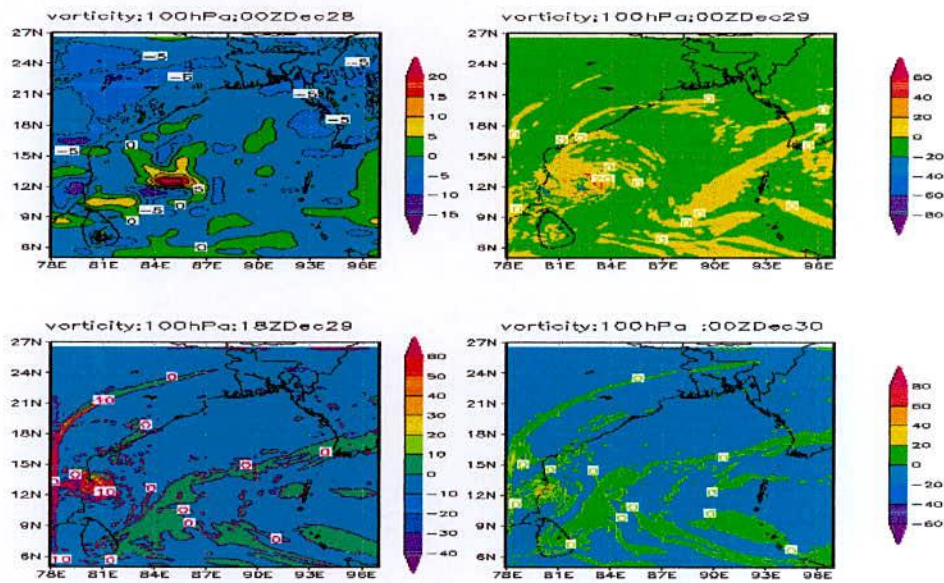


Figure 4.11(d): Model simulated vorticity field at 00 UTC on 28, 29 & 30 December and 18 UTC on 30 December 2011 at 100 hPa level.

#### 4.3.4 Temperature Anomaly

The model simulated temperature anomaly of TC Thane at 00 UTC on 28, 29 & 30 December and 18 UTC on 29 December 2011 has been shown in the Figure 4.12.

At 00 UTC on 28 December 2011, several 3<sup>0</sup>C warm cores are observed in the layers between 900-600 and 350-250 hPa levels. It is seen that the warm core is slightly expanded outward at 900-250 hPa level. The highest anomaly is formed around 700 and 250 hPa levels. The simulated anomaly demonstrates that the warm core is visible in the upper troposphere and any negative anomaly is visible.

At 00 UTC on 29 December 2011, 5<sup>0</sup>C warm core is observed in the layer between 700- 550 and 400-300 hPa levels. The highest anomaly is formed around 300 and 650 hPa levels. At this stage almost everywhere negative anomaly other than a slight embedded anomaly at the westerly part. The simulated anomaly demonstrates that the warm core is visible in the upper troposphere and negative anomaly at the upper levels.

At 18 UTC on 30 December 2011, 6<sup>0</sup>C warm core is observed in the layer between 700- 350 hPa. The highest anomaly is formed around 500 hPa level. At this stage almost everywhere negative anomaly other than a slight embedded anomaly at the westerly part. The simulated anomaly demonstrates that the warm core is visible in the upper troposphere and negative anomaly is almost at the middle levels.

At 00 UTC on 29 December 2011, 3<sup>0</sup>C warm core is observed in the layer between 400-300 hPa. It is seen that the warm core is slightly expanded outward at 1000-800 hPa level. The highest anomaly is formed around 950 hPa level. At this stage almost everywhere negative anomaly other than a slight embedded anomaly at the westerly part. The simulated anomaly demonstrates that the warm core is visible in the upper troposphere and negative anomaly at the upper levels.

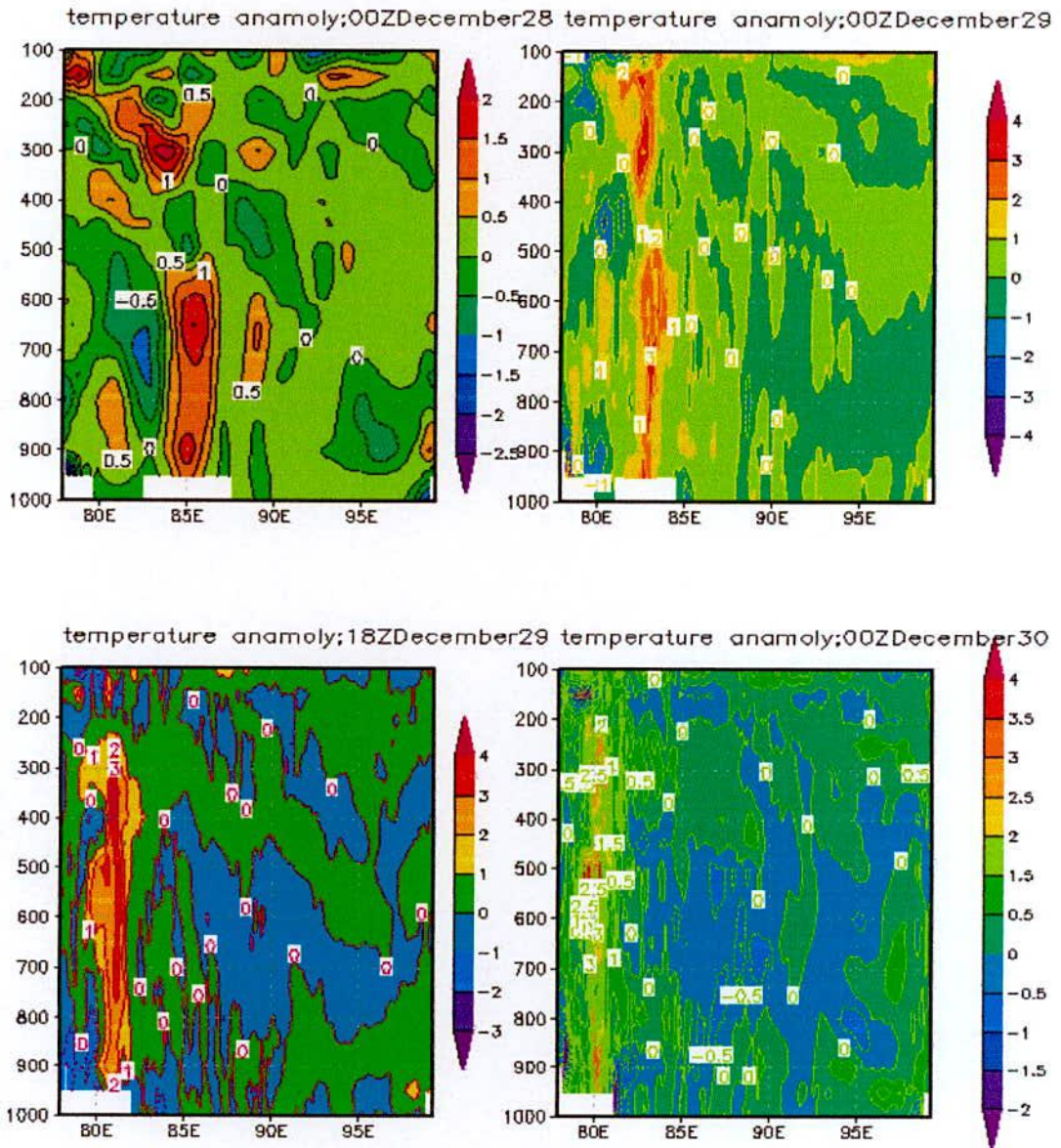


Figure 4.12: Vertical distribution of temperature anomaly in the east-west direction through the centre at 00 UTC on 28, 29 & 30 December and 18 UTC on 30 December 2011.

### 4.3.5 Water Vapor Mixing Ratio

The model simulated vertical distribution of water vapor mixing ratio along the east-west cross section of the center of TC Thane at 00 UTC on 28, 29 & 30 December and 18 UTC on 29 December 2011 has been shown in Figure 4.13. It is observed that the highest water vapor mixing ratio around  $1.8 \times 10^{-2}$  kg/kg or more is found at the centre of the system at 950 hPa level and it decreases upwards to 500 hPa level. It is seen that moisture content distribution has shifted towards eastward with increase of time.

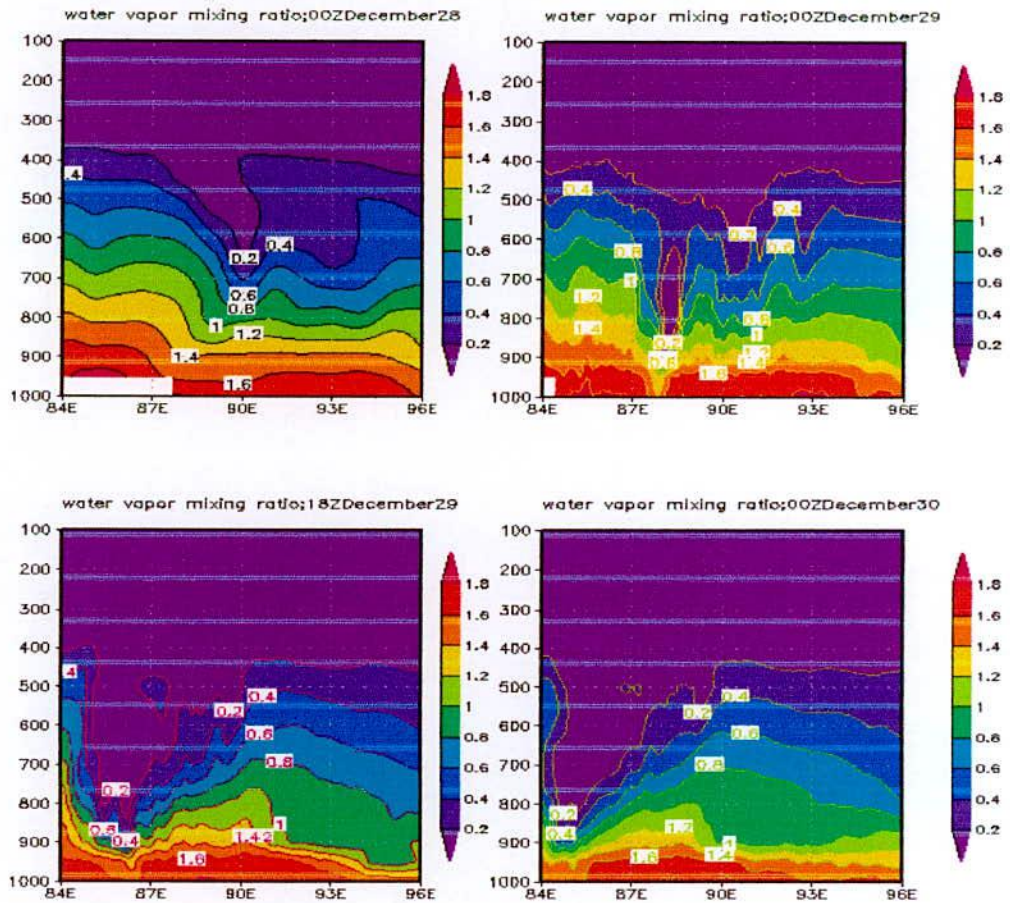


Figure 4.13: Vertical distribution of water vapor mixing ratio in the east-west direction through the centre at 00 UTC on 28, 29 & 30 December and 18 UTC on 30 December 2011.

### 4.3.6 Rainfall Pattern

Model simulated 24 hours accumulated rainfall of TC Thane for the days 28, 29 and 30 December 2011 (i.e, ending at 00 UTC on 29, 30 and 31 December 2011) has been shown in the Figure 4.14.

On 28 December 2011, the rainfall occurs mainly in the sea. On 29 December 2011, the rainfall occurs mainly in the sea and west-southwestern part of India. On 30 December 2011, it rains west-southwestern coastal part of India.

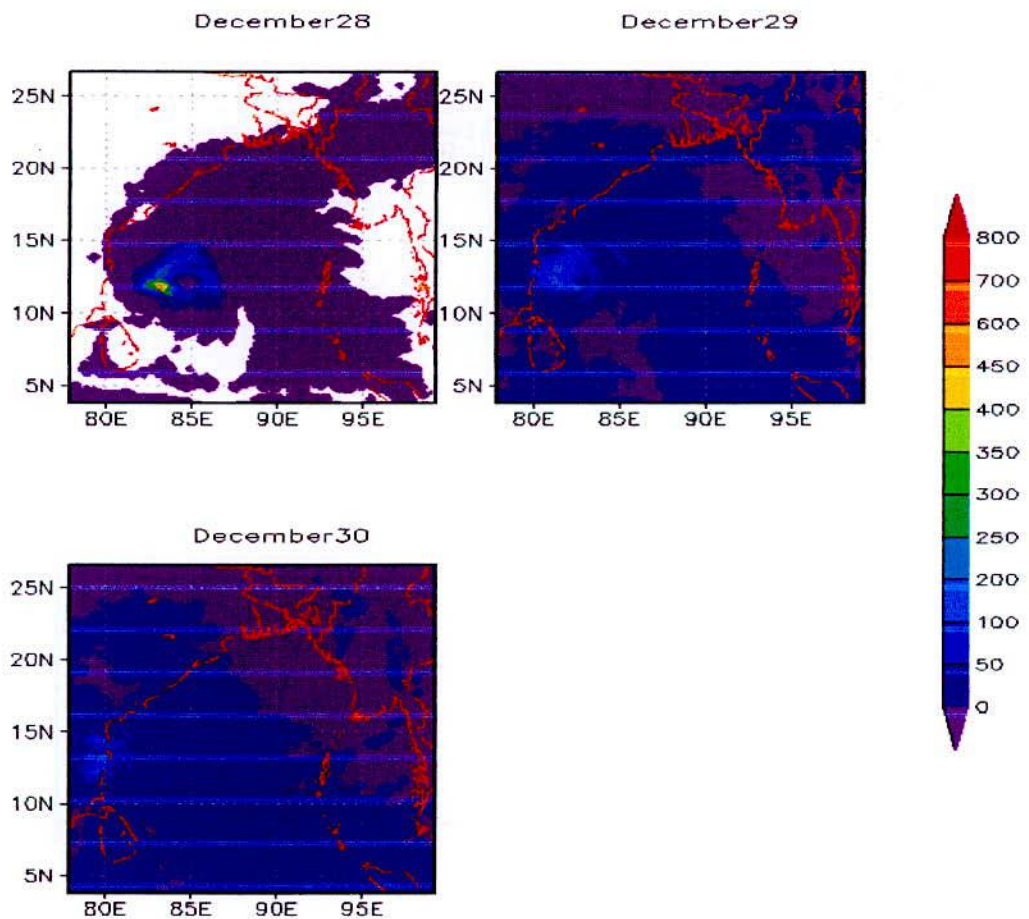


Figure 4.14: 24- hours accumulated rainfall (mm) of TC Thane for the days 28, 29 and 30 December 2011.



## 4.4 Simulation of TC Mahasen

To evaluate the structure of TC Mahasen the WRF model is run for 96 hours from 14 May 2013 at 00 UTC. After 15 hrs on 14 May 2013 at 15 UTC the system attained to state of highest intensity. To evaluate the structure of TC Mahasen the model resulted values of different meteorological parameters for the best combination are discussed graphically, numerically and figuratively in the following subsections comparing with the available data obtained from Indian Meteorological Department (IMD).

### 4.4.1 Pressure Field

To evaluate the TC intensity, minimum sea level pressure (SLP) plays an important role. It is pretty difficult to find any ratification of model simulated SLP with real observable data from the sea before the landfall as TCs develop over the vast oceanic areas where observations are scant or not available. But now meteorologists are able to estimate SLP and maximum sustained wind (MSW) using interpretations of satellite products. Observed and model simulated SLP of TC Mahasen from 00 UTC 14 May 2013 up to 96 hours is presented in Figure 4.16(a). Model simulated SLP falls gradually with time and attains the peak intensity 974 hPa at 15 & 18 UTC on 14 May 2013 and 00 UTC on 15 May 2013 respectively and after that SLP gradually increases. Finally just before the landfall the SLP is 987 hPa at 03 UTC on 16 May 2013 and remains same up to 09 UTC on 16 May 2013. On the other hand the observed peak SLP 990 hPa is obtained at 06 UTC on 15 May and remain same up to 06 UTC 16 May 2013 and after that it increases gradually.

The distribution of sea level pressure (SLP) for the TC Mahasen at 00 UTC on 14, 15 & 16 May and 15 UTC on 16 May 2013 which has been shown in the Figure 4.16(b) which shows the same features as described in Figure 4.16(a).

At 00 UTC on 14, 15 and 16 May 2013 a symmetric and isobaric pressure core is found to be formed. It also clear that the pressure at the center is less than the outer perimeter which confirms the development of the cyclone. On the other hand at 15 UTC on 16 May 2013 the pressure bars are a little bit asymmetric causes to mature cyclone.

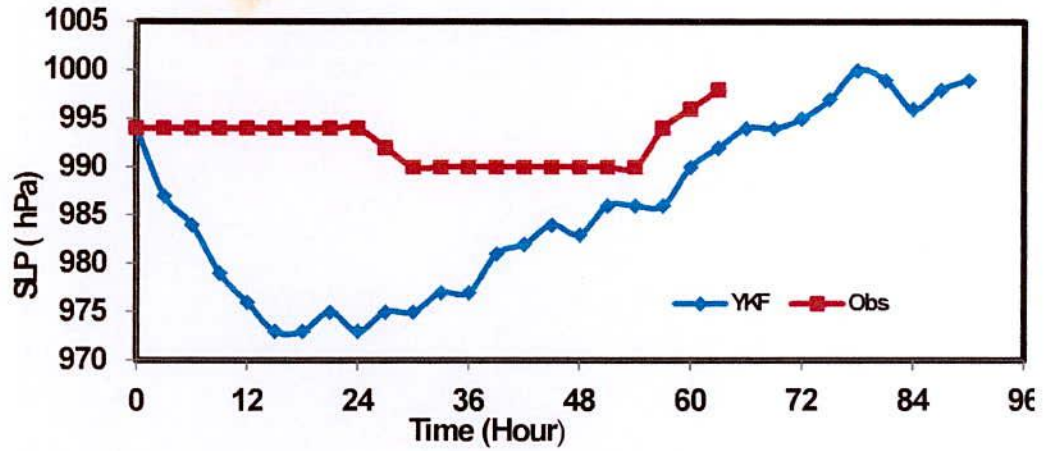


Figure 4.16 (a): Time variation of observed & simulated SLP (hPa) for TC Mahasen.

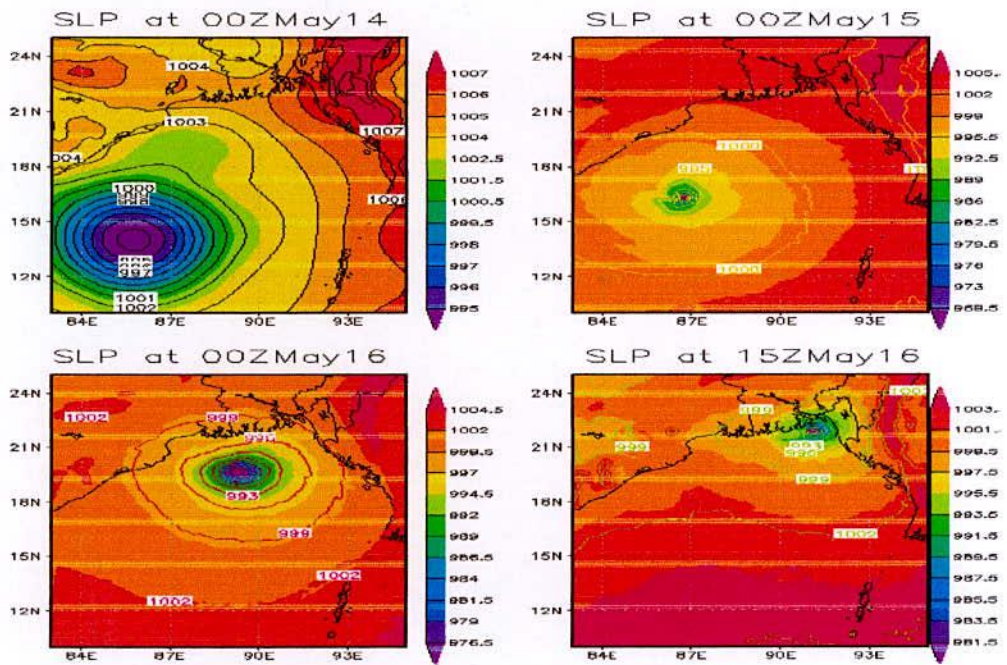


Figure 4.16 (b): Distribution of model simulated SLP (hPa) for TC Mahasen at 00 UTC on 14, 15 & 16 May and 15 UTC on 16 May 2013.

## 4.4.2 WIND FIELD

When the landfall occurs, maximum wind speed (MWS) directly devastates the effected area and it is the most effective force for generating storm, surge over the landfall area. Figure 4.17 (a) shows the time variations of model simulated MWS and observed wind of TC Mahasen. The model simulated MWSs obtained are lower in most of the cases except some deviation at 15, 18 & 21 UTC on 14 May and 03 & 06 UTC on 16 May 2013 from the observed values. Simulated Maximum Wind Speed (MWS)  $24 \text{ ms}^{-1}$  is achieved at 06 UTC on 15 May 2013 and remain same up to 06 UTC on 16 May 2013. On the other hands the observed MWS  $42 \text{ ms}^{-1}$  is achieved at 18 UTC on 14 May 2013 and remain same up to 00 UTC on 15 May 2013.

The distribution of surface wind for Mahasen at 00 UTC on 14, 15 & 16 May and 15 UTC on 16 May (before landfall) 2013 has been shown in the figure 4.17(b). Figures show that the wind field is highly asymmetric in the horizontal distribution. The distribution of surface wind at 00 UTC on 14 May 2013 has been shown in the Figure 4.17(b) when the TC is in the sea. The Figures show that the pattern has an asymmetric wind distribution with strong wind bands at the front left and right sides, close to the centre of north directed moving storm. The wind flow in the core region shows a near circular feature with minimum wind speed at the centre. The maximum wind speed at this time is 15 m/s. At 00 UTC on 14 and 15 May 2013, TC is organized with strong wind band around and the wind flow in the core region shows asymmetric feature with minimum wind at the centre. The maximum wind at this stages are  $30$  and  $40 \text{ ms}^{-1}$  respectively. At 15 UTC on 16 May 2013 just before the landfall, the maximum wind is  $33 \text{ ms}^{-1}$ .

The horizontal distribution of wind vector and magnitude of the wind field for 850, 500, 300 and 100 hPa levels at 00 UTC on 14, 15 & 16 May and 15 UTC on 16 May 2013 has been shown in the Figures 4.17(c), (d), (e), (f), (g) and (h) respectively.

The Figures 4.17 (c) and (d) show that a well organized cyclonic circulation with strong wind encircling the center is found at 850 hPa and that of having a little outflow at right side of 500 hPa levels respectively.

At 300 hPa level wind shows a little bit cyclonic circulation in the lower left side of the TC and visible outflow at the upper right side which is shown in Figure 4.17(e). At 100 hPa level strong outflow is seen from the central part of the cyclone shown in Figure 4.17(f).

Figure 4.17(g) shows the vertical profile of horizontal wind of the system at 00 UTC on 14, 15 & 16 May and 15 UTC on 16 May 2013 which indicates the distribution of strong winds up to 500 hPa level.

The vertical profile of radial, tangential, vertical velocity and horizontal wind of the system just before the landfall at 00 UTC on 14, 15 & 16 May and at 15 UTC on 16 May 2013 has been shown in the Figures 4.17(g), (h) and (i) respectively.

Figure 4.17(g) shows the vertical profile of radial wind at 00 UTC on 14, 15 & 16 May and 15 UTC on May 2013 which indicates that the system is more organised at 15 UTC on 16 May than 00 UTC on 14, 15 & 16 May 2013 and it is also clear that the system has strong inflow in the lower level which bring air to the system from the boundary and lower level, and outflow at the upper level.

Figure 4.17(h) shows the vertical profile of tangential wind at 00 UTC on 14, 15 & 16 May 2013 and 15 UTC on 16 May 2013 which demonstrates that the tangential wind flows towards northerly direction the eastern side of the system and southerly direction at the western side.

Figure 4.17(i) shows the vertical profile of vertical velocity at 00 UTC on 14, 15 & 16 May 2013 and 15 UTC on 16 May 2013 which indicates that there is no vertical velocity of wind at any levels except at 00 UTC on 15 and 15 UTC on 16 May 2013.

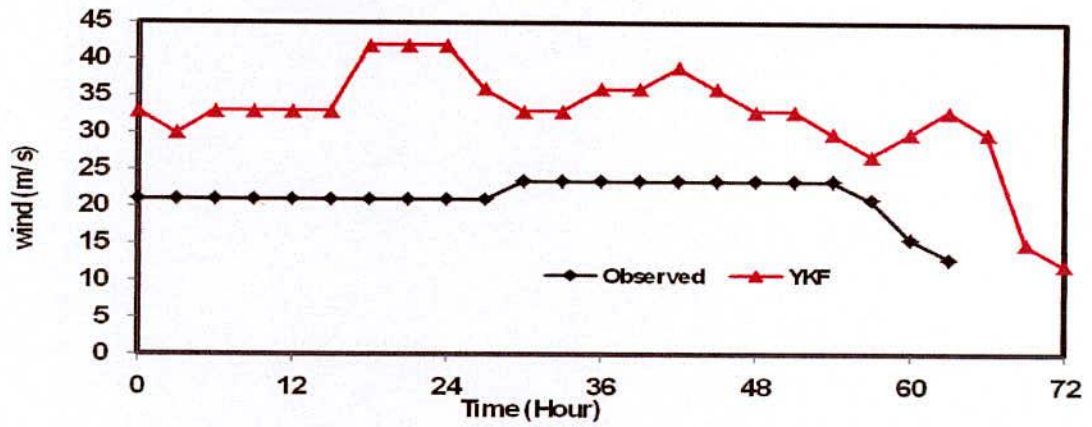


Figure 4.17 (a): Time variation of observed & model simulated wind (m/s) for TC Mahasen.

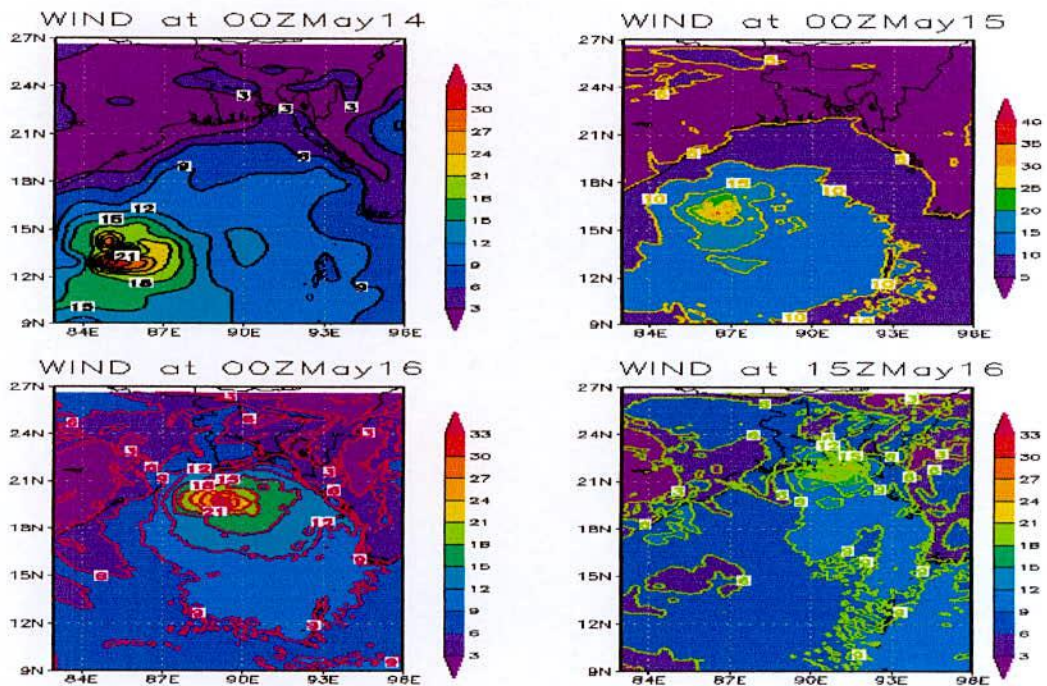


Figure 4.17 (b): Surface wind (m/s) distribution at 00 UTC on 14, 15 & 16 May and 15 UTC on 16 May 2013.

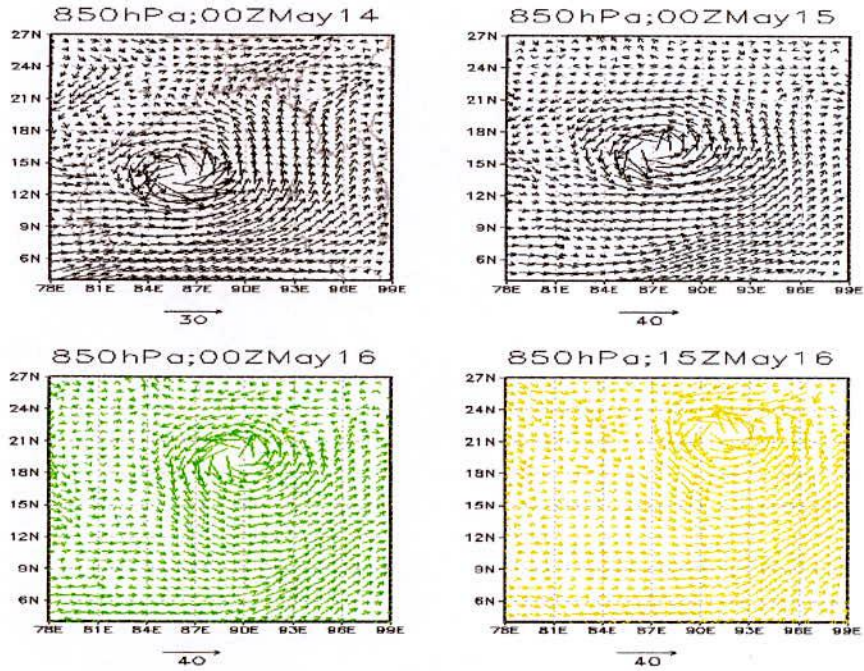


Figure 4.17 (c): Model simulated wind vector and magnitude at 00 UTC on 14, 15 & 21 May and 15 UTC on 16 May 2013 at 850 hPa level.

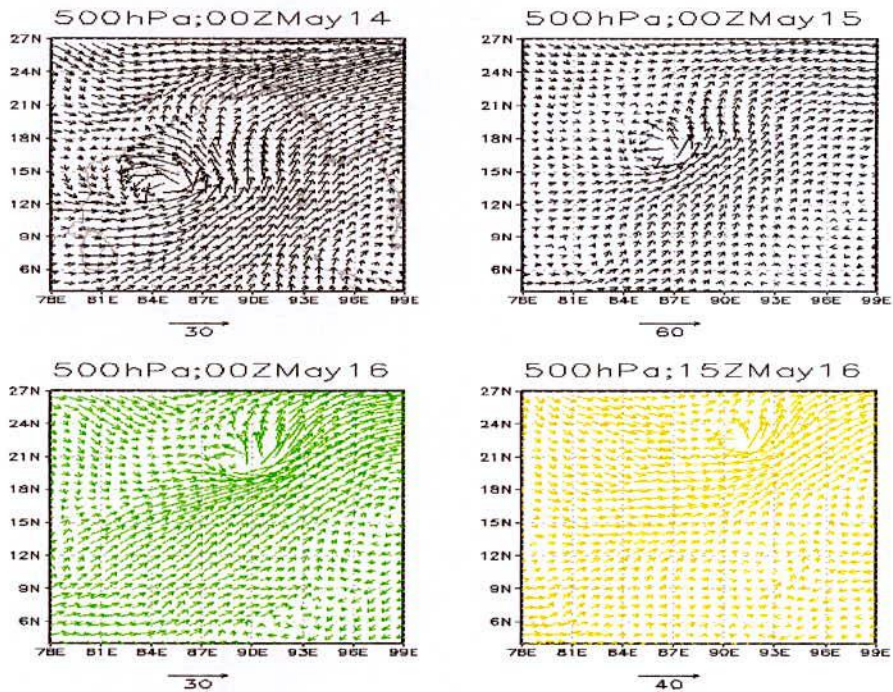


Figure 4.17 (d): Model simulated wind vector and magnitude at 00 UTC on 14, 15 & 21 May and 15 UTC on 16 May 2013 at 500 hPa level.

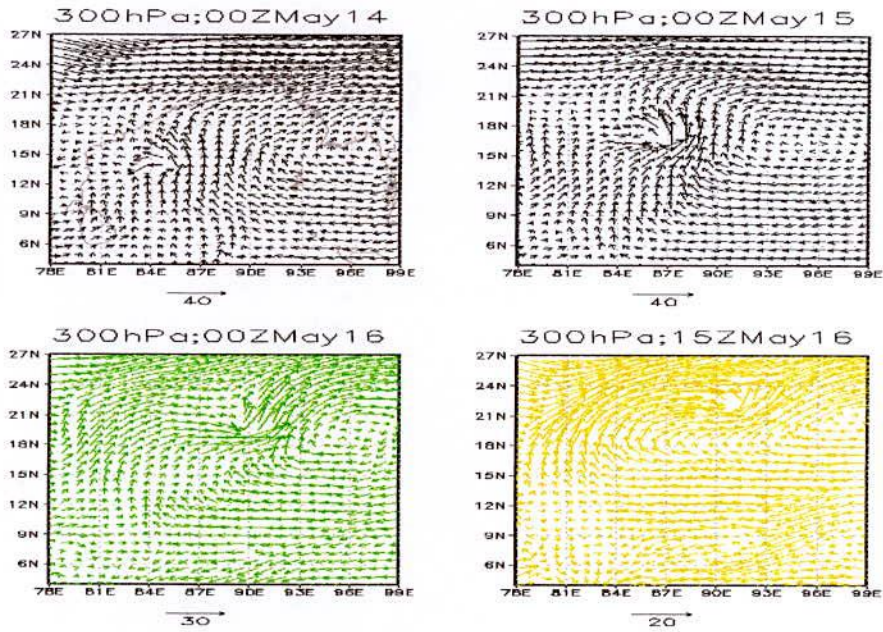


Figure 4.17 (e): Model simulated wind vector and magnitude at 00 UTC on 14, 15 & 16 May and 15 UTC on 16 May 2013 at 300 hPa level.

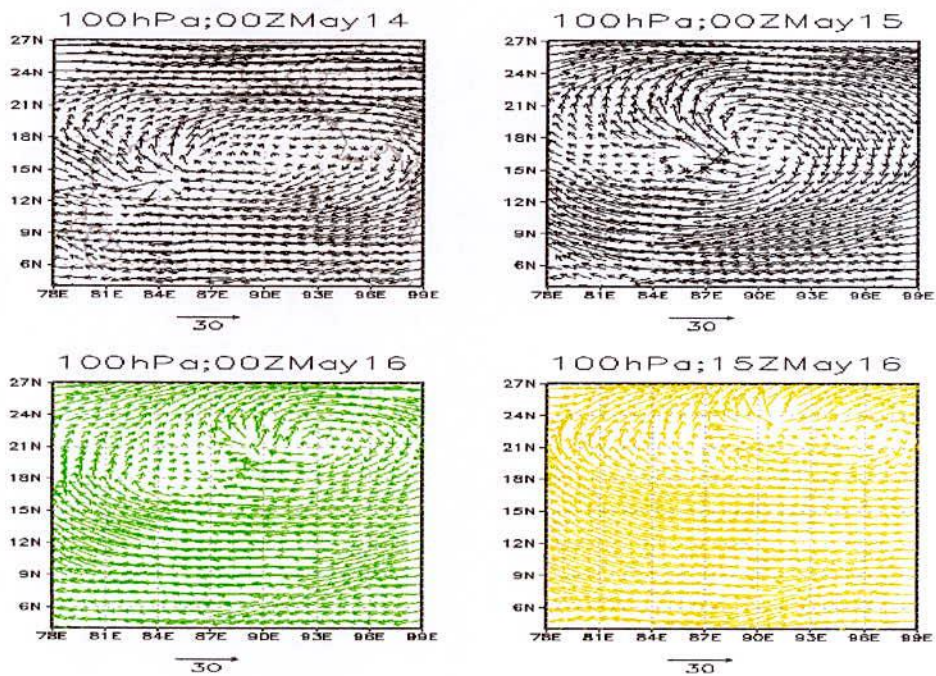


Figure 4.17 (f): Model simulated wind vector and magnitude at 00 UTC on 14, 15 & 16 May and 15 UTC on 16 May 2013 at 100 hPa level.

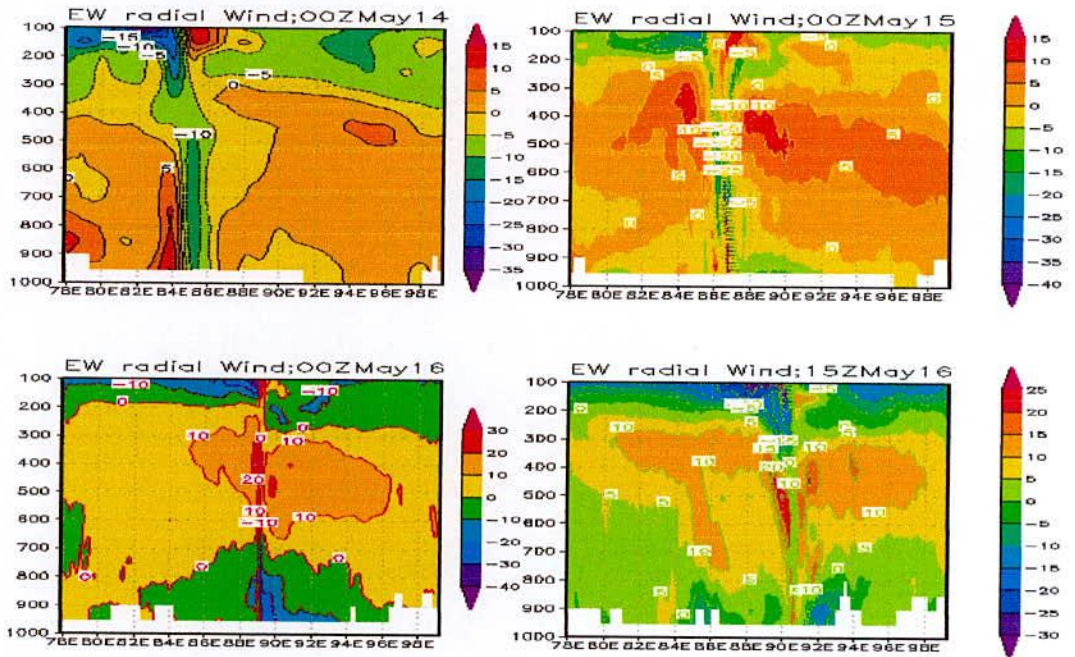


Figure 4.17 (g): Model simulated east-west cross section of vertical profile of radial wind at 00 UTC on 14, 15 & 16 May and 15 UTC on 16 May 2013.

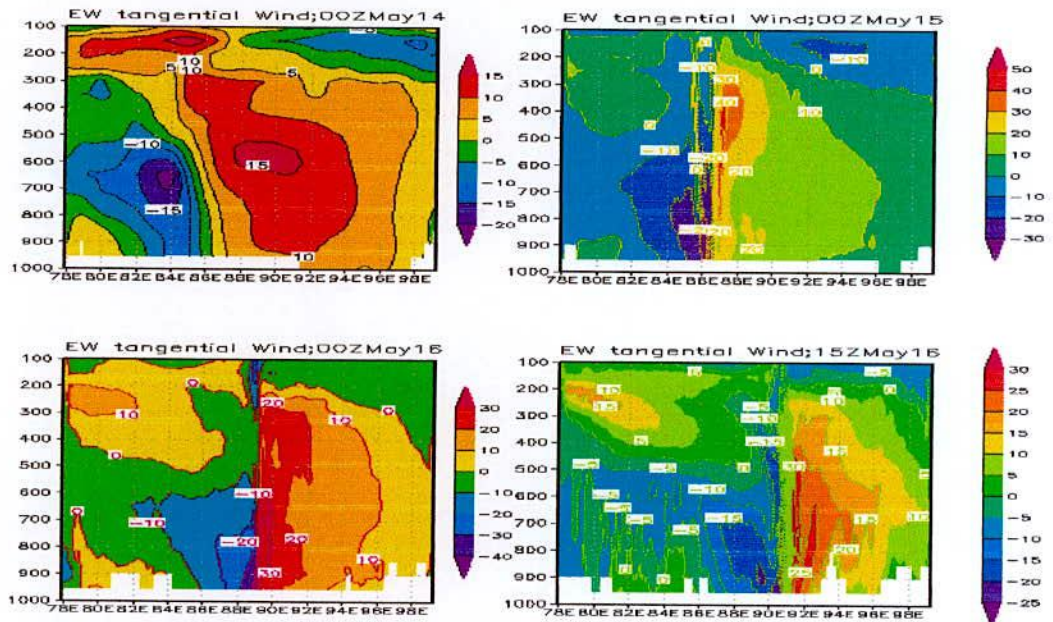


Figure 4.17 (h): Model simulated east-west cross section of vertical profile of tangential wind at 00 UTC on 14, 15 & 16 May and 15 UTC on 16 May 2013.



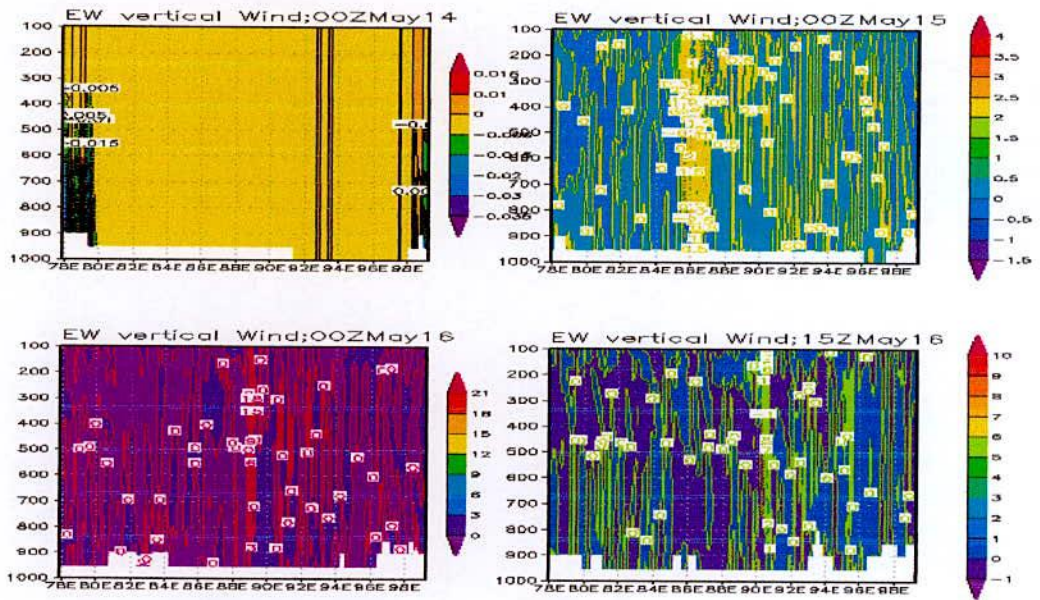


Figure 4.17 (i): Model simulated east-west cross section of vertical profile of vertical wind at 00 UTC on 14, 15 & 16 May and 15 UTC on 16 May 2013.

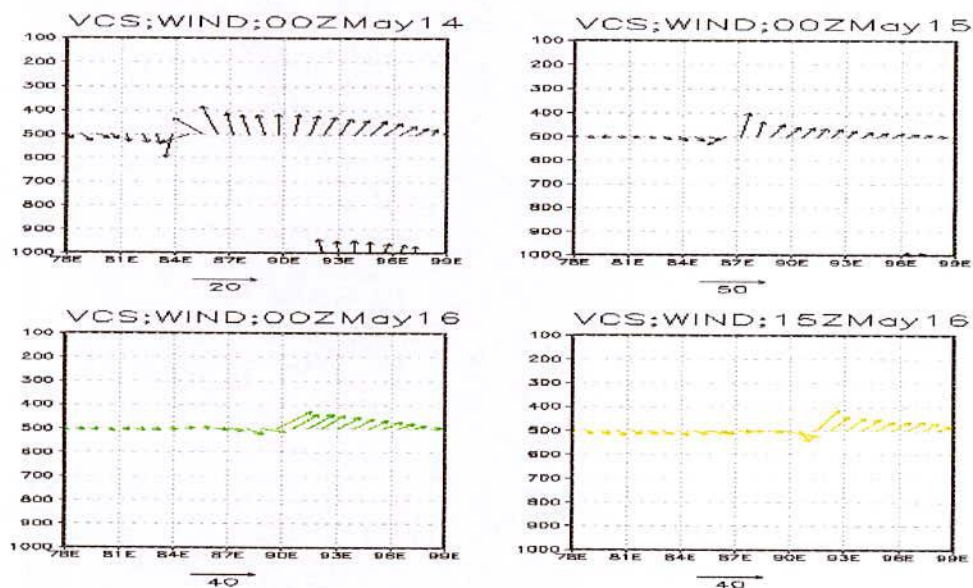


Figure 4.17 (j): Model simulated east-west cross section of vertical profile of horizontal wind for TC Mahasen along the center at 00 UTC on 14, 15 & 16 May and 15 UTC on 16 May 2013.

### 4.4.3 Vorticity Field

The horizontal distribution of relative vorticity at 00 UTC on 14, 15 & 16 May and 15 UTC on 16 May 2013 at 850, 500, 300 and 100 hPa levels have shown in Figures 4.18(a), (b), (c) and (d) respectively.

It is seen from the Figures that the obtained vorticity is distributed with maximum value at the center. The distribution shows circular pattern with some asymmetric features in the outer periphery except at 00 UTC on 14 May 2013 (i.e, initial time) but symmetric circular pattern is available at all the levels in the inner side of the centre.

At 850 hPa level, shown in Figure 4.18(a) negative vorticity is found almost every sides which is followed by a positive and negative vorticity fields at 15 UTC on 16 May 2013. Similar phenomena are found at 00 UTC on 14, 15 and 16 May 2013. The distance of the negative vorticity fields from the center are increased due to intensification of the intensity. Low level vorticity fields confirm the strong cyclonic circulation with different value of the radius at different time in feeding moisture into the system to sustain its intensity.

At 500, 300 and 100 hPa levels the distribution of relative vorticity shows a symmetric character in the horizontal direction.

At 500 and 300 hPa levels the distribution of relative vorticity shows a symmetric character in the horizontal direction which has been shown in Figures 4.18(b) and (c). These values of relative vorticity are increased with the intensification of the intensity of the cyclone and then decreased before landfall. At 00 UTC on 14 May 2013 a core of positive relative vorticity is found to be formed at the 500 hPa level. On the other hand at 15 UTC on 16 May 2013 an embedded core of positive relative vorticity is found to be formed at the 500 hPa level. The values of relative vorticity are increased with the intensification of the intensity of the cyclone and then decreased before landfall.

A weak positive vorticity embedded with negative vorticity field is visible at 100 hPa level shown in Figure 4.18(d). At this level vorticity diversifies to the either direction of the level which confirms the mature development of negative vorticity of the cyclone.

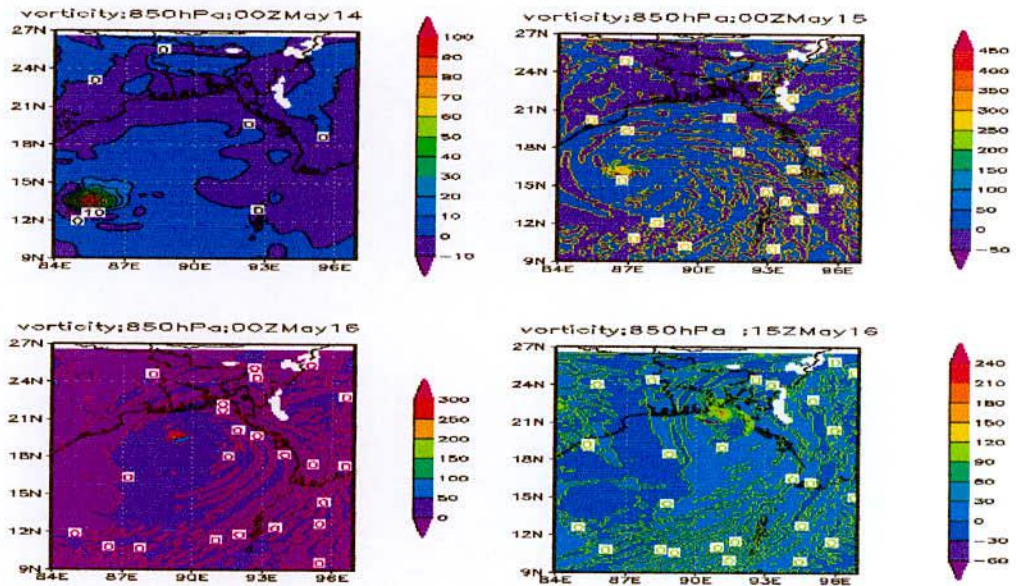


Figure 4.18(a): Model simulated vorticity field at 00 UTC on 14, 15 & 16 May and 15 UTC on 16 May 2013 at 850 hPa level.

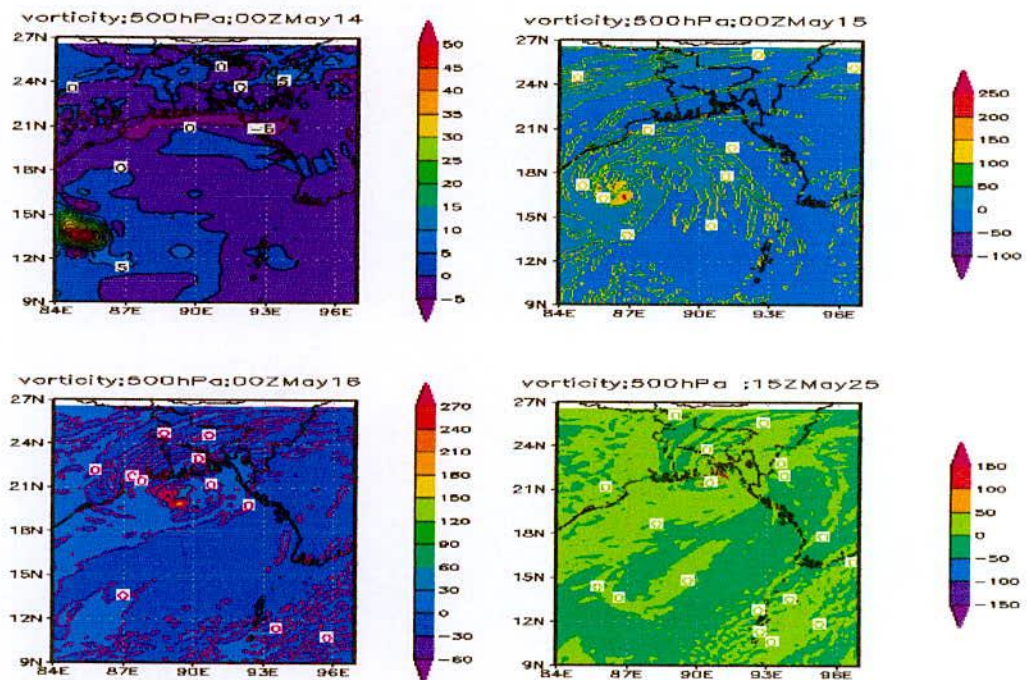


Figure 4.18(b): Model simulated vorticity field at 00 UTC on 14, 15 & 16 May and 15 UTC on 16 May 2013 at 500 hPa level.

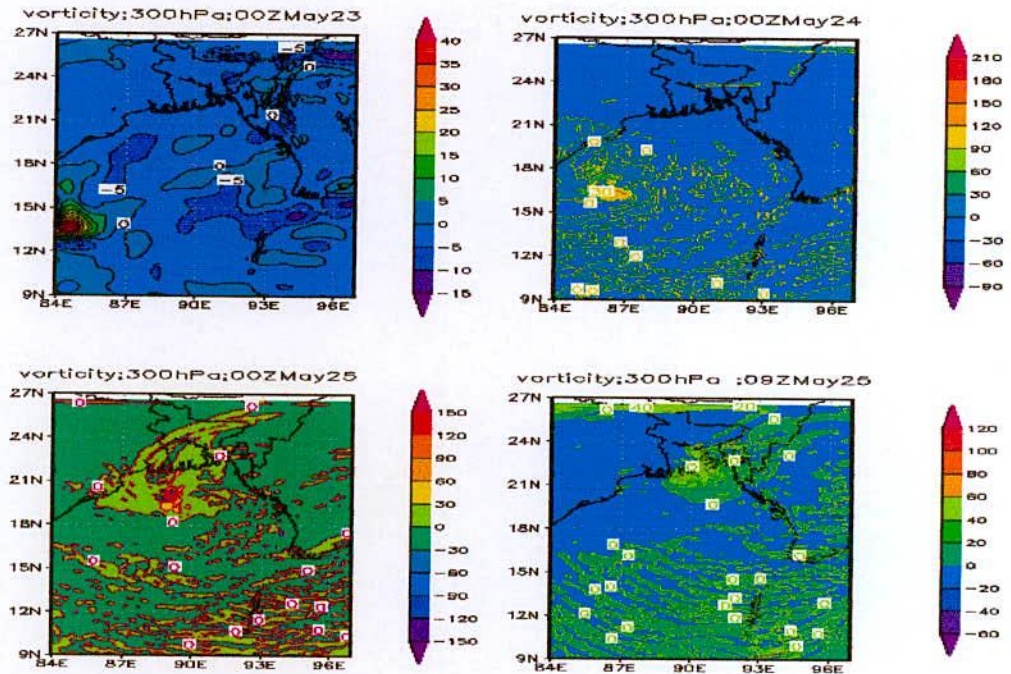


Figure 4.18(c): Model simulated vorticity field at 00 UTC on 14, 15 & 16 May and 15 UTC on 16 May 2013 at 300 hPa level.

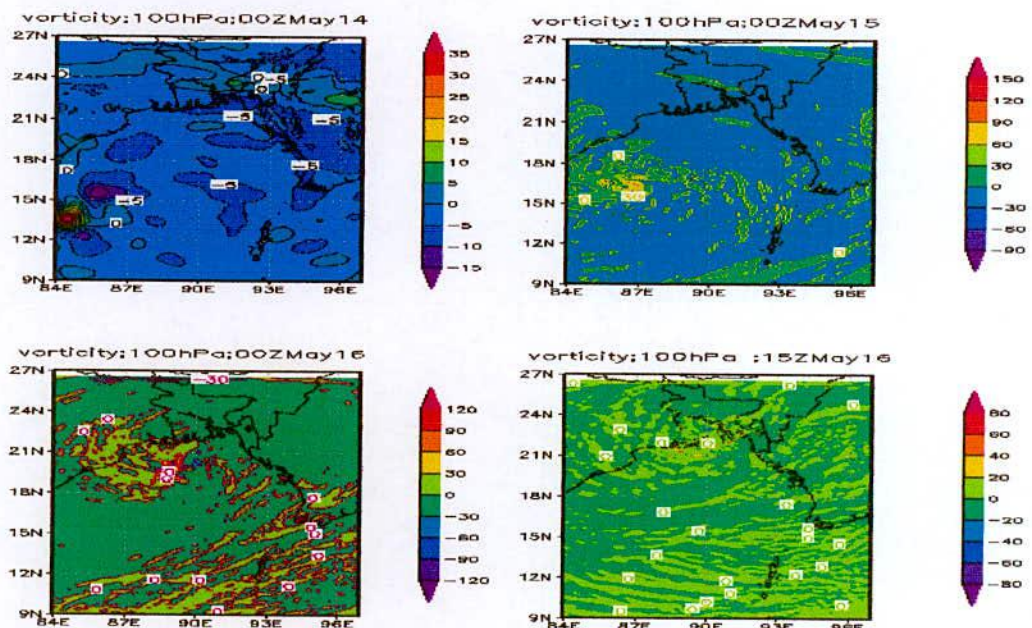


Figure 4.18(d): Model simulated vorticity field at 00 UTC on 14, 15 & 16 May and 15 UTC on 16 May 2013 at 100 hPa level.

#### 4.4.4 Temperature Anomaly

The model simulated temperature anomaly of TC Mahasen at 00 UTC on 14, 15 & 16 May 2013 and 15 UTC (before the landfall) on 16 May 2013 from surface to 100 hPa levels has been shown in the Figure 4.19.

At 00 UTC on 14 May 2013, 5<sup>0</sup>C warm core is observed in the layer between 750- 650 hPa and 350 – 200 hPa levels respectively at 00 UTC. It is seen that the warm core is slightly expanded outward at 400-200 hPa level. The highest anomaly is formed around 700 and 250 hPa levels. The simulated anomaly demonstrates that the warm core is visible in the upper troposphere and negative anomaly at the upper levels.

At 00 UTC on 15 May 2013, 10<sup>0</sup>C warm core is observed in the layer between 400- 150 hPa. The highest anomaly is formed around 250 hPa level. The simulated anomaly demonstrates that the warm core is visible in the upper troposphere and negative anomaly at the upper levels.

At 00 UTC on 16 May 2013, 14<sup>0</sup>C warm core is observed in the layer between 400 - 100 hPa. The highest anomaly is formed around 450 hPa level. The simulated anomaly demonstrates that the warm core is visible in the upper troposphere and negative anomaly at the upper levels.

At 15 UTC on 16 May 2013, 10<sup>0</sup>C warm core is observed in the layer between 1000- 900 hPa. It is seen that the warm core is slightly expanded outward at 1000-800 and 400 - 150 hPa levels. The highest anomaly is formed around 950 hPa level. The simulated anomaly demonstrates that the warm core is visible in the upper troposphere and negative anomaly at the upper levels.

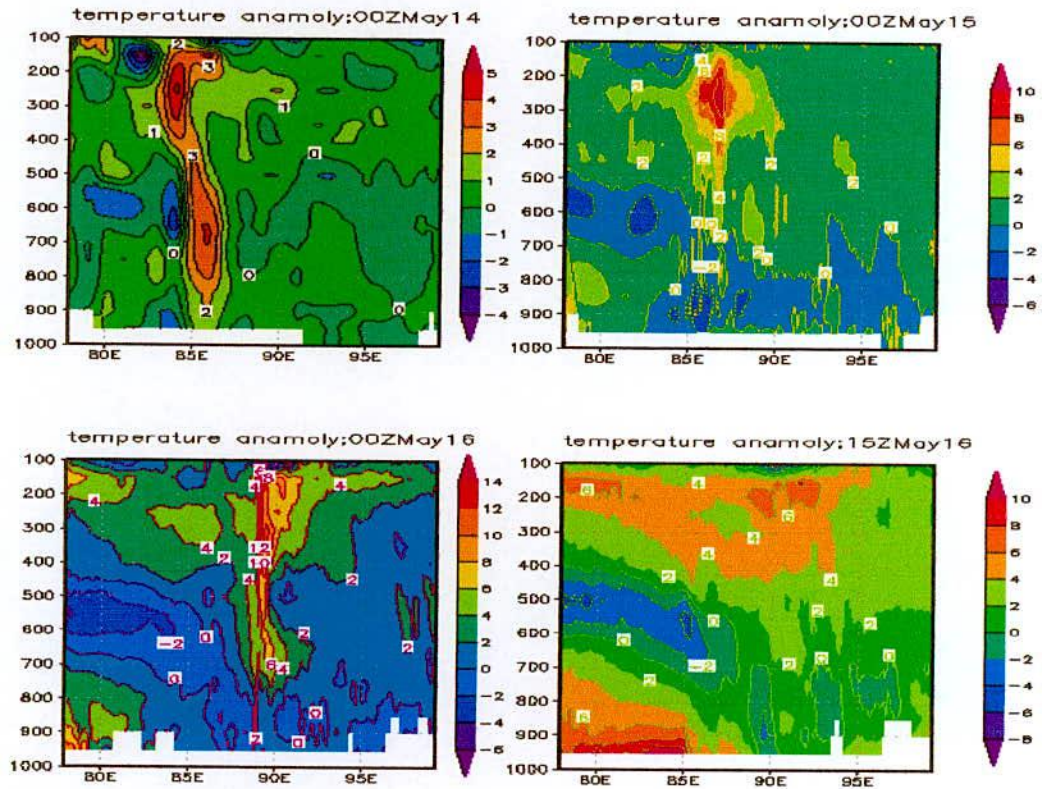


Figure 4.19: Vertical distribution of temperature anomaly in the east-west direction through the centre at 00 UTC on 14, 15 & 16 May and 15 UTC on 16 May 2013.

#### 4.4.5 Water Vapor Mixing Ratio

The model simulated vertical distribution of water vapor mixing ratio along the east-west cross section of the center of TC Mahasen at 00 UTC on 14, 15 & 16 and 15 UTC (before the landfall) on 16 May 2013 from surface to 100 hPa levels has been shown in Figure 4.20. It is observed that the highest water vapor mixing ratio around  $1.8 \times 10^{-2}$  kg/kg or more is found at the centre of the system at 950 hPa level and it decreases upwards to 500 hPa level. It is seen that moisture content distribution has shifted towards eastward with increase of time.

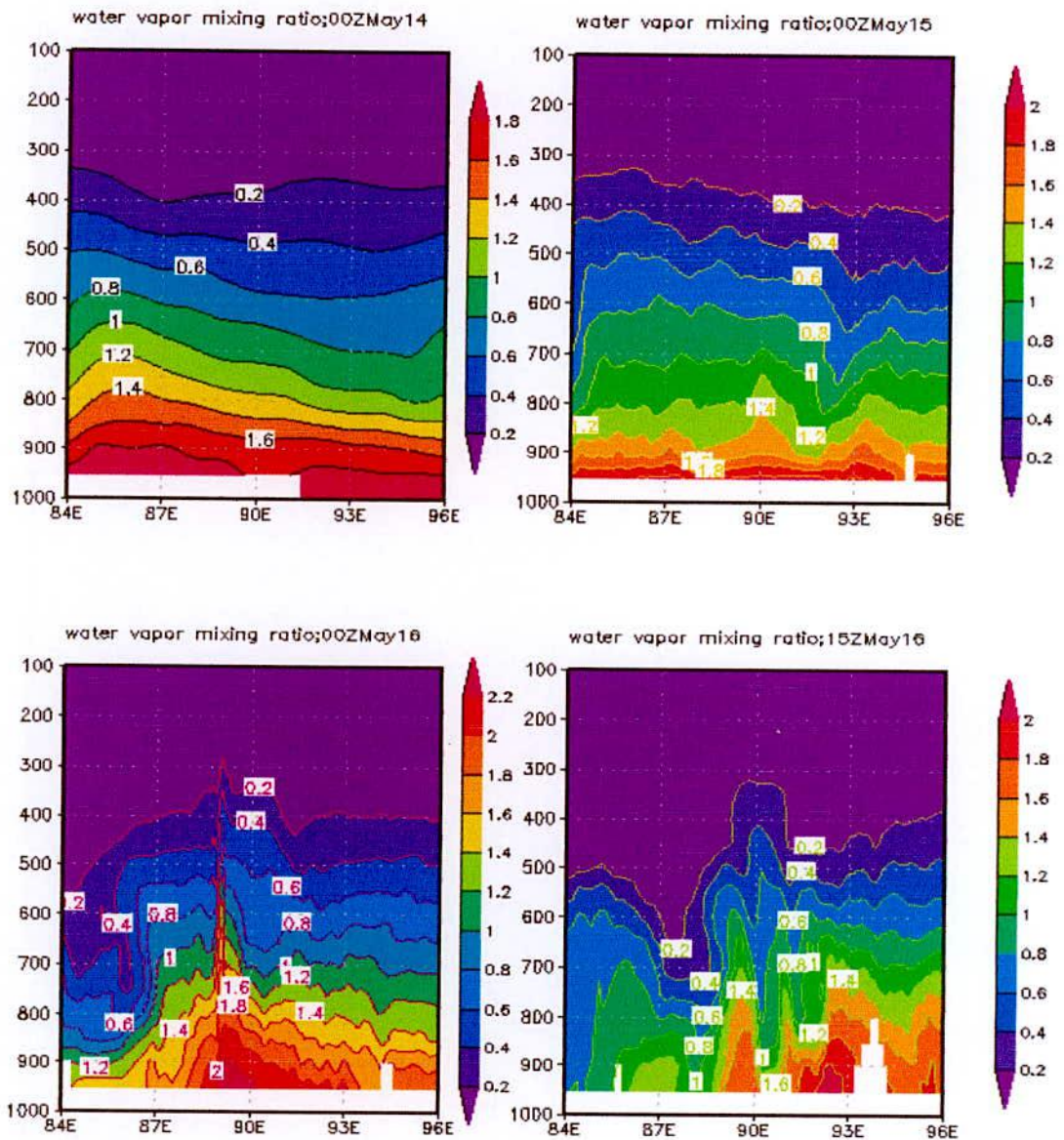


Figure 4.20: Vertical distribution of water vapor mixing ratio in the east-west direction through the centre at 00 UTC on 14, 15 & 16 May and 15 UTC on 16 May 2013.

#### 4.4.6 Rainfall Pattern

Model simulated 24 hours accumulated rainfall of TC Mahasen for the day 14, 15 and 16 May 2013 (i.e, ending at 00 UTC on 15,16 and 17 May 2013) has been shown in the Figure 4.21.

On 14 May 2013, the rainfall occurs in the sea. On 15 May 2013, the rainfall occurs mainly in the sea and south-east coastal part of Bangladesh. On 16 May 2013, it rains south-east coastal and south-eastern part of Bangladesh.

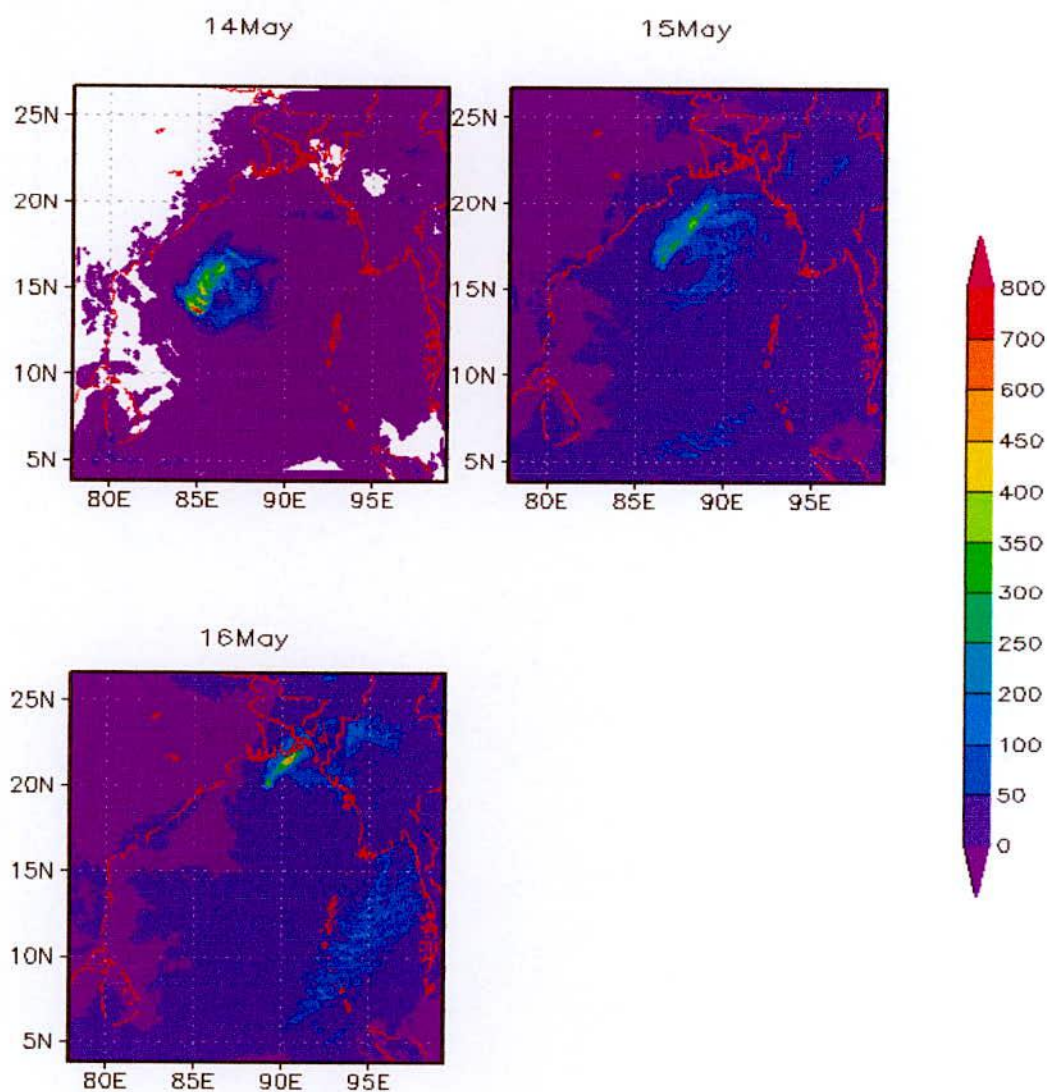


Figure 4.21: 24- hours accumulated rainfall (mm) of TC Mahasen for 14, 15 and 16 May 2013.



## 4.4.7 Track Pattern

Model simulated and observed track of TC Mahasen are plotted in the Figure 4.22. It is visualized from the figure that the model simulated tracks for six selected combination are parallel along with the observed track but other than the YKF simulated track rest of the simulated tracks have been deviated maximum east or west side of the observed track all along the journey from the initial to the landfall. Initially all the simulated tracks have deviated at the east other than YKF. It may be because of initial data error. It reveals that YKF simulated track is obtained more close to the IMD best track than all other simulated tracks. The numerical calculation (shown in Table 4.3) shows that the average track error of YKF is 42 km which is least than any other simulation.

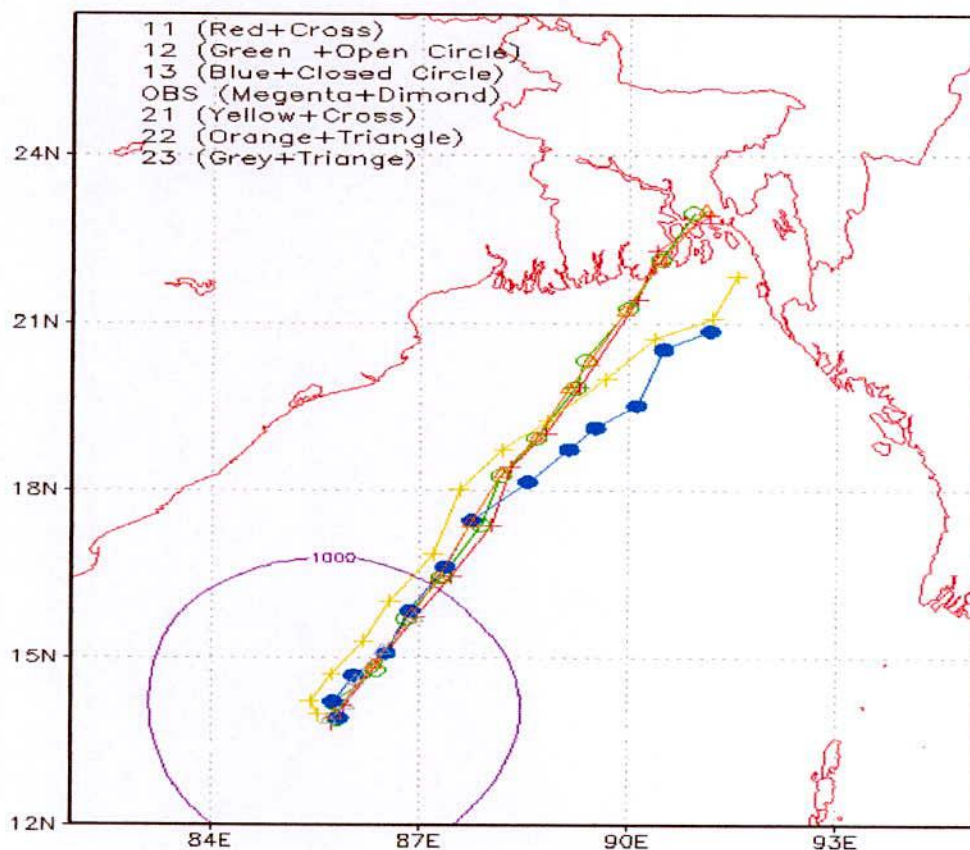


Figure 4.22: Model simulated tracks in 6-h interval for TC Mahasen.

**Chapter 5**  
**Conclusion**

## 5. Conclusions

In the present study the Advanced Research WRF (ARW) model using 9 km single domain has been used for the simulation of three tropical cyclones namely Nargis, Thane and Mahasen using six combination of two PBL's (YSU & MYJ) and three CP's (KF, BM & GD). To understand the dynamics of sensitivity, intensity (wind & slp), vorticity, temperature anomaly, accumulated rainfall, water vapor mixing ratio and track of the mentioned TCs have been simulated and thereby analyzed.

The broad conclusions materialized in this study are presented in the following: From this study, it is clear that the YSU PBL scheme with KF CP scheme shows less track and intensity error out of the six combinations.

1. The Mean RMSE of intensity in terms of CSLP with YSU PBL scheme with KF is 0.782243 hPa for Mahasen, Thane and Nargis respectively while that of MYJ with scheme is 3.61 for Mahasen, Thane and Nargis respectively.
2. Further, the YSU PBL scheme with KF convection scheme simulates the intensity in terms of wind with minimum errors of 2.2, 2.02, and 3.79  $\text{ms}^{-1}$  for Mahasen, Thane and Nargis respectively. These errors are minimum than any other combinations in case of simulated TCs Mahsaen, Thane and Nargis respectively.
3. The KF with YSU PBL scheme returns with the mean track errors of 43.44 km for Mahasen, 21.16 km for Thane and 55.26 km for Nargis respectively, while BM and GD with YSU PBL show 59.50 km and 57 km, 31 km and 30 km and 70.77 km and 101 km respectively. These show the better performance of KF scheme than BM and GD. The KF scheme is also more successful in predicting the landfall compared with BM and GD. Further, the KF and YSU combination shows least track and landfall errors.
4. The mean vector displacement errors using YKF combination has been studied which shows better dynamics of wind movement.
5. The landfall errors are spreaded from 30 to 110 km for different forecast lead times. With the better prediction of track and intensity.

6. The YKF experiment could replicate much of the observed characteristics features such as vorticity, water mixing ratio which satisfy the development of the cyclone.
7. From the study of vertical structural characteristics of the cyclone inner core, it is clear that robust features are observed with YKF combination produced intense horizontal wind speed, strong convergence with intense updrafts within the warmer cyclone core. The enhanced updrafts and storm intensification rate in YKF experiment can be attributed to the feedback mechanism between low-level convergence of warm air, latent heat release in the eye wall, and a correspondent decrease of surface pressure in the inner core of the storm. From the study the warm core of temperature anomaly is also seen.
8. 24-h accumulated rain band is seen around the center of the cyclone.

Finally we can conclude that WRF model can predict the cyclone features. Further this combination can be tested for few TCs on real-time bases and compared the predicted tracks with those of leading operational centers.

## References:

- Anthes RA (1977) Hurricane model experiments with a new cumulus parameterization scheme. *Mon Weather Rev* 105:287–300.
- Anthes RA (1982) Tropical cyclones—their evolution, structure, and effects. Monograph No. 41, American Meteorological Society.
- A modeling study of typhoon Toraji (2001): physical parameterization sensitivity and topographic effect. *Terr Atmos Ocean Sci* 16:177–213
- Arakawa A, Schubert WH (1974) Interaction of a cumulus cloud ensemble with the large-scale environment. Part I. *J Atmos. Sci* 31:674–701.
- Betts, A. K., and M. J. Miller, 1986: A new convective adjustment scheme. Part II: Single column tests using GATE wave, BOMEX, and arctic air-mass data sets. *Quart. J. Roy. Meteor. Soc.*, 112, 693–709.
- Bhaskar Rao et al., 2001 Sensitivity of tropical cyclone intensification to boundary layer and convective processes. *Nat Hazards* 45:429–545.
- Bhaskar Rao DV, Hari Prasad D (2007) Sensitivity of tropical cyclone intensification to boundary layer and convective processes. *Nat Hazards* 41:429–445
- Braun SA, Tao W-K (2000) Sensitivity of high-resolution simulations of hurricane Bob (1991) to planetary boundary layer parameterizations. *Mon Weather Rev* 128:3941–3961.
- Chen, S.-H., and W.-Y. Sun, 2002: A one-dimensional time dependent cloud model. *J. Meteor. Soc. Japan*, 80, 99–118.
- Dudhia, J., 1989: Numerical study of convection observed during the winter monsoon experiment using a mesoscale two-dimensional model, *J. Atmos. Sci.*, 46, 3077–3107.
- Dudhia et al., (2008): Dudhia J., S. Y. Hong and K. S. Lim.: A new method for representing mixed phase particle fall speeds in bulk microphysics parameterizations. *J. Met., Soc. Japan* vol. 86, 33-44.
- Grell GA (1993) Prognostic evaluation of assumptions used by cumulus parameterizations. *Mon Weather Rev* 121:764–787
- Grell, G. A., and D. Devenyi, 2002: A generalized approach to parameterizing convection combining ensemble and data assimilation techniques. *Geophys. Res. Lett.*, 29(14), Article 1693.
- Hong S-Y, Pan H-L (1998) Nocturnal boundary layer vertical diffusion in a medium-range forecast model. *Mon Weather Rev* 124:2322–2339
- Hong, S.-Y., J. Dudhia, and S.-H. Chen, 2004: A Revised Approach to Ice Microphysical Processes for the Bulk Parameterization of Clouds and Precipitation, *Mon. Wea. Rev.*, 132, 103–120.

- Hong and Lim, (2006) A new vertical diffusion package with an explicit treatment of entrainment processes. *Mon. Wea. Rev.*, 132, 2318–2240.
- Hong, S.-Y., and Y. Noh, and J. Dudhia, 2006: A new vertical diffusion package with an explicit treatment of entrainment processes. *Mon. Wea. Rev.*, 134, 2318–2341.
- IMD Atlas (2008) Tracks of storms and depressions in the Bay of Bengal and the Arabian Sea, India Meteorological Department, New Delhi, India
- Janjic, Z. I., 1994: The step-mountain eta coordinate model: further developments of the convection, viscous sublayer and turbulence closure schemes, *Mon. Wea. Rev.*, 122, 927–945.
- Janjic, Z. I., 2000: Comments on "Development and Evaluation of a Convection Scheme for Use in Climate Models", *J. Atmos. Sci.*, 57, p. 3686.
- Janjic, Z. I., 2002: Nonsingular Implementation of the Mellor–Yamada Level 2.5 Scheme in the NCEP Meso model, NCEP Office Note, No. 437, 61 pp.
- Kain, J. S., and J. M. Fritsch, 1990: A one-dimensional entraining/ detraining plume model and its application in convective parameterization, *J. Atmos. Sci.*, 47, 2784–2802.
- Kain, J. S., and J. M. Fritsch, 1993: Convective parameterization for mesoscale models: The Kain-Fritsch scheme, The representation of cumulus convection in numerical models, K. A. Emanuel and D.J. Raymond, Eds., *Amer. Meteor. Soc.*, 246 pp.
- Kain, J. S., 2004: The Kain-Fritsch convective parameterization: An update. *J. Appl. Meteor.*, 43, 170–181.
- Kessler, E., 1969: On the distribution and continuity of water substance in atmospheric circulation, *Meteor. Monogr.*, 32, *Amer. Meteor. Soc.*, 84 pp.
- Kuo H-L (1974) Further studies of the parameterization of the influence of cumulus convection on largescaleflow. *J Atmos Sci* 31:1232–1240
- Kuo Y-H, Reed RJ, Liu Y-B (1996). The ERICA IOP 5 storm. Part III: Mesoscale cyclogenesis and precipitation parameterization. *Mon Weather Rev* 124:1409–1434
- Lin et al. (1983): Bulk parameterization of the snow field in a cloud model. *J. Climate Appl. Meteor.*, 22, 1056-1092.
- Mandal M, Mohanty UC, Raman S (2004) A study on the impact of parameterization of physical processes on prediction of tropical cyclones over the Bay of Bengal With NCAR/PSU mesoscale model. *NatHazards* 31:391–414
- Morrison, H., J. A. Curry, and V. I. Khvorostyanov, 2005: A new double-moment microphysics parameterization for application in cloud and climate models, Part I: Description. *J. Atmos. Sci.*, 62, 1665–1677.

- Mc Cumber et al., (1991) Mohapatra M, Pattanayak Sujata (2010) Simulation of Bay of Bengal tropical cyclones with WRF model: impact of initial and boundary conditions.
- Mellor, G. L., and T. Yamada, 1982: Development of a turbulence closure model for geophysical fluid problems. *Rev. Geophys. Space Phys.*, 20, 851–875.
- Morrison, H., and J. O. Pinto, 2006: Intercomparison of bulk microphysics schemes in mesoscale simulations of springtime Arctic mixed-phase stratiform clouds. *Mon. Wea. Rev.*, 134, 1880–1900.
- Morrison, H., G. Thompson, and V. Tatarskii, 2008: Impact of cloud microphysics on the development of trailing stratiform precipitation in a simulated squall line: Comparison of one- and two-moment schemes. Submitted to *Mon. Wea. Rev.*
- Nat Hazards (2012) 63:1337–1359 1359 123 A simple parameterization of land surface processes for meteorological models. *Mon. Wea. Rev.*, 117, 536–549.
- Rao GV, Bhaskar Rao DV (2003) A review of some observed mesoscale characteristics of tropical cyclones and some preliminary numerical simulations of their kinematic features.
- Rutledge S. A. and P. V Hobbs (1984): The mesoscale and microscale structure and organization of clouds and precipitation in midlatitude cyclones XII: A diagnostic modeling study of precipitation development in narrow cloud- frontal rain bands. *J. Atmos. Sci.*, 20.
- Ryan WR, Rugg S, Elsberry RL, Wegiel J (1996) Evaluations of the AFWA weather research forecast model.
- Shapiro and Willoughby (1982) Use of four-dimensional data assimilation in a limited- area mesoscale model. Part I: Experiments with synoptic-scale data. *Mon. Wea. Rev.*, 118, 1250–1277.
- Smith, (1980) A diagnostic modeling study of precipitation development in narrow cloud- frontal rain bands. *J. Atmos. Sci.*, 20, 2749- 3972.
- Tao, W.-K., J. Simpson, and M. McCumber 1989: An ice-water saturation adjustment, *Mon. Wea. Rev.*, 117, 231–235.
- Tao, W.-K., and J. Simpson, 1993: The Goddard cumulus ensemble model. Part I: Model description. *Terr. Atmos. Oceanic Sci.*, 4, 35–72.
- Tao, W.-K., J. Simpson, D. Baker, S. Braun, M.-D. Chou, B. Ferrier, D. Johnson, A. Khain, S. Lang, B. Lynn, C.-L. Shie, D. Starr, C.-H. Sui, Y. Wang, and P. Wetzel, 2003: Microphysics, radiation and surface processes in the Goddard Cumulus Ensemble (GCE) model. *Meteor. and Atmos. Phys.*, 82, 97–137.

- Technical note, JTWC, 76-3, 12 pp Skamarock WC, Klemp JB, Dudhia J, Gill DO, Barker DM, Wang W, Powers JG (2005) A description of the advanced research WRF version 2.
- Thompson et al. (2004): Explicit forecasts of winter precipitation using an improved bulk microphysics scheme. Part I : Description and sensitivity analysis. *Mon. Wea. Rev.*, 132.
- Thompson, G., R. M. Rasmussen, and K. Manning, 2004: Explicit forecasts of winter precipitation using an improved bulk microphysics scheme. Part I: Description and sensitivity analysis. *Mon. Wea. Rev.*, 132, 519–542.
- Vrieling A, Sterk G, de Jong SM (2009) Mapping rainfall erosivity for Africa with TRMM time series. *Geophys Res Abstr* 11:2034
- Wicker, L. J., and R. B. Wilhelmson, 1995: Simulation and analysis of tornado development and decay within a three-dimensional supercell thunderstorm. *J. Atmos. Sci.*, 52, 2675–2703.
- World Meteorological Organization technical document (2008).
- Yang and Cheng L (2005) The Goddard cumulus ensemble model. Part I: Model description. *Terr. Atmos. Oceanic Sci.*, 4, 35–72.